CAPILLARY FILLING DYNAMICS AS A METROLOGICAL CHARACTERISATION TECHNIQUE FOR THE DETECTION OF RADIUS CHANGES AND SURFACE MODIFICATIONS IN NANOPOROUS ANODIC ALUMINA

Chris Eckstein

DOCTORAL THESIS

Chris Eckstein

CAPILLARY FILLING DYNAMICS IN NANOPOROUS ANODIC ALUMINA FOR BIOSENSING APPLICATIONS

UNIVERSITAT ROVIRA i VIRGILI
Departament d'Enginyeria Electrònica, Elèctrica I Automàtica

Chris Eckstein

CAPILLARY FILLING DYNAMICS IN NANOPOROUS ANODIC ALUMINA FOR BIOSENSING APPLICATIONS

Ph. D. Thesis

Supervised by

Prof. Lluís Francesc Marsal Gaví and Prof. Josep Ferré-Borrull

Departament d'Enginyeria Electrònica, Elèctrica I Automàtica

Nanoelectronic and Photonic Systems (NePhoS)

UNIVERSITAT ROVIRA i VIRGILI

Tarragona

2019

UNIVERSITAT ROVIRA I VIRGILI
CAPILLARY FILLING DYNAMICS AS A METROLOGICAL CHARACTERISATION TECHNIQUE FOR THE DETECTION OF RADIUS CHANGES AND SURFACE MODIFICATIONS IN NANOPOROUS ANODIC ALUMINA
Chris Eckstein

UNIVERSITAT ROVIRA i VIRGILI

Escola Tècnica Superior D'Enginyeria
Departament d'Enginyeria Electrònica, Elèctrica i Automàtica
Campus Sescelades
Avinguda dels Països Catalans, 26
43007 Tarragona
Espanya
Tel.: + 34 977 559 610
Fax: + 34 977 559 605

We, Lluís Francesc Marsal Gaví and Josep Ferré-Borrull, state that the present study, entitled "CAPILLARY FILLING DYNAMICS IN NANOPOROUS ANODIC ALUMINA FOR BIOSENSING APPLICATIONS" presented by Chris Eckstein for the award of the degree of Doctor, has been conducted under our supervision at the Department of Electrical, Electronic and Automatic Engineering of this University, and that it satisfies all requirements to be eligible for the International Doctorate Award.

Tarragona, 2nd May 2019

Doctoral Thesis Supervisors

Prof. Lluís Francesc Marsal Gaví

Prof. Josep Ferré-Borrull

UNIVERSITAT ROVIRA I VIRGILI
CAPILLARY FILLING DYNAMICS AS A METROLOGICAL CHARACTERISATION TECHNIQUE FOR THE DETECTION OF RADIUS CHANGES AND SURFACE MODIFICATIONS IN NANOPOROUS ANODIC ALUMINA
Chris Eckstein

Acknowledgements

While conducting my research as a PhD candidate I was able to enjoy a wealth of freedom and independence when designing and conducting experiments in the lab and together with the sharp attention and vast experience of my superior, this constituted a highly productive and professional learning environment for which I wish to express my deepest gratitude. Therefore, I sincerely wish to thank the University of Rovira i Virgili in Tarragona for the financial support and providing state-of-the-art facilities for the realisation of this PhD. Applying the aforementioned resources in context my supervisors Professor Lluís Francesc Marsall Gaví and Professor José Ferré-Borrull managed to integrate my ideas and results to sculpt the wider shapes of my project and always kept me from walking astray scientifically. Their professional guidance, technical assistance and uplifting encouragements were invaluable to the success of this work for which I am deeply thankful.

I also wish to thank Dr. Abel Santos for facilitating the space, financial resources and intellectual input during the months of my research stay at the School of Chemical Engineering within the University of Adelaide in South Australia. I was not only able appreciate his scientific professionalism but also enjoyed his company exchanging world views over a beer which made the whole exchange a scientifically highly productive and personally joyful experience.

I also extend my gratitude to Elisabet Xifré-Pérez for inducting me into the lab routine and her continuous scientific input, helping with technical trouble-shooting and interpretation of data. Without her help

quickly becoming a productive member of the group and continuously producing good quality data would have been impossible.

For the technical and managerial assistance I am grateful for Pilar Formentin´s upbeat and positive attitude while organising the lab facilities which made sharing work space with her a blissful daily experience.

I also wish to thank Mariana, Rita and Mercè of the Microscopy Department of the Servei de Recursos Científics i Tècnnics Servei (SRCiT) who were always patient and readily available to assist with handling the electron microscopes. A special thank you is addressed to Lukas Vojkuvka for his introduction and support in the clean room.

I wish to emphasise and praise the great work environment, support and collaborations with my fellow group members of NePhos, José, Karen, Laura, Pilar, Maria, Catherina and Aurelien. Thanks guys for a wonderful time and great teamwork.

Last but not least I wish to thank all my close friends and family across the world for the moral support, love, trust and respect. Out of sight is not out of mind.

This work was funded by:

Marti i Franquès Grant from the University of Rovira i Virgili

List of Figures

List of Tables

List of Contributions

Journal Publications

[1] Eckstein, C.; Acosta,L. K.; Pol, L.; Xifré-Pérez, E.; Pallares, J., Ferré-Borrull, J.; Marsal, L. F.; Nanoporous Anodic Alumina Surface Modification by Electrostatic, Covalent, and Immune Complexation Binding investigated by Capillary Filling. *ACS Appl. Mater. Interfaces* **2018**, 10, 10571−10579.

[2] Eckstein, C.**;** Xifré-Pérez, E.; Porta-I-Batalla, M.; Ferré-Borrull, J.; Marsal, L. F.; Optical Monitoring of the Capillary Filling Dynamics Variation in Nanoporous Anodic Alumina toward Sensing Applications. *Langmuir* **2016**, 32 (41), 10467–10472.

[3] Porta-i-Batalla, M.; Xifré-Pérez, E.; Eckstein, C.; Ferré-Borrull, J.; Marsal, L. 3D Nanoporous Anodic Alumina Structures for Sustained Drug Release. *Nanomaterials* **2017**, 7 (8), 227.

[4] Eravuchira, P. J.; Baranowska, M.; Eckstein, C.; Díaz, F.; Llobet, E.; Marsal, L. F.; Ferré-Borrull, J.; Immunosensing by Luminescence Reduction in Surface-Modified Microstructured SU-8. *Appl. Surf. Sci.* **2017**, 392, 883–888.

[5] Porta-i-Batalla, M.; Eckstein, C.; Xifré-Pérez, E.; Formentín, P.; Ferré-Borrull, J.; Marsal, L. F.; Sustained, Controlled and Stimuli-Responsive Drug Release Systems Based on Nanoporous Anodic Alumina with Layer-by-Layer Polyelectrolyte. *Nanoscale Res. Lett*. **2016**, 11 (1), 372.

Conference Contributions

[1] Eckstein, C.; Ferré-Borrull, J.; Xifré-Pérez, E.; Marsal, L. F.; Fluid Imbibition-Coupled Laser Interferometry: a highly sensitive optical technique for nanometrology, Spanish Nanophotonics Conference, 2016, Valencia, Spain. **O*ral Presentation, Poster,***

[2] Eckstein, C.; Xifré-Pérez, E.; Ferré-Borrull, J.; Marsal, L. F.; Estimating the Pore Radius of a Nanoporous Alumina Membrane via Fluid Imbibition-Coupled Laser Interferometry, Porous Semiconductors – Science and Technology, 2016, Tarragona, Spain. ***Poster,***

[3] Ferré-Borrull, J.; Eckstein, C.; Xifré-Perez, E.; Marsal, L. F.; Fluid Imbibition-Coulped Laser Interferometry As a Tool for Optical Biosensing with Anodic Aluminum Oxide, 231st Electrochemical Society Meeting, ECS 2017, Louisiana, USA. ***Oral Presentation,***

[4] Ferré-Borrull, J.; Eckstein, C.; Xifré-Perez, E.; Pallarès, J.; Marsal, L. F.; Optical characterisation of nanofluidic infiltration of nanoporous anodic alumina and its application to biosensing, The 7th International Conference on Optical, Optoelectronic and Photonic Materials and Applications - ICOOPMA 2016, Montréal, Canada. ***Oral Presentation,***

[5] Xifre-Perez, E.; Eckstein, C.; Ferre-Borrull, J.; Marsal, L.F.; Photoluminescent porous alumina particles for the development of label-free biomarkers, Spanish Nanophotonics Conference, CEN 2016, Valencia, Spain. ***Oral Presentation,***

Learning never exhausts the mind

- Leonardo Da Vinci

Somewhere, something incredible is waiting to be known.

- Carl Sagan

I have always believed, and I still believe, that whatever good or bad fortune may come our way we can always give it meaning and transform it into something of value.

- Hermann Hesse, Siddartha

Table of Content

UNIVERSITAT ROVIRA I VIRGILI
CAPILLARY FILLING DYNAMICS AS A METROLOGICAL CHARACTERISATION TECHNIQUE FOR THE DETECTION OF RADIUS CHANGES AND SURFACE MODIFICATIONS IN NANOPOROUS ANODIC ALUMINA
Chris Eckstein

Chapter1

Introduction

1.1 Motivation and Background

Nanotechnology research has gained much interest in the last decades. Fabrication of materials at nano-scale levels has brought to light many new unique physico–chemical characteristics of materials which are otherwise not present in their bulk counterpart. Harvesting these new properties has led to many unique applications in biotechnology, medicine and environmental sciences in recent years. Even though many exciting innovations have already been presented, a wealth of possibilities still lies ahead further uniting the fields of biology, physics, chemistry and material science.

Many of the fundamental biochemical reactions making life possible take place at the nanoscale level and being able to fabricate and modify materials at such level brings about benefits of understanding and controlling biological interactions of living cells, complex tissues or entire organisms with novel materials. Medical applications are bound to be made in the fields of drug delivery, tissue regeneration and wound healing. Environmental applications will further advance the detection and remediation of pollutants. Filtering gas, ions or other small molecules or harvesting and directing electromagnet waves are current applications in the fields of chemistry and physics.

Interdisciplinary techniques finding application across biology, chemistry and physics can be found in the form of sensing systems. The detection of substances or monitoring events at the nanoscale level can be found in cancer diagnostics, detection of environmental pollutants or the detection and monitoring of gaseous substances and light intensities.

The advantages of sensors based on nanomaterials lie in the application of ultra-small sample volumes, which is especially important in the field of biology where tissue samples are often minute or biological reagents are very expensive. Furthermore the downscaling of the reactions has led to new technologies such as lab-on-a-chip (LOC) or point-of-care (POC) devices which have the great potential of being small and portable and can be applied *in situ*, for faster and cheaper retrieval of data.

Nano-optofluidics is a recently introduced term which typically describes applications interfacing liquids carrying an analyte of interest with a solid as the matrix producing an optical signal detected by a measurement system. Nano-optofluidics possesses great potential for the development of novel LOC and POC devices which is what this PhD dissertation is aiming at.

1.2 Objectives of this PhD Dissertation

The main objective of this PhD dissertation lies in working towards the development of a novel type of nano-optofluidic biosensor based on nanopore radius reduction by advancing a recently introduced nano-metrological technique monitoring a laser reflected of the top and bottom surface of a nanoporous membrane while a liquid is traveling through the pores. This technique was termed fluid imbibition-coupled laser interferometry (FICLI) and will be referred to as such throughout this PhD dissertation.

It was at first necessary to learn different fabrication strategies of nanoporous anodic alumina (NAA) leading to a variety of nano-

structured architectures which served as the basic porous matrix for the liquid to pass through for subsequent pore radius estimations using FICLI. Additionally, a range of chemical and biological surface modification strategies had to be controlled for the strategic immobilization of target analytes to the inside pore walls of NAA. For a better comparison of the FICLI technique it was necessary to apply further traditional optical NAA sample characterization techniques, such as scanning electron microscopy (SEM), confocal microscopy, UV/Vis, FTIR and photoluminescence spectroscopy.

A first milestone of this PhD dissertation was set to assess the sensitivity, accuracy and reproducibility of FICLI towards the estimation of pore radius modifications across different liquid-surface interfaces by using different liquids travelling through the pores of a set of consecutively modified NAA structures fabricated with different anodization electrolyte solutions.

A second milestone aimed at assessing complex chemical surface functionalizations and target specific immobilization of biological analytes onto the NAA pore walls and the effects on the estimations of pore radius changes via FICLI.

1.3 Structure of this PhD Dissertation

This PhD dissertation is organized as follows:

Chapter 2 provides a historical and technical overview of the fundamentals and state-of-the-art of optical sensing systems based on NAA. NAA fabrication, pore modification and surface functionalization

strategies are presented, an overview of sensing systems based on NAA is given and the basics of fluidics in nanopores are introduced to help conceptualise technical terminology in the experimental section of this PhD dissertation.

Chapter 3 provides more specific details of the fabrication, modification and functionalization of the NAA for the following experiments and the theoretical and practical background for obtaining NAA pore radius estimations via FICLI. First experiments considering the effects of NAA architectural characteristics and FICLI handling procedures are also discussed.

Chapter 4 presents experiments on applying FICLI as an NAA pore radius estimation technique in comparison to scanning electron microscopy. The sensitivity, accuracy and reproducibility of FICLI towards detecting small pore radius modifications across different liquid-surface interfaces is shown. Further pore radius assessments of more complex NAA pore architectures in the form of bi- and trilayers are further presented.

In chapter 5 the sensitivity, accuracy and reproducibility of FICLI detecting pore radius changes due to the deposition of a variety of chemical and biological materials onto the pore walls are assessed. From single biomolecule immobilization, via the build-up of multi-layer systems of polymers to the detection of target specific immune complexes, FICLI radius estimations are assessed towards the applicability in the context of NAA modified via different physico-chemical immobilization strategies.

Finally, chapter 6 summarizes the main achievements of the presented work and concludes this PhD dissertation.

Chapter2

State-of-the-Art

Chapter Overview

The combination of fluidics and optics has gained much interest in the past decade and many novel applications have been developed. Likewise, research on nanoporous structures has also become widely popular and much insight was gained on controlling the fabrication process and the resulting structural and physico-chemical characteristics of novel types of nano-architecture.

This chapter will give an overview of the fundamentals and the current state-of-the-art of nanoporous optical and optofluidic systems and their components with respective fabrication and modification techniques to provide the background for the coming chapters. At first, we will be introducing the advent of the development of nanoporous anodic alumina (NAA) and hone in on the electrochemical fabrication procedure to control pore morphologies. Secondly, we present surface modifications of NAA to produce varying surface interfaces and to equip NAA with bioconjugates. Thirdly, we present current optical and optofluidic methods employing nanoporous materials narrowing down the focus on capillary driven fluid imbibition as the main experimental focus of this PhD study.

2.1 Fundamentals of Nanoporous Anodic Alumina

2.1.1 Historical Overview

In the early 1900s Bengough, Stuart[1] and Carboni[2] pioneered the electrochemical anodization of aluminium foils in acidic solutions with

an emphasis to produce protective and decorative characteristics in the form of aluminium oxide, i.e. alumina. With the advent of electron microscopy Keller[3] was able to characterize anodic alumina for the first time and discovered hexagonally arranged arrays of pores in the nanometre range. He discovered that the distance between adjacent pore centres, i.e. interpore distance, is proportional to the anodization voltage which led to an increased interest in research on nanoporous anodic alumina (NAA).

Many efforts to theoretically describe the pore formation mechanisms followed throughout the years [4]–[7] and despite the lack of a full understanding about these underlying mechanisms it is conceptually agreed on the *electric field instability model* as the driver of the pore formation process: Upon anodization an alumina thin film is formed across the aluminium-acid interface called the barrier layer. In certain areas on the barrier layer electric field concentrations with stronger electric fields, enhanced ionic conductivity and increased local temperature are generated and act as nucleating centres. At these nucleating centres oxide dissolution is favoured leading to the outgrowth of pores until an equilibrium of ionic dissolution is established at the barrier layer leading to steady pore growth (figure 2.1).

In 1995 Masuda and Fukuda[8] developed a two-step anodization process, a cheap and highly reproducible NAA fabrication strategy allowing the fabrication of NAA with a high aspect ratio and narrow pore size distribution. Following this process manipulating the pore radius and interpore distance by adjusting the anodization parameters

became a feasible instrumentation in many laboratories leading to a large body of scientific output in the field of NAA. This two-step anodization process was later refined by Nielsch et al. [9] and many different types of anodization techniques have been established [10]–[12].

Much research has been put forward on NAA since and many pore modification and surface functionalization strategies were reported to produce various kinds of nanostructures and applications thereof [13], [14]. NAA membranes, fabricated by wet-chemical dissolution of the barrier layer or reactive ion etching can be applied as nano-filters[15], the functionalization with silane groups for the selective retention of analytes via coupling agents[16] and the entrapment and release of molecular loads from within the NAA by stimuli responsive polymers[17] are all of great potential to name but a few application examples.

2.1.2 Electrochemical Fabrication of Nanoporous Anodic Alumina

Based on Gibb's free energy change, a metal spontaneously reacts to produce a thin film of metal oxide when exposed to air or water [18].

$$2Al(s) + \frac{3}{2}O_2(g) \rightarrow Al_2O_3(s); \qquad \Delta G^\circ = -1582\ kJmol^{-1} \qquad (2.1)$$

$$2Al(s) + 3H_2O(l) \rightarrow Al_2O_3(s) + 3H_2(g); \quad \Delta G^\circ = -871\ kJmol^{-1} \qquad (2.2)$$

During electrochemical anodization in an acid electrolyte the metal oxide film is produced via redox reactions [19].

The aluminium oxide barrier layer grows on the aluminium surface (anode).

$$2Al\,(s) + 3H_2O\,(l) \leftrightarrow Al_2O_3(s) + 6H^+\,(aq) + 6e^- \qquad (2.3)$$

The formed aluminium oxide dissolves on the alumina-electrolyte interface (anode).

$$Al_2O_3(s) + 6H^+\,(aq) \rightarrow 2Al^{3+}(aq) + 3H_2O\,(l) \qquad (2.4)$$

Aluminium cations diffuse within the oxide barrier layer (anode).

$$2Al\,(s) \rightarrow 2Al^{3+}(aq) + 6e^- \qquad (2.5)$$

The formation of hydrogen takes place at the electrolyte-cathode interface (cathode).

$$6H^+\,(aq) + 6e^- \rightarrow 3H_2\,(g) \qquad (2.6)$$

Idealistically the current efficiency (μ) during the anodization would be 100% but due to other side reactions, not directly relevant for the anodization of aluminium (e.g. evolution of oxygen species at the anode), it is somewhat lower. The current density (J) of the anodization process under potentiostatic conditions is the combination of the anion (Ja), cation (Jc) and electron (Je) current densities.

$$J = J_a + J_c + J_e\,; \qquad (2.7)$$

which can be simplified to

$$J \cong J_a + J_c \tag{2.8}$$

The electron current density can be neglected since the charges for the redox reaction are primarily transported by Al^{3+} and O^{2-} due to the very low electric conductivity of aluminium oxide. The ion transport is the main rate-limiting step in the anodization process leading to a current density-time transient under potentiostatic conditions with four sections relating to four NAA growth stages (figure 2.2).

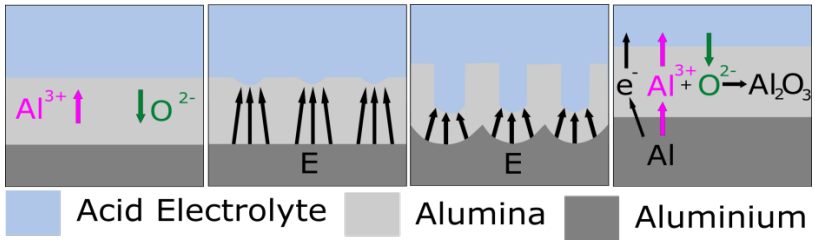

Figure 2.1: Illustration of ion fluxes and electric field instability during the pore formation process.

During the first stage the aluminium oxide layer is formed leading to a sudden drop in current density. During the second stage when the current density is lowest due to the non-conductive barrier layer the formation of electric field instabilities leads to localised dissolution of aluminium oxide. These localised areas of dissolved alumina lead to a rise in current density, pore nucleation and the onset of pore growth in the third stage. During fourth stage the nucleated areas reached a thickness where an equilibrium between formation and dissolution of aluminium oxide is reached, and steady pore growth occurs which is

indicated by a slight asymptotical drop in current density to a constant value.

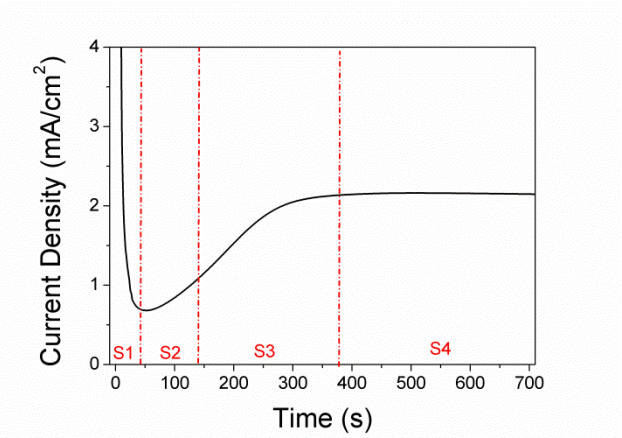

Figure2.2: Current density over time during the first minutes of the anodization process

The two interfaces of the growing NAA have been shown to be chemically distinct by producing an inner layer (aluminium - aluminium oxide interface) of pure aluminium oxide and an outer layer (aluminium oxide - electrolyte interface) which contains anionic electrolyte contaminants and is less resistant to chemical etching. Under ordered pore growth regimes the ratio of the inner and outer layer is constant and independent from the used electrolyte[9].

Figure 2.3: Illustration of the pure inner and contaminated outer layer of aluminium oxide formed during the anodization process.

2.1.3 Effects of Anodization Parameters on the Structure of Nanoporous Anodic Alumina

Important anodization parameters are anodization voltage (V), anodization time (t) and temperature (T) and the type and concentration (C) of the electrolyte which all have a direct effect on the structural characteristics of NAA such as the pore radius (R), interpore distance (d_{int}, the distance of the centres of two adjacent pores), porosity (P), NAA thickness (L), barrier layer thickness (L_{BL}) and the degree of hexagonal arrangement[9].

The anodization voltage has a tremendous effect on the NAA structure and in order to avoid burning phenomenon the anodization voltage is limited in range depending on the respective acid electrolyte in use and its concentration. Choosing a too high voltage can lead to sample burning due to local heating and an increase in conductivity, ionization of atoms leading to excessive electron generation, or breakdown of the barrier layer from cracks. The properties of the acid electrolytes in use

bring about specific limitations on the anodization parameters and therefore on the resulting NAA structure. Even though a variety of electrolytes were reported for the fabrication of NAA, the most common acids are sulfuric (H_2SO_4), oxalic ($H_2C_2O_4$) and phosphoric (H_3PO_3) acid.

Regardless of the acid electrolyte, the anodization voltage is directly proportional to the interpore distance d_{int} and is a commonly used modifier of the NAA structure.

$$d_{inter} = K_1 V$$

where K_1 is the proportionality constant of 2.5-2.8nm/V. With decreasing respective conductivities of these acid electrolytes typically used voltages are around 20 V for sulfuric[20], 40 V for oxalic[8] and 160-195 V for phosphoric acid[21]. These anodization conditions lead to the fabrication of NAA with interpore distances of 55, 100 and 400-500 nm, respectively. Less commonly used acid solutions such as malonic[22] and citric acid[23] at 140 V and 240 V produce NAA with interpore distances of 270 and 600 nm. Additionally, the barrier layer thickness is linked to the voltage by $L_{BL} = 0.5 \times d_{int}$ [24].

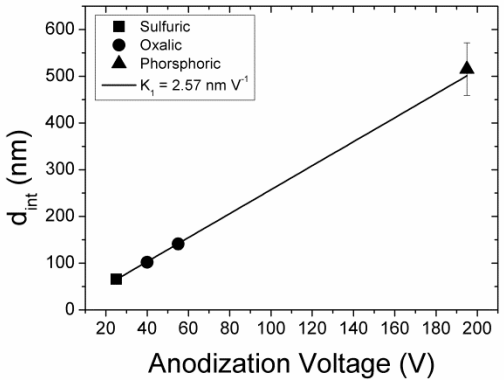

Figure 2.4: Dependence of the interpore distance (d_{int}) on the applied voltage (V) during the anodization process.

The higher the conductivity of the acid the lower the applied voltage has to be to reduce heat production by the Joule effect. With a lower pH of the acid electrolyte less potential is necessary to generate pore growth and the smaller the resulting fabricated pores[9].

The electrolyte temperature has a direct effect on the pore growth rate and pore radius (R). Higher temperatures lead to faster growth rates but also to higher dissolution rates of the newly formed aluminium oxide at the oxide-electrolyte interface resulting in larger pores[25]. Additionally, higher temperatures of the acid electrolyte are less effective in dissipating heat generated by the Joule effect at the pore tips posing higher risks of burning the NAA during the fabrication. Typically, sulfuric and oxalic acid are kept between 0 – 5 °C and phosphoric acid is usually kept at 0 °C.

In respect thereof, adding alcohol-based solvents to keep the electrolyte from freezing when temperatures below 0 °C are needed changes the viscosity which in turn affects d_{int} and $L_{BL.}$ Higher viscosity reduces electrophoretic velocity and therefore the current density leading to a slower pore growth rate with less localised heating and helps to avoid acid breakdown[26], [27].

Under potentiostatic conditions the total thickness (L) is linearly dependent on the total current charge (Q) which allows precise fabrication of NAA with a desired final thickness[28].

2.1.4 Two-Step Anodization for the Fabrication of Self-Ordered Nanoporous Anodic Alumina

Based on the naturally occurring self-ordering of pores during the anodization of aluminium Masuda and Fukuda[8] developed a two-step anodization process in 1995 that has since then lead to an enormous research output in the field of nanoporous anodic alumina (figure2.5). With this process all NAA samples were fabricated for the experimental evaluation of the optofluidic technique described later.

After an initial electropolishing step to produce a mirror-like surface of the aluminium foil a long first anodization step of about 24 hours is carried out. During this time initially disordered pores start growing outwards and, by following a self-ordering mechanism, arrange into domains of hexagonally ordered pores at the pore bottom. The self-ordering mechanism in NAA can be explained by mechanical compressive stress due to the volume expansion from aluminium to

aluminium oxide during anodization which promotes self-ordering through generated repulsive forces[29].

Upon completion of this first step, the formed layer of aluminium oxide with unordered pores at the top and ordered pores at the bottom is completely removed by wet chemical etching leaving a pattern of nanoimprints on the aluminium surface. Upon starting a second anodization step with the same anodization conditions, the pores start nucleating from the nanoimprints patterned onto the aluminium surface and begin to grow outwards in an orderly fashion right from the start. This hexagonal outgrowth is preserved throughout the duration of the second anodization step and large aspect ratios can be fabricated with an NAA thickness of up to 100 μm.

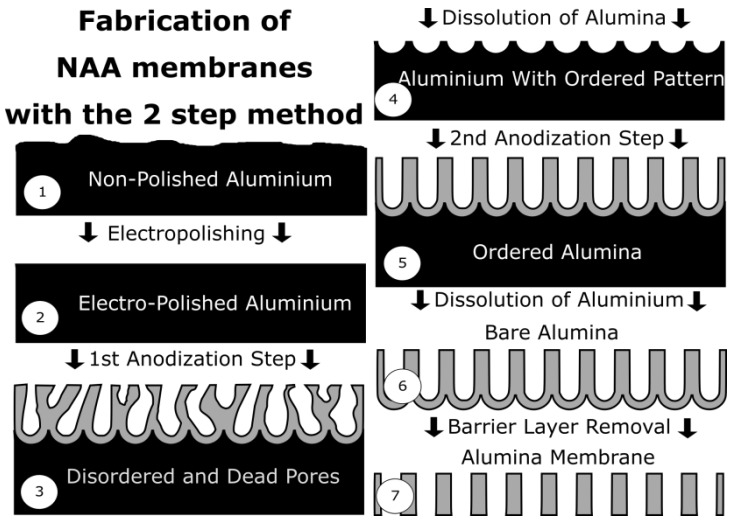

Figure 2.5: Illustration of the formation of ordered pores during the 2 step anodization process and barrier layer removal.

2.2 Structural Modification and Functionalization of Nanoporous Anodic Alumina

2.2.1. Barrier Layer Removal of Nanoporous Anodic Alumina

For certain applications it is necessary to use NAA membranes, hence pores that are exposed to the environment on the top and bottom side [30]–[32]. However, not much attention has thus far been given to the removal of the barrier layer and the pore opening process [33]–[36].

The thickness of the oxide barrier layer can be deduced from the anodization parameters and it is possible to estimate the time needed to wet-chemically remove it to obtain a through-hole pore morphology[37], [38]. Even though widely used, with this method it is not possible to remove the barrier layer in a controlled fashion without attacking the inner pore walls and thereby altering the porosity. Using a simple electro-chemical permeation cell with two electrodes it is possible to monitor current through the pores and determine the onset of the pore opening once the barrier layer is sufficiently attacked [33], [36]. The termination of this process is based on the observation of a plateauing current once the pores are fully open and, even though, the determination of the opening end point is significantly improved it does not provide absolute certainty of unaltered pore morphologies.

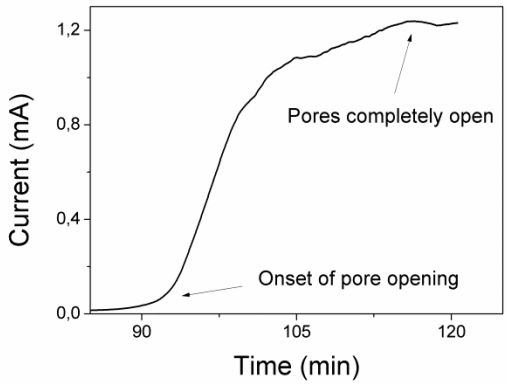

Figure 2.6: Current monitored pore opening with 5% H_3PO_4 in a half permeation cell.

Alternatively, advances in semiconductor fabrication techniques brought about technological developments in ion beam, plasma and atomic etching technologies which are highly sophisticated methods to physically attack an exposed surface with high precision and reproducibility. In recent years advances in nanopore fabrication employed techniques such as focused ion beam (FIB)[39], electron beam drilling[40] [41], ion beam sculpting[42] and reactive ion etching (RIE)[43].

Electron beam lithography coupled with reactive ion etching and a final anisotropical wet etch was shown to produce a single through hole structure with 50 – 100nm in diameter on a silica wafer [40].

Applicable to a wider size range from single pore to multiple pore arrays focused ion beam milling was demonstrated to produce controlled and

reproducible dimensions of opened pores on NAA with circular patterns of 50 nm, 500 nm, and 5 µm [34].

Free silica nanotubes were fabricated by layer-by-layer deposition of silica on an NAA template with subsequent large scale removal of the silica top layer via RIE and wet chemical removal of the NAA matrix[44]. To suppress sidewall etching via sidewall passivation of aluminium during inductively coupled plasma reactive ion etching (ICP-RIE), fluoroform (CHF_3) was simultaneously flown during the etch process and shown to effectively protect the sidewalls [45]. It was further shown that the etch rate of alumina highly depends on the applied particle bombardment energy whereas fluorine concentration and flow rate has little effect [46].

2.2.2 Increasing Porosity of Nanoporous Anodic Alumina

The porosity of NAA is used as an indicator and anodization in sulfuric, oxalic and phosphoric acid follow the 10% porosity rule[9].

$$P = \frac{2\pi}{\sqrt{3}}\left(\frac{R}{d_{int}}\right)^2 \tag{2.9}$$

The porosity is comprised by the interpore distance (d_{int}) and the pore radius (R) and can be adapted to the needs of a specific application. Controlling the interpore distance via anodization conditions has to be part of the initial experimental planning. Controlling the pore radius, however, is routinely done post-fabrication of NAA via simple wet-chemical etching or so-called pore widening in 5% H_3PO_4 at 30 – 40°C[4],

[38], [47], [48]. Figures 2.7 and 2.8 show the effects of pore widening over time (t_{PW}) for NAA fabricated with sulfuric (25 V), oxalic (40 V) and phosphoric acid (195 V). The samples were etched in successive steps at different pore widening times t_{PW} in 5% H_3PO_4 at 35 °C with intermittent environmental scanning electron microscopy (ESEM). The pore radius was extracted from the images by image analysis using *image J* image analysis software.

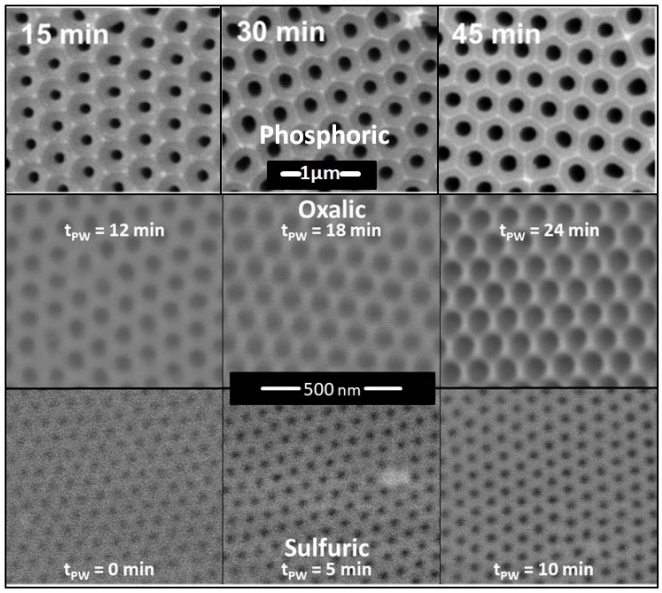

Figure 2.7: ESEM top view images of NAA produced in phosphoric, oxalic and sulfuric acid after indicated pore widening times t_{PW}.

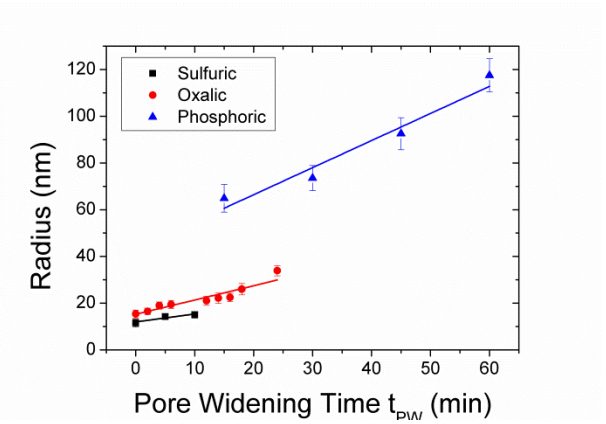

Figure 2.8: Radius increase over pore widening time t_{PW} of phosphoric, oxalic and sulfuric acid.

Pore widening rates, or hereafter referred to as increase rates (IR) depend on the acid's potency (common practice is to re-use acids for multiple pore widening steps), temperature and concentration. The outer layer of alumina contains impurities from the electrolyte and was shown to resolve faster during pore widening than the inner layer of NAA which consists of pure aluminium[9], [49].

2.2.3 Silanization of Nanoprous Anodic Alumina Pore Walls

Many applications of nanoporous structures require surface functionalizations, for instance in biomedical applications to fabricate host compatible interfaces with preserved structural integrity[50], [51], in sensing systems to retain specific target analytes[52], in stimuli-responsive drug release systems with gated nanochannels[17] or to prevent biofouling[53].

Different functionalization strategies are available for the introduction of reactive functional groups (e.g. amino, carboxyl, hydroxyl groups, etc.) to metal oxide surfaces for surface modifications, bio-conjugation or addition of further functional groups[54], [55]. Silanol chemistry is the most popular strategy for covalent immobilization of functional groups to hydroxylated surfaces by providing a bond between inorganic and organic materials[52], [56], [57]. Silane linkers offer a variety of functionalities due to different terminal functional groups and depending on the application they can facilitate the attachment of biological, organic or inorganic material[13], [15], [52], [56]–[61].

Organosilanes (figure 2.9) are silicon-based tetrahedral monomers with a main carbon chain ending in a functional or reactive group to covalently or electrostatically link to another organic molecule. Other residual side groups usually are alkoxy groups.

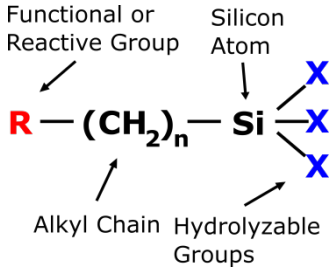

Figure 2.9: Generic structure of an organosilane with its reactive and hydrolysable groups left and right, the central carbon chain and tetrahedral silicon core.

Silanization via dip-coating is simple, fast, cheap, reproducible and produces high surface coverage and there is a multitude of commercially

available organosilanes described in the literature with distinct applications. Types of organosilanes include amino-silanes[62], PEG-silanes[53], fluorinated-silanes[63] and mercapto-silanes[64]. Of particular interest for the immobilization of biomolecules are the functional and reactive amine groups of amino-silanes [55], [58], [62], [65].

Widely popular amongst the latter silane linkers are 3-aminopropyltri(m)ethoxysilane (APTES and APTMS) which stabilize hydroxylated surfaces and are frequently used to introduce amine groups for the coupling of biomolecules such as lipids[66], DNA[67], biotin[68], BSA[52], immunoglobulins[16] etc.. Compared to other organosilanes APTES is more stable due to the lack of secondary amines which attenuates a local increase in pH and reduces Al-O-Si bond activation[69].

APTES reacts with the free hydroxyl groups (-OH) of oxidized metals by transforming silane-ethoxy (CH_3-CH_2-O-Si) groups to silanol oxygen (SiO) under the loss of ethanol (CH_3CH_2OH) [70], [71].

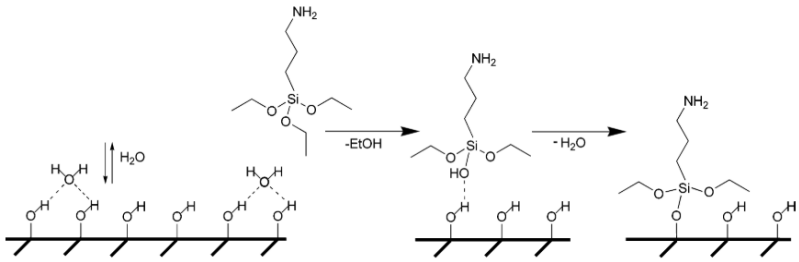

Figure 2.10: APTES hydrolysis and condensation on hydroxylated metal oxide surface [71].

Carefully following a strict dip-coating protocol allows for a homogenous coverage of an APTES monolayer with crosslinking between the organosilane monomers on the surface [65].

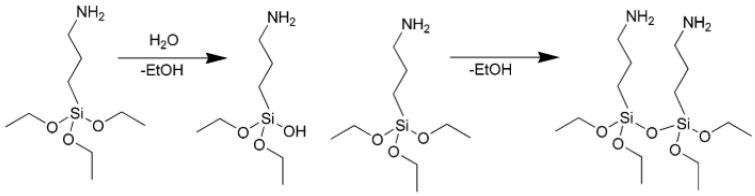

Figure 2.11: APTES crosslinking via hydrolysis followed by condensation reaction in solution phase [71].

APTES is traditionally used as the first step in a two-step process for the covalent immobilization of biomolecules but it has also been shown to bind electrostatically via its amine functional group to the carboxyl groups of amino acids [52].

Typically, though, a two-step functionalization is preferred for covalent immobilization of biomolecules via a silane linker and an additional cross-linker. Different cross-linkers with functional groups reactive towards amines, thiols, or carboxylic acids for covalent immobilization of biomolecules can be used between the activated silanized surface and the target molecule to modify the surface chemistry to the needs of the targeted conjugate [58], [72].

APTES can be used with different cross-linkers and a biotinylated derivative of N- hydroxysuccinimide (NHS) was shown to covalently bind to and immobilize streptavidin on alumina and silica surfaces[73]. A

silane linker 3-isocyanatopropyl triethoxy (ICN) silane already pre-conjugated to a cross-linker for ease of application was used for the immobilization of antibodies[59].

But the most common cross-linker used in combination with APTES is the *bis*-aldehyde glutaraldehyde (GTA). GTA forms covalent imine double bonds on either side with the protein and the linker by reacting aldehyde functional groups with amine groups of APTES and the amino acids of proteins[74].

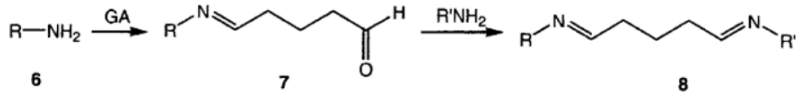

Figure 2.12: Crosslinking of GTA via imine bonding to silane linker [74].

2.2.4 Non-Covalent Immobilization Strategies for Nanoporous Anodic Alumina Functionalization

Next to covalent coupling strategies, as exemplified by the silanization techniques in the previous section, physiosorption (e.g. electrostatic, hydrophobic, intermolecular interactions or physical entrapment) and bioaffinity immobilization (avidin-biotin, protein A-antibody, affinity capture ligand, DNA hybridization, antibody or aptamers) are useful strategies for the immobilization of compounds and biomolecules onto porous materials[75].

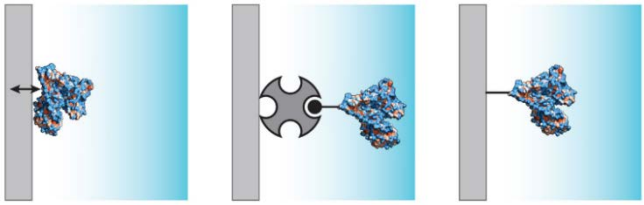

Figure 2.13:Immobilization strategies for proteins from left to right: physiosorption, bioaffinity immobilization, covalent coupling[75].

Simple Natural Adsorption via Electrostatic Interaction

Binding of protein via simple natural adsorption onto NAA surfaces via electrostatic interaction (without prior hydroxylation of NAA) through wet-chemical immobilization is probably the easiest functionalisation strategy of all. Bovine serum albumin (BSA) is a standard reference protein and blocking agent in bio-science and it is well-known to adsorb onto alumina surfaces. On alumina BSA shows a well-defined adsorption isotherm with a large pH range plateau from pH 3.5 – 9 and an adsorption maximum around its isoelectric point (IEP) of pH 5.1. Alumina was shown to have its IEP at pH 9[76]. BSA in solutions with DI water produces a pH of around pH 7 and given its IEP it is deprotonated whereas the NAA surface is protonated at this pH, providing sufficient opposing charges for electrostatic immobilization.

The durability of this immobilization strategy was demonstrated via the lack of desorption of the enzyme Invertase which was electrostatically bound to the NAA pore walls via a dip solution for 1h at 22 °C to study enzyme activity in real time via surface plasmon resonance. Only a minor decrease in relative enzymatic activity over a week due to

desorption was found. Even complete enzyme removal and NAA cleaning with guanidine and re-immobilization of Invertase was possible for up to 5 cycles without loss of immobilization loading capacity indicated by only minor differences in enzymatic activity [77].

It was previously shown that the maximum adsorption of BSA is dependent on the surface charge density of metal oxides[76] and that BSA has a higher binding efficiency in NAA functionalized with longer carbon chains of organic acids [78]. These findings demonstrate that charge density of the carrier matrix plays an important role in the adsorption of protein. Prior to adsorption of protein it is therefore common practice to increase the number of hydroxide (-OH) moieties on the NAA surface via hydroxylation (e.g. boiling NAA in 35% hydrogen peroxide (H_2O_2) for 15 min) [72].

Electrostatic Layer-by-Layer Deposition of Polyelectrolytes

Another functionalization strategy of NAA exploiting electrostatic interactions is the layer-by-layer (LbL) construction of polyelectrolyte (PE) multilayers, which allows controlling the film thickness inside the pores at the nanometer scale. It is a simple and versatile technique employing alternate dipping of NAA in PE solutions of alternating charge, thereby creating a protein friendly, gel-like hydrophilic matrix[79], [80]. The film thickness can be modified by controlling the pH and ionic strength of the PE solutions during and after the LbL deposition process while the pores remain unobstructed for up to seven deposition cycles [81]–[83].

There is a vast amount of commercially available PE on the market but the most popular PE used for LbL deposition are polyacrylic acid (PAA), polyallylamine hydrochloride (PAH), polystyrene sulfonate (PSS) and polydiallyldimethylammonium chloride (PDADMAC) [84]. ´

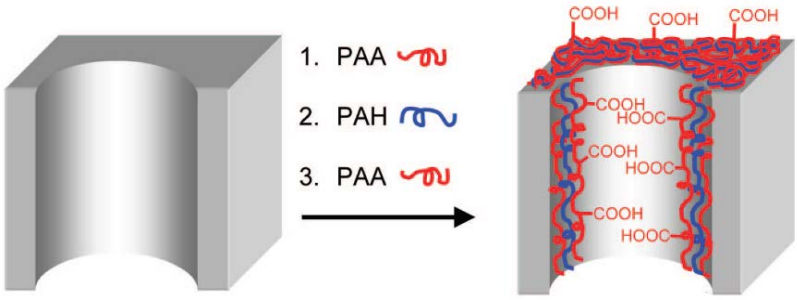

Figure 2.14: Schematic illustration of the deposition of polyelectrolyte multilayer in NAA[79].

Most applications revolve around tuning NAA pore geometries to control molecular size selective transport [81]–[83] but other work focused on resisting nonspecific binding of protein during immuno-sensing experiments[85], immobilizing citrate-coated gold nanoparticles[86] and the formation of NAA template assisted soft and flexible nanotubes [87].

Physical entrapment is also regarded as a form of physiosorption and the complex meshwork of PE multilayers provides a matrix for loading and withholding molecules. It was demonstrated that a pH adjustment from pH 2 to pH 8 after drug loading causes contractions of PE films in NAA which thereby entrapped the loaded drug. By reducing the pH the PE swelled out again and provided sufficient steric space for the outward diffusion and release of the drug [17], [88].

Bioaffinity Adsoprtion

Biospecific or bioaffinity adsorption can be regarded as a natural "key-lock system" (figure 2.15) where two or more individual biomolecules have complementary binding sites for one another. Specific binding phenomena between complementary biomolecules yield strong, highly specific, and oriented protein immobilization [89]–[91] which are reversible using chemical treatment, pH change, or heat treatment [92], [93]. Bioaffinity interactions are commonly used as a secondary immobilization step after the first target specific biomolecule was initially immobilized by physiosorption or covalent conjugation.

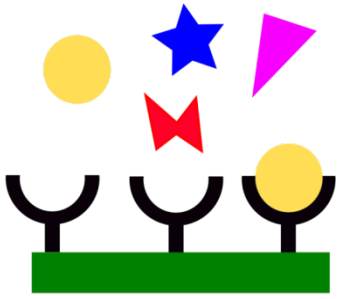

Figure 2.15: Simplified illustration of specificity of bioaffinity adsorption.

Bioaffinity Adsoprtion of Avidin and Biotin

One of the strongest known non-covalent bonds between biomolecules is found between the egg white protein avidin (or its bacterial derivative streptavidin) and the water soluble vitamin biotin (vitamin H) which allows for uniformly oriented protein immobilization [94], [95].

Avidin is a water soluble tetrameric protein with a diameter of about 5nm [96] which is stable over a wide pH and temperature range and can bind up to four molecules of biotin. Recombinant techniques have produced a range of avidin derivatives with designed qualities for specific biotechnological needs. The bond formation between avidin and biotin is very rapid, strong and unaffected by denaturation through pH or temperature changes, enzymatic degradation or organic solvents.[90]

Biotin is a small molecule found in all living cells and its conjugation to macromolecules does not affect conformation, size, or functionality. It can be chemically modified to add further functionality (e.g. conjugation with proteins or surfaces) via its carboxyl groups to form biotinylated reagents which in turn does not affect binding to avidin via the bicyclic ring[95]. Biotinylated N-hydroxysuccinimide (NHS) and hydrazide are commonly used to target amine or carboxyl groups respectively[90].

Using an NAA carrier matrix the avidin-biotin bioaffinity immobilization was used for DNA hybridization[97] and fluorescence detection of biomolecules[68] .

Bioaffinity Adsoprtion of Protein A and Immunoglobulins

Protein A (PA) is a popular immunoglobulin (IgG) immobilizing protein, extracted from the cell wall of the Gram-positive round shaped bacteria of the human skin flora *Staphyloccucs Aureus*. PA can specifically bind up to four IgG via their constant F_c region[98] thereby orientating the IgG presenting their variable F_{ab} regions to the exterior (figure 2.16), making them readily accessible for antigen binding[89].

A spacer that links PA to the planar surface is frequently used in conjunction for improved orientation, so that bound IgGs are away from the immobilization surface and more accessible to antigen binding[90]. However, PA has an IEP of around pH 5, is negatively charged at around pH 7[99] and can be electrostatically bound on bare NAA similarly to BSA as described above. With high protein stability ranging from pH 1- 12 PA immobilisation on bare NAA is therefore fast and simple and was demonstrated as feasible by several studies which detected binding of PA with subsequent detection of immunoglobulins[100], [101].

Bioaffinity Adsorption of Immunoglobulins

Immunoglobulins are the workhorse in bioanalytical laboratories around the world owing to the commercial availability of a large arsenal of different types which target different analytes with high specificity via immune-adsorption. Most commonly immunoglublin type G (IgG) are used due to their structural advantages stemming from their Y-shape architecture. In biochemical engineering the constant but animal specific bottom part of the IgG, referred to as the F_c region, is typically used for annealing and orientating the IgG on surfaces via silane coupling or as the region binding to protein A. The two top regions of the Y structure, referred to as the F_{ab} regions, are recognition centres that bind selectively to specific targets. Often secondary antibody systems are used where the specific target of a primary IgG's F_{ab} region is the F_c region of a secondary IgG from a different animal species (figure 2.16).

Demonstrating their applicability and feasibility there is a large body of scientific research available on detecting immuno-complexation reactions of IgG with target analytes in NAA[100]–[102].

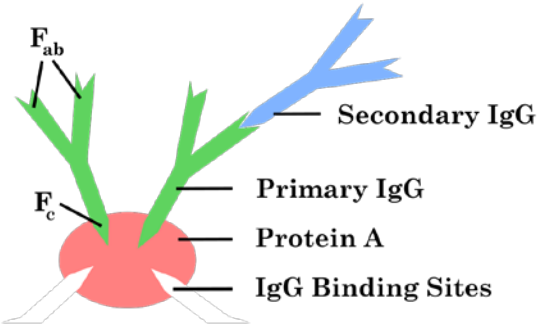

Figure 2.16: Illustration of Protein A with 4 binding sites and immobilized primary and secondary IgG.

2.3 Optical and Optofluidic Applications of Nanoporous Anodic Alumina

Studies demonstrating practical applications of the physico-chemical properties of NAA are numerous ranging from template synthesis for nano-pattern imprinting, molecular and ion separation, electrochemical sensors, catalytic nano-reactors, drug deliver and biomedical applications, to name but a few examples [13].

But of particular interest within the context of this PhD study are the optical properties of NAA. A wealth of academic research exists investigating the interaction of light with NAA and exemplifying advances in applications such as waveguides, photon-energy conversion, surface-enhanced Raman spectroscopy (SERS), surface plasmon

resonance (SPR), reflectometric interference spectroscopy (RIfS) or photoluminescence spectroscopy (PLS) [103].

2.3.1. A Brief Historical Overview

Efforts put into exploiting optical properties of thin films for the development of optical biosensors date back until the 1970s where the vast majority of research output focused on surface plasmon resonance (SPR). The advent of nanostructures made of noble metals has since then spawned new research on localized SPR (LSPR) and waveguides[104].

First successful attempts on fabricating waveguides using NAA date back to 1994 [105] and 10 years later successful applications monitoring biological and chemical modifications of pores via NAA waveguides started emerging[106].

A huge leap forward in research of optical sensing with NAA was seen when reflectometric interference spectroscopy (RIfS) was naturally adapted to NAA from porous silicon and other materials [100], [101], [107]. Conventionally, RIfS is based on the detection of effective refractive index shifts in single layered NAA upon infiltrating with analytes presented as well-resolved peaks generated by the Fabry-Pérot effect[108]. More recently Bragg reflectors[109] (multi-layered structures of a nanoporous material with periodic refractive index) were presented as a promising alternative as sensing matrix which allows monitoring of optical transmittance dip position and intensity.

The term optofluidics was introduced in 2004 [110] and represents a fairly young discipline which combines the fields of optics and fluidics at the micro- and nanoscale [111]. Monitoring the infiltration of liquid into nanoporous structures via laser interferometry has very recently been demonstrated as a novel nano-characterisation tool in nanometrology[30]–[32]. Experimentally advancing this technique towards minute modifications of the pore radius of NAA across different liquid-surface interfaces towards the development of a pore radius reduction biosensor is the scope of this PhD study.

2.3.2. Optical Properties and Applications of Nanoporous Anodic Alumina

Photoluminescence

Natural crystalline aluminium oxide is transparent and non-luminescent, whereas NAA is luminescent and absorbs light in the UV and blue light spectrum. Many studies have focused on the photoluminescence (PL) characteristics[103], [112], [113] and it was shown that PL intensity increases with the degree of pore ordering and NAA thickness [114], [115].

The maximum PL emission of NAA can generally be found between 350-450 nm and the discrete location of the luminescence band can be tuned via the anodization conditions. The acid electrolyte solution and the anodization voltage were shown to be the main discriminants of PL [116]–[119] by determining the amount of incorporated impurities (F-

centres) and ionised oxygen vacancies (F^+-centres) during the electro-chemical anodization process [113].

Oxalic acid was shown to produce the highest PL intensities which slightly increase with increasing anodization voltage. In contrast PL intensities of malonic acid decrease with increasing anodization voltage. For both acids the PL peak wavelength remains unaffected by the anodization voltage, but was shown to increase slightly with pore widening time[113]. Additionally, the PL intensities were shown to increase with increasing pore widening time indicating that NAA material composition changes over the distance from the pore [113], [120]

Post-fabrication modification can also lead to altering PL peak intensities and wavelengths. Increasing the NAA crystallinity, by thermal annealing up to 1100 °C, leads to quenching of the PL intensity and a red-shift of the peak wavelength[121]. Contrarily, ZnO nanoparticles grown inside NAA were shown to augment the PL intensity[122].

NAA grown on a polished and planar aluminium surface does not only exhibit PL but furthermore the PL peak is patterned with distinct oscillations due to the Fabry-Pérot effect [112]. Similarly to PL peak maximum and intensity, these oscillation patterns can be fine-tuned via the anodization conditions and post-anodization treatment [123]. Tuning such oscillation patterns provides unique PL signatures applicable to optical encoding and biosensing (figure 2.17).

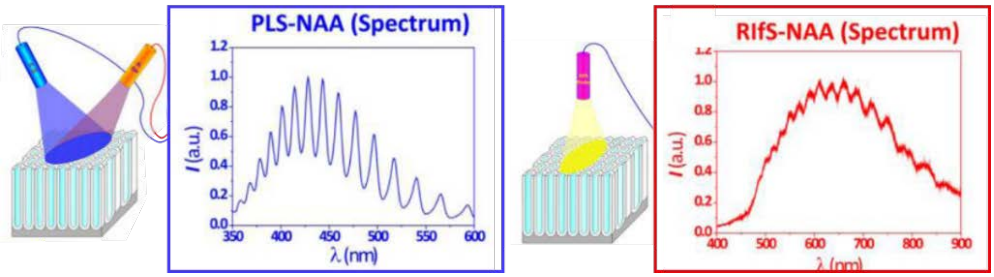

Figure 2.17: Simplified illustration of optical setup and resulting Fabry-Pérot fringes from NAA photoluminescence (left) and reflectometric interference (right), adapted from Santos et al [124].

Unique optical fingerprints could be assigned to NAA before and after the infiltration of a dye and glucose inside the pores[123]. Additionally, its thermal stability, bio-compatibility, sensitivity, high resolution and reproducibility led to numerous applications of PL based biosensors [125], [126]

The operating principle of an NAA PL biosensor is most commonly based on monitoring the infiltration and immobilization of analytes to the pore walls via PL spectrum shifts and determining an effective optical thickness change after each modification step. In this way it was possible to monitor the functionalization, activation and immobilisation of trypsin onto the pore walls[127].

NAA as an effective medium

Since the pore sizes and interpore distances of NAA are usually much smaller than the wavelength of visible light an effective medium approximation can be used to explain and model the interaction of light with the material and applications derived thereof[100], [101], [124]. If

the NAA film is very thin interference spectral patterns can be observed. These interference patterns stem from the Fabry-Pérot interference of light reflecting from the air-NAA and NAA-aluminum interfaces. [100] The wavelength of the maxima in the interference pattern is dictated by the Fabry-Pérot relationship

$$m\lambda = 2nL \tag{2.10}$$

where λ is the wavelength of maximum constructive interference of order m, n_{eff} is the effective refractive index of the porous matrix and its contents (gas or liquid filling the pore and analytes attached to the pore walls), and L is the geometric thickness of the porous thin film. The effective optical thickness (EOT) is represented by 2nL of equation 2.10 and can be obtained from the Fourier transform of the reflectivity spectrum. The interference pattern and Fourier transform of reflected white light on an NAA thin film is similar in nature to the PL oscillation pattern of NAA as they are both caused by the Fabry-Pérot effect (figure 2.17)[124].

Any modification of the pores (i.e. pore widening or immobilisation of analytes) affects the effective refractive index and ultimately changes the interference pattern which can be expressed as a change in EOT. This analysis, commonly referred to as reflectometric interference spectroscopy (RIfS), has been used to monitor gas adsorption [128], to detect circulating tumour cells[129] and it has been applied extensively for sensing within NAA and porous silica [130], [131]

2.3.3. Optofluidic Systems

After many breakthroughs in microfluidics, coupling fluidics and photonics at the micro- and nanoscale level has led to the creation of optofluidics, a relatively new scientific field which has continued to attract significant attention within the last 15 years [111]. Unique advantages of optofluidic devices permit optical and fluidic property manipulations and new optofluidic applications are steadily emerging in the areas of nanosensing[110], [132].

Optofluidic systems are dependent on the physico-chemical characteristics of a liquid within a solid or liquid carrier matrix and on the interface between them. To reduce the roughness of the underlying matrix for a more homogenous liquid flow, a fluid-fluid interface systems was described to manipulate light in waveguides, of a core liquid flowing between slabs of a cladding liquid [133]. A colloidal system using a microsphere in a microfluidic channel was demonstrated to act as an optically relocatable lens when interacting with the optical path of waveguides [134]. Moreover, as a fluid-solid interface system, the detection of analytes via refractive index changes in nanoporous platforms has become one of the most popular optofluidic sensing devices [52], [77], [100], [101]. One of the most striking advantages of the integration of optics and nanofluidics lies in the application of very small sample volumes that do not require additional labelling.

Nano-optofluidic methods have been proven sensitive for substances as small as nanoparticles, viruses[135] and even ions[64]. Furthermore, the application of NAA as a powerful optofluidic biosensing platform has

been successfully demonstrated via the detection of proteins [101], antibody-antigen complexation[100], [107] enzyme activity[77], [127], and DNA [136].

More specifically, a novel optofluidic technique exploiting capillary driven fluid imbibition and laser refractometry was presented with great potential for the non-destructive characterization of nanoporous materials in the field of nanometrology. The method exploits the fact that arrays of nanopores behave as an effective medium. Thus, laser interferometry with data acquisition can be used to follow optical property variations associated to capillary imbibition into nanoporous membranes with a narrow pore size distribution and allows to give estimations of the radius and internal geometry of the pores [30]–[32]. A variation of the well-known Fabry-Pérot interferometry served as the measurement system, which has previously been shown applicable to nanoscale fluid dynamics [137].

2.3.4. Fluid Dynamics and Capillary Driven Fluid Imbibition

The continuum of fluid mechanics describes the dynamics of capillary filling down to micro-channels and was shown to remain valid even in the nano-confinement of nano-channels with a cross-section smaller than 10nm [137]–[139]

NAA is an assembly of well-ordered, perpendicularly grown and straight pores of the same length with a narrow pore size distribution and the velocity at which a liquid invades the NAA is consequently the same in all pores. Fluid dynamics can therefore be addressed on a single pore level as a reasonable approximation for simplified calculation (figure

2.18). Pores are assumed to be symmetric along the axial direction x with a circular cross section and pore radius r(x). The pores are open at the bottom and exposed to the environment on both ends to factor out backpressure build up at the pore bottom in closed pores.

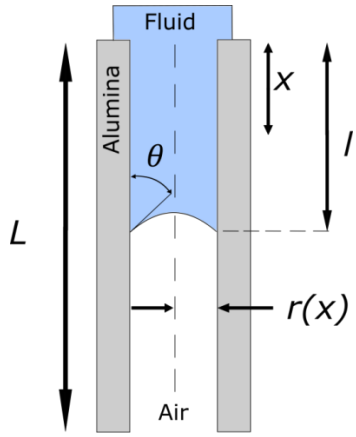

Figure 2.18: Schematic representation of a single nanopore with imbibing fluid, coordinate systems and details of the meniscus formed by the fluid in contact with alumina and air used in calculations.

Further, an incompressible Newtonian fluid in laminar flow is considered. Due to the nano-confinement very low Reynold numbers are taken into account leading to a negligible inertial forces [140] [141].

$$Re = \frac{inertial\ forces}{viscous\ forces} = \frac{\rho u L}{\mu} = \frac{uL}{\nu}, \tag{2.11}$$

where ρ is the density of the fluid, u is the velocity of the fluid with respect to the object, L is a characteristic linear dimension, μ is the dynamic viscosity of the fluid, ν is the kinematic viscosity of the fluid.

The Hagen-Poiseuille equation describes the relationship between the hydrodynamic resistance of the infiltrating fluid and the pressure gradient,

$$\Delta P = -\frac{dP}{dx} = \frac{8\mu Q}{\pi r(x)^4} \tag{2.12}$$

where ΔP is the pressure difference between the two ends and Q is the volumetric flow rate.

The hydrodynamic resistance of the displaced air is disregarded and the temperature is considered uniform. The entrance length of the fluid is minimal with respect to the large aspect ratio of the NAA pores producing a fully developed and one-directional fluid flow throughout the pores under the no-slip condition at the liquid-solid interface. [140].

When Q becomes instantly uniform due to mass conservation, integrating (2.12) from x = 0 to the travelled distance x = l results in

$$\frac{8\mu Q}{\pi}\int_0^l \frac{dx}{r(x)^4} = \Delta P \tag{2.13}$$

representing a steady state balance between capillary forces and viscous forces in nanopores with non-uniform radius. The main force driving the pore filling process is the capillary pressure described by Laplace's equation,

$$\Delta P = 2\sigma \cos\theta / r \tag{2.14}$$

where θ is the contact angle forming the meniscus at the liquid-air-solid interface.

Since the interfacial tension is inversely proportional to the pore radius it becomes extremely large in nanopores, which renders the present hydrostatic pressure negligible. The contact angle θ is regarded as constant throughout the pore filling process.

Substituting $Q = v(l)\pi r(l)^2$ where $v(l) = \frac{dl}{dt}$ is the average fluid velocity at the meniscus position and eliminating ΔP from (2.13) and (2.14) leads to the following expression for the meniscus velocity[30] ,

$$\frac{dl}{dt} = \alpha \left[4r(l)^3 \int_0^l \frac{dx}{r(x)^4}\right]^{-1} \qquad (2.15)$$

with the constant coefficient $\alpha = \sigma \cos\theta / \mu$ a characterizing the fluid properties.

Via this equation it was possible to predict the instantaneous meniscus position l(t) , for a given function r(x) via direct calculation[142]–[145]. Additionally, determining a completely unknown function r(x) from the curve of experimental data l(t) was accomplished via inverse calculation[32].

Chapter3

Experimental & Methods

Overview

In this chapter we will be presenting the fabrication process of the nanoporous anodic alumina (NAA) samples used during the optical characterization experiments. We will further present the instrumental setup, operation and data acquisition of fluid imbibition-coupled laser interferometry (FICLI), its theoretical background for the estimation of NAA pore radii and the respective data treatment. Since this thesis is principally an experimental study towards the application of FICLI as an NAA characterization technique and biosensor, initial experiments are presented here addressing the effects of different NAA architectural characteristics (e.g. pore length, open vs closed pores, sample orientation) and FICLI operational procedures (e.g. drop release height and volume).

3.1 Fabrication of NAA Membranes

Even though various optofluidic methods exist using a variety of carrier matrices, e.g. porous silicon[31], in this PhD dissertation, however, we focus exclusively on NAA fabricated following a well-established two step anodization protocol [8] . The fabrication conditions and modifications thereof are outlined in brief in the following sections as a generic introduction. More specific detail of the reaction conditions of the individual fabrications and resulting NAA characteristics will be presented in chapters 4 and 5 together with the respective FICLI experiments.

3.1.1 NAA anodization

Electro-polishing:

Aluminum foils used in this PhD dissertation were of high purity (99.999%) and a thickness of 0.5mm, obtained from Goodfellow Cambridge Ltd.. Planar surfaces of these aluminium foils are important for a homogenous and perpendicular pore growth during the electrochemical anodization. Electrochemical polishing was the method of choice to provide mirror-like surfaces of the aluminium foils throughout all following NAA fabrications. Foils were degreased with acetone ($(CH_3)_2CO$) followed by electropolishing in a mixture of ethanol (EtOH) and perchloric acid ($HClO_4$) 4:1 (v/v) at 20 V for 4 min under alternating stirring directions every minute at temperatures around 0 °C.

First Anodization Step:

NAA can be fabricated using a variety of different electrolytes, which in turn has a drastic effect on the NAA morphology and optical characteristics. During this study we focused on NAA with ordered pores in the lower size range with pore radii ranging from 5-50nm. The choice of electrolytes to achieve such small pores fell on sulfuric and oxalic acid.

A first anodization step was carried out using either a mixture of sulphuric acid (H_2SO_4) and ethanol 5:1 (v/v) at 25V and -5°C or 0.3M oxalic acid ranging from 40 V to 55 V at 5°C, depending on the desired

final pore radius and interpore distance. The anodization time accounted for 20h to obtain self-ordered arrays of nanochannels [9].

Removal of unordered pores:

As the growing nano-channels propagate from disordered to ordered arrays over time during the first anodization step, the initially disordered nano-channels had to be dissolved by a mixture of phosphoric acid (H_3PO_4, 6% wt.) and chromic acid (H_2CrO_7, 1.8% wt.) at 70°C for 3h.

Second Anodization Step:

A second anodization step was carried out using the same conditions as used during the first step. The total anodization time was determined via the linear relationship of total anodization charge and NAA thickness which is a more accurate parameter to control the desired sample thickness. A variety of sample thicknesses were investigated towards the applicability with FICLI, however, most samples were produced within the range of 50 -80 µm. To achieve these thicknesses with a necessary total charge between 1.16 – 1.94 C /mm² the anodization time typically lasted somewhere between 15-22 h.

Pore opening:

Since FICLI is based on interference of light traveling through an effective medium and laser reflection from the bottom side of alumina of NAA it was necessary to wet-chemically remove the non-anodized, non-transparent remainder aluminium from the bottom side. A mixture of $CuCl_2$-HCl (saturated) and 68% HNO_3 was used to expose the alumina

barrier layer. Furthermore, in order to avoid the build-up of gas pressure within the NAA pores upon fluid imbibition during FICLI experiments the barrier layers were removed, if not specified otherwise, leaving NAA membranes exposed to the environment on top and bottom side.

We initially removed the barrier layers following a previously described wet-chemical pore opening protocol as reported by Lillo M. and Losic D. 2009 [33]. In brief, the NAA is mounted in a half permeation cell where the barrier layer is exposed to 5% H_3PO_4 while the top side is covered with a potassium chloride (KCl) solution. In principle, as soon as the barrier layer is etched off, the effects of the infiltrating acid into the pores are reduced due to the presence of the KCl solution and thereby preventing excessive acid attack on the pore walls. Using an electrical current as a marker further allows monitoring of the pore opening process and in theory helps to determine the onset and complete opening of the pores by a rise and plateauing of the monitored current. The barrier layer removal and wet chemical pore opening of 4 different NAA produced in oxalic acid electrolyte (NAA_{Ox}) with two different thicknesses is shown in figure 3.1. and 3.2

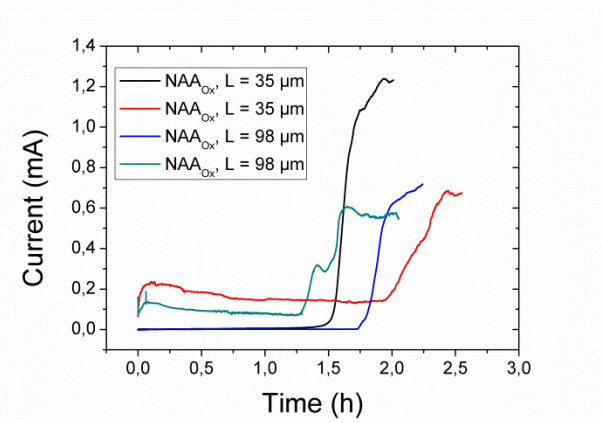

Figure 3.1 Current monitored pore opening in a half permeation cell showing the entire duration of the barrier layer removal and pore opening process.

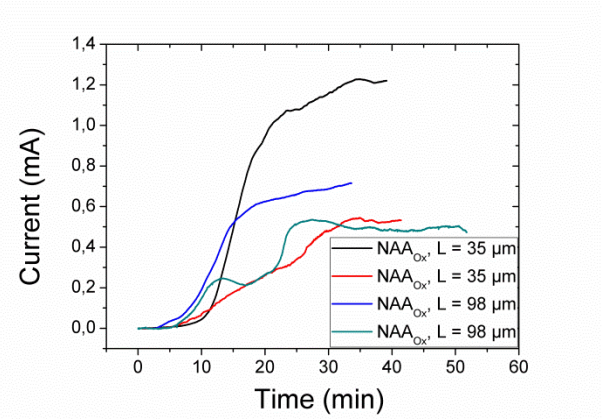

Figure 3.2 Current monitored pore opening in a half permeation cell showing the focused pore opening process.

The duration until the pores start opening is not consistent across the 4 different NAA samples, varying up to 1h. The pore open was performed at room temperature and slight temperature changes affecting the reactivity of the H_3PO_4 acid are a reasonable explanation for the

variations in pore opening time. Minute amounts of remaining aluminium on the barrier layer may also contribute to these variations. The NAA_{Ox} thickness did not show to affect the onset or duration of the pore opening process, underlining that the anodization duration does not affect the barrier layer thickness.

Similarly, the duration of the opening ranges between 15 to 35 min leaving a large margin for the acid to enter the pores and alter the pore radius. Furthermore, the pore opening was determined to be complete once a current plateau was reached for 0.5 h. Determining such a plateau is somewhat arbitrary and leaves even more time for the acid to enter and attack the pore walls.

Reducing the attack on the pore walls once the pores start to open, the KCl solution dilutes the entering acid, however, not completely neutralising it. It is therefore neither possible to accurately control this process with high precision nor to accurately reproduce the pore opening process across a number of NAA to produce NAA membranes with identical pore geometries. Figure 3.3 shows the total barrier layer removal time and resulting radius estimations obtained with scanning electron microscopy.

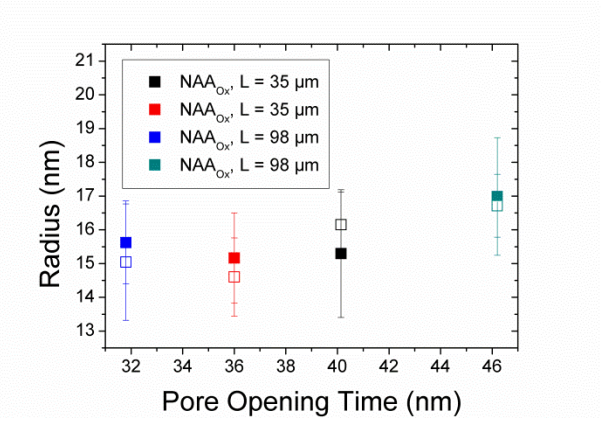

Figure 3.3: NAA_{Ox} radius estimates obtained by scanning electron microscopy after a current plateau was reached during wet chemical barrier layer removal. Solid and hollow squares are top and bottom estimates respectively.

Removing the barrier layer and opening the pores via current controlled wet chemical etching is a cheap method but controlling the parameters is somewhat arbitrary and subjective and thus does not allow reliably fabricating reproducible NAA membranes. Furthermore, the process is time consuming and with the current setup it is only possible to open one NAA at the time.

As a fast and high throughput alternative we started opening the pores with reactive ion etching (RIE) on an Oxford Instruments Plasma Technology Plasma Pro NGP80 (figure 3.4) . RIE pore opening is based on physical abrasion due to ion bombardment and by precisely controlling the physical parameters accurate barrier layer removal and pore opening provides highly reproducible results for up to 9 NAA samples at one time.

Figure 3.4: Oxford Instruments Plasma Technology Plasma Pro NGP80

The barrier layers of up to 9 NAA were removed simultaneously by 4 cycles of RIE using a mixture of 5ccms argon (Ar) and 35ccms fluoroform (CHF_3) for 5min followed by 50ccms Ar for 1min. During the process sidewall passivation occurs due to condensed polymer ($(CF_2)^n$) which was removed by a brief wet chemical etching step in 5% H_3PO_4 at 35°C for 30 seconds.

3.1.2 NAA Modification

Even though a large variety of different surface functionalizations and modifications have been reported, here we focus on a short overview of the modifications undertaken during the experiments in this PhD dissertation. However, more detail will be provided in the sections of the respective experiments in chapters 4 and 5.

Wet chemical pore widening:

Increasing the pore radius of NAA, regardless of the electrolyte they are fabricated with, is easily achieved by means of wet chemical etching in 5% H_3PO_4 at 35°C for a given pore widening time (t_{PW}). Under these conditions the pore radius is widened at a rate of approximately 1nm /min. In many of the experiments in later chapters pore widening was performed to assess the sensitivity of FICLI towards minor pore radius changes or to enhance protein infiltration into larger pores.

Hydroxylation:

NAA poses negatively charge moieties at the surface which can be exploited for biological or chemical modifications via charge interactions. The amount of charged moieties on the alumina pore walls affects the physiosorption (i.e. electrostatic interaction) of analytes to the pore walls. In order to increase the amount of negative moieties (i.e. OH^- groups) on the surface and to enhance pore wall functionalization, hydroxylating NAA in > 30% hydrogen peroxide (H_2O_2) at 70 °C for 30 min was routinely performed for all NAA before any further functionalization or immobilization steps.

Surface functionalization:

Even though a large variety of chemical surface functionalization strategies are reported for NAA in this PhD dissertation we exclusively employed the functionalization with (3-aminopropyl)triethoxysilane (APTES). After initially hydroxylating the NAA they are thereafter handled in nitrogen environment. They are immersed in 20 mL of

anhydrous toluene under stirring and 0.2 mL of APTES is added drop wise and incubated for varying amounts of time ranging from 0.5 – 4 h. A 10 min washing step in anhydrous toluene follows, still in nitrogen environment, then in toluene and deionized water at ambient environment. Afterwards, silane cross linking is facilitated by keeping the NAA in an oven at 120 °C overnight. Activating the APTES surface with glutaraldehyde (GTA) provides nitrogen binding sites particularly relevant for capturing biomolecules.

Layer-by-layer deposition of polyelectrolytes:

The desposition of polyelectrolytes has become common practice in modifying surfaces providing them with certain functionalities, such as to immobilise analytes or controlling the reaction space due their intrinsic size responsiveness on changing environments. They were shown to efficiently enter into nanopores and they can be used for the stepwise addition of layers rendering them a great tool in the arsenal of nanofunctionalization.

In this PhD dissertation we employed poly(allylamine hydrochloride) (PAH) and poly(sodium 4-styrenesulfonate) (PSS) solutions (0.5 mg/mL in 0.15 M NaCl) in which the NAA was dipped and incubated for 30 minutes, following a protocol reported elsewhere [146]. Successively dipping NAA in PAH and PSS produced one polyelectrolyte double layer given as N_{PDL}.

Biomodification – BSA, Protein A, Immunoglobulins

After increasing the negative moieties on the NAA surface via hydroxylation the immobilization of Bovine Serum Albumin (BSA) and Staphyllococcus Aureus Potein A (PA) to the pore walls is fast and easy via electrostatic forces. Simply incubating NAA in a solution of highly concentrated protein at 4 °C overnight will suffice to allow for protein infiltration inside the pores and attachment to the pore walls. Immunoglobulins are incubated identically after initially hydroxylating and incubating NAA in PA.

3.2 Fluid imbibition coupled laser interferometry

Fluid imbibition coupled laser interferometry (FICLI) is an optofluidic technique using the movement of a liquid front passing through nanoporous materials and its optical interference with a reflected laser beam to estimate the radius of the nanopore the liquid is travelling through.

3.2.1 FICLI – The Setup

Figure 3.5 shows a schematic setup used to measure light reflection from NAA membranes during fluid imbibition driven by capillary forces in real-time. Reflected light intensity is measured as a function of time, after a liquid drop is released onto the NAA. A monochromatic He-Ne laser beam is focused on the bottom side of the NAA membrane via mirrors.

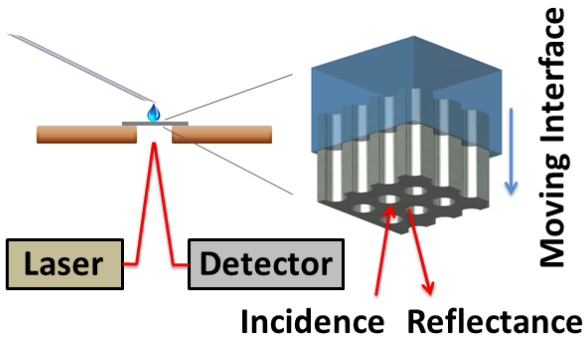

Figure 3.5: Schematic of the FICLI measurement setup.

Figure 3.6 shows the 632.8nm generated laser (1) which is redirected via a mirror (2) targeting the bottom side of the NAA. The NAA membrane (4) is fixed on a sample holder (3), allowing the NAA to rotate horizontally but held firmly when clamped down. The light reflected from the NAA membrane is redirected via a second mirror and measured by a photodetector (5). Using a 14 bits computer controlled data acquisition (DAQ) card (6), light intensity data is recorded at 48 samples per second.

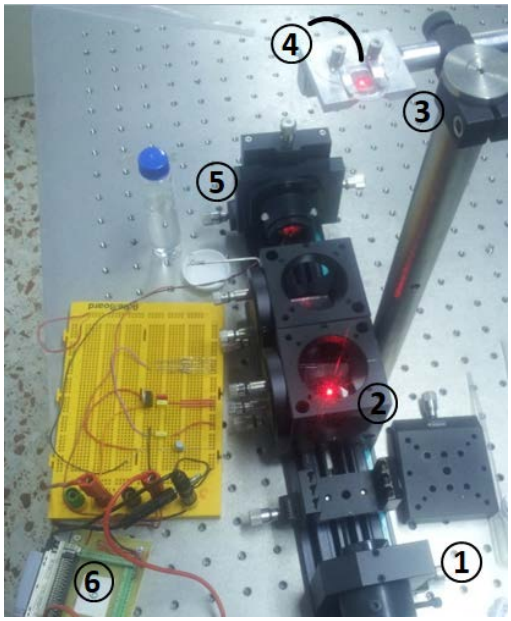

Figure 3.6: FICLI setup showing (1) the laser, (2) the mirrors, (3) the sample holder, (4) the NAA membrane, (5) the detector and (6) the DAQ.

After dropping a liquid drop from a pipette onto the NAA membrane, the fluid enters the pores driven by capillary forces and readily passes through the pores. Simultaneously, the light reflected from the NAA membrane's bottom side is measured by the photodetector. The output of the photodetector is a small current which is converted into voltage by a resistor and then recorded by the DAQ. Figure 3.7 shows a schematic illustration of the pores and fluid imbibition and its interference with the optical path.

3.3 FICLI – Optical Fundamentals

In this section we will be covering the fundamentals of light intensity fluctuations measured with FICLI and how they are treated to obtain pore radius estimates.

3.3.1 Moving liquid interface and light interferences

The light interference of a He-Ne laser beam (emission wavelength 632.8nm) reflected off the two interfaces (top and bottom) of an NAA thin film is registered as a function of time. A liquid drop is released onto the NAA and is readily drawn into the pores by capillary forces.

Figure 3.7 illustrates basic optical interference in NAA. Incoming beams are reflected off of the bottom surface (red) but also travel through the effective medium (NAA filled with air or liquid or a combination of both) to be reflected off of the top surface, travel back and interfere with beams reflecting off of the bottom surface. This optical path difference (P) (orange) is defined by the pore length (L_{pore}) and the effective refractive index (n_{eff}) of the effective medium with

$$P = 2n_{eff}L_{pore} \tag{3.1}$$

During fluid imbibition the membrane gradually fills with liquid and L_{pore} is constituted by the increasing and decreasing lengths of NAA filled with liquid (L_{liquid}) and air (L_{air}) respectively, with their corresponding effective refractive indices n_{eff_liquid} and n_{eff_air}. Fluid

moving through the effective medium causes changes in this optical path difference which can be expressed collectively by

$$P = 2\,(n_{eff\_liquid}\,L_{liquid} + n_{eff\_air}\,L_{air}) \qquad (3.2)$$

These changes in optical path difference can be translated into maxima and minima of reflected light intensity. Optical path differences equal to even integer multiples of half the laser wavelength result in constructive interferences which produce reflected light intensity maxima. Contrarily, optical path differences equal to odd integer multiples of half the laser wavelength result in destructive interferences which produce reflected light intensity minima.

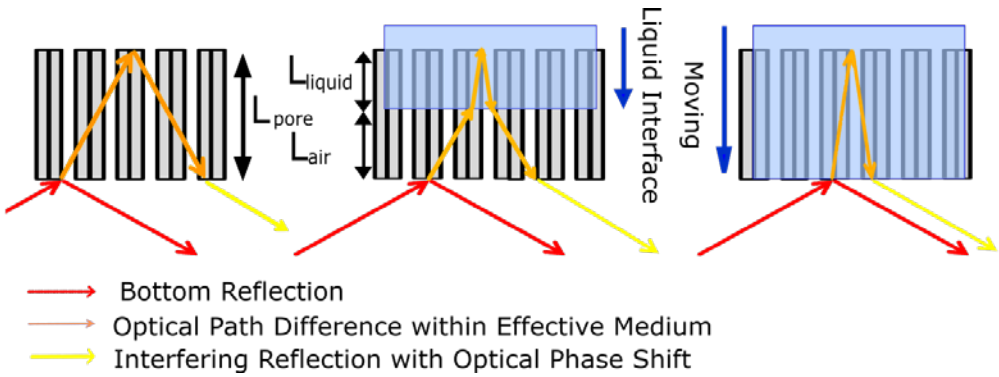

Figure 3.7: Schematic illustration of light interference due to optical path shifts is based on the changing optical path.

These successive intensity extrema are represented as time-resolved interferograms in figure 3.8 These interferograms also provide the capillary filling time (t_{fill}) given as the oscillation time span starting from

the an initial light intensity drop until the signal increases again to reach a steady plateau.

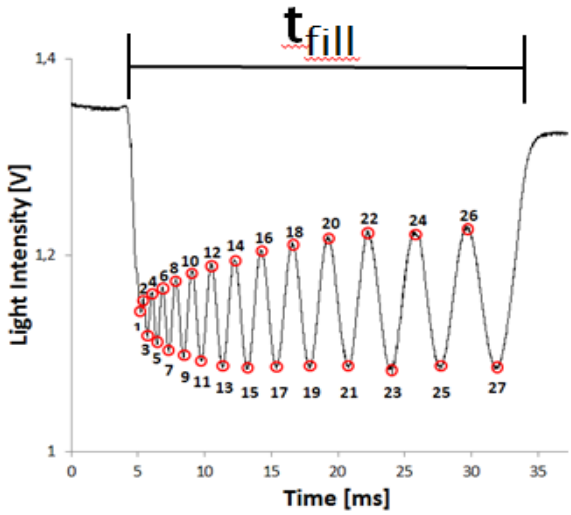

Figure 3.8: Time resolved interferogram showing light intensity maxima and minima.

Each extremum in the pattern is indexed with integers and the time of occurrence is registered. Then, the time difference between two consecutive extrema is plotted against the extremum index (Figure 3.9), giving a linear trend.

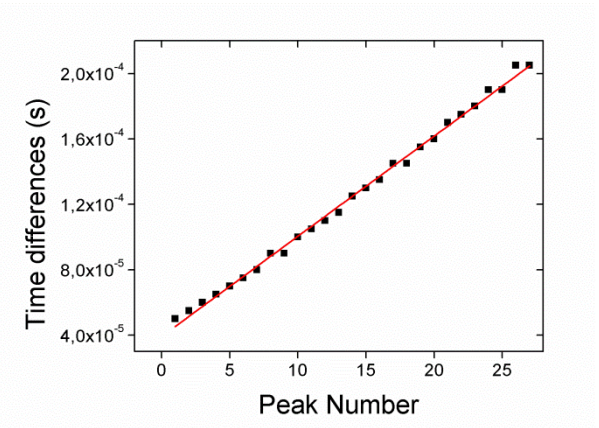

Figure 3.9: Time differences obtained from adjacent extrema plotted against their extremum indices.

The pore radius can be estimated from the slope of this linear trend (S) through the expression:

$$R_0 = \left(\frac{\alpha L_0^6}{S}\right)^{\frac{1}{6}}, \text{ with } \alpha = \frac{4\mu}{\pi^2 \gamma \cos\theta} \text{ and } L_0^3 = \frac{\lambda}{4(n_2 - n_3)\delta}, \qquad (3.3)$$

where θ is the liquid contact angle with the inner pore surface, γ is the liquid surface tension and μ is the liquid viscosity. The refractive indices of the liquid and air are n_2 and n_3, respectively, the laser wavelength is λ and the number of pores per unit of area is δ.

3.3.2. Theoretical Fundamentals for the Radius Conversion

Rearranging equation 2.15 to expresses the velocity of the fluid meniscus in nanochannels with both ends exposed to the environment as a function of the radius profile of the pore (R(x)) and of its position within the pore (x) leads to [30]:

$$\frac{dx}{dt} = \frac{\sigma \cos\theta}{4\mu R(x)^3 \int_0^x R(x')^{-4} dx'}. \tag{3.4}$$

Expressing this formula in terms of the volume filled by the liquid at a given time (V) instead of the liquid front position (x) results in:

$$\frac{dV}{dt} = \frac{1}{\alpha R(V) \int_0^V R(V')^{-6} dV'}, \text{ with } \alpha = \frac{4\mu}{\pi^2 \sigma \cos\theta}, \tag{3.5}$$

where the constant α is expressed in SI units of s/m. Even though the pores are known to be conical with a very small angle of about 0.007°[30], here we consider the pores as cylindrical with $R(V) = R_0$ as a reasonably good approximation. Equation (3.5) can therefore be reduced to:

$$\frac{dV}{dt} = \frac{1}{\alpha R_0 \int_0^V R_0^{-6} dV'} = \frac{1}{\alpha R_0 R_0^{-6} \int_0^V dV'} = \frac{1}{\alpha R_0^{-5} V}. \tag{3.6}$$

This leads to an intuitive result of capillary filling where the rate at which the volume of liquid increases inside the pore is inversely proportional to the volume already filled. The previous equation can be rewritten as:

$$dt = dV \cdot V \cdot \alpha \cdot R_0^{-5}. \tag{3.7}$$

Discretization leads to:

$$\Delta t = \Delta V \cdot V \cdot \alpha \cdot R_0^{-5}, \tag{3.8}$$

This equation will be combined with the optical measurements. The optical path difference (equation 3.1) is dependent on the effective refractive index n_{eff} which depends of the volume filled by the liquid at a given time, V. This effective refractive index can be written as:

$$n_{eff}(V) = \frac{n_1 V_{Ox} + n_2 V + n_3 V_{Air}}{V_{unit\_cell}} = \frac{n_1 V_{Ox} + n_2 V + n_3 (V_{pore} - V)}{V_{unit\_cell}}, \quad (3.9)$$

where n_1 is the refractive index of the oxide, n_2 is the refractive index of the liquid and n_3 is the refractive index of air. V_{Ox} is the volume of the oxide within the unit cell, V_{pore} is the total volume of the one pore and V_{unit_cell} is the total volume of a unit cell (thus $V_{unit\_cell} = V_{ox} + V_{pore}$). This can be reduced to:

$$n_{eff}(V) = n_1 \frac{V_{Ox}}{V_{unit\_cell}} + n_3 \frac{V_{pore}}{V_{unit\_cell}} + (n_2 - n_3)\frac{V}{V_{unit\_cell}} = n_1(1-p) + n_3 p + (n_2 - n_3)\frac{V}{V_{unit\_cell}} = n_{eff,0} + (n_2 - n_3)\frac{V}{V_{unit\_cell}} \quad (3.10)$$

With the previous expression the optical path difference can be written as a function of the filled volume:

$$P = 2 \cdot n_{eff}(V) \cdot L = 2 n_{eff,0} L + 2(n_2 - n_3)\frac{L}{V_{unit_{cell}}} V = P_0 + 2(n_2 - n_3)\frac{1}{A_{unit\_cell}} V \quad . \quad (3.11)$$

where P_0 is the optical path difference at t=0 and A_{unit_cell} is the alumina unit cell area.

In an idealized NAA structure with perfectly ordered pores the value $1/A_{unit\_cell}$ is equal to the number of pores per unit area (δ), as there is one pore per unit cell. However, since NAA is not a perfectly ordered structure δ can be approximated by counting the number of pores (N_{pores}) in a wide-field scanning electron microscope (SEM) picture and divide it by the area of picture (A_{SEM}):

$$\frac{1}{A_{unit\_cell}} \approx \frac{N_{pores}}{A_{SEM}} = \delta$$

The optical path difference is an integer multiple of half a wavelength for a given maximum or minimum, indexed i in the interferogram analysis:

$$P_0 + 2(n_2 - n_3) \cdot \delta \cdot V_i = K_i \frac{\lambda}{2}, \qquad (3.12)$$

where K_i is an integer. If a consecutive pair of extrema (maximum/minimum or minimum/maximum) is considered then K_i integers are also consecutive: K_{i+1}-K_i = 1, thus:

$$2(n_2 - n_3) \cdot \delta \cdot V_{i+1} - 2(n_2 - n_3) \cdot \delta \cdot V_i = (K_{i+1} - K_i)\frac{\lambda}{2}$$

$$2(n_2 - n_3) \cdot \delta \cdot (V_{i+1} - V_i) = \frac{\lambda}{2}. \qquad (3.13)$$

The last equation reveals that the difference in filled volume at the times of two consecutive extrema is always constant, which can be defined as:

$$(V_{i+1} - V_i) = \frac{\lambda}{4(n_2 - n_3)\delta} = L_0^3 \tag{3.14}$$

The previous can be combined with equation 3.7, by assuming that the difference in time corresponds to the difference in time between two consecutive extrema (i-th and subsequent) in the interferogram analysis, $\Delta V = L_0^3$:

$$\Delta t_i = L_0^3 \cdot V_i \cdot \alpha \cdot R_0^{-5}. \tag{3.15}$$

V_i corresponds to the filled volume at the time of the i-th maximum. From equation 9 it can be seen that the V_i is proportional to the index i:

$$P_0 + 2(n_2 - n_3) \cdot \delta \cdot V_i = K_i \frac{\lambda}{2} = (K_0 + i)\frac{\lambda}{2}. \tag{3.16}$$

This allows writing the volume V_i as:

$$V_i = V_0 + iL_0^3, \tag{3.17}$$

with the unknown volume V_0. Introducing this in equation (3.15) a linear relation between the Δt_i and the extremum index I is obtained:

$$\Delta t_i = \Delta t_0 + i \cdot L_0^6 \cdot \alpha \cdot R_0^{-5}. \tag{3.18}$$

This basic equation justifies the analysis of the time-resolved interferograms in FICLI where the measured Δt_i (y-axis) is plotted

against the extremum index i (x-axis) and a linear relationship is obtained (figure 3.2.5). This is a confirmation of the accuracy of the cylindrical pore assumption. The slope of the linear regression S is thus equal to $S = L_0^6 \cdot \alpha \cdot R_0^{-5}$, hence

$$R_0 = \left(\frac{\alpha L_0^6}{S}\right)^{1/5}.$$

3.4 FICLI – Experimental Optimization

In this section first experiments are presented showing the optimization process of FICLI while adjusting operational parameters such as drop volume, position of the laser reflection on the sample, laser reflection with and without the barrier layer and NAA thickness.

3.4.1 Effects of the Position of the Laser Reflection from NAA on FICLI Pore Radius Estimations

Occasionally there are time-resolved interferograms which produce noisy signals. During the setup stage we noticed that the cleanliness of the interfergorams is affected by the position of the reflected laser on the NAA bottom side. Some positions produce data which leads to very reproducible radius estimates whereas other positions produce higher deviations. Figure 3.10 shows pore radius estimates for NAA produced in sulfuric (NAA_{sul}) and oxalic acid (NAA_{ox}) on three different positions marked by their horizontal rotational orientation. Measurement

triplicates were made in each position and the standard deviation of results is given by the error bars.

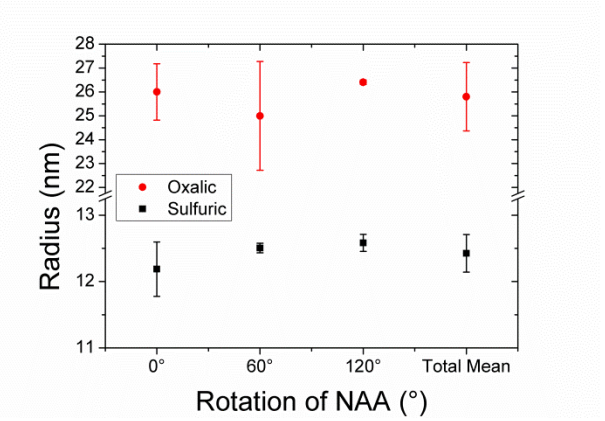

Figure 3.10: Variation of pore radius estimations depending on the relative position of the refracted laser position.

As illustrated by the largely different standard deviations on every position the reproducibility of accurate radius estimations varies with regard to the position of the reflected laser on the bottom side of the NAA. Similar findings were found for NAA produced in NAA_{ox} and NAA_{sul}.

Based on the results and in order to produce the most statistically robust radius estimations we determined the measurement procedure to include three measurement replicates each on three different positions, as described above, presenting a total mean of 9 measurements for each presentation of a radius estimation.

3.4.2 Effects of Released Drop Volume onto NAA on FICLI Pore Radius Estimations

Assuming that a larger drop of water impinging on the NAA surface produces a moving liquid front occupying more surface area, measurements may produce different interferograms and thus different radius estimations. Figure 3.11 shows the results of FICLI measurements using an Eppendorf pipette fixed on a tripod using accurate drop volumes in comparison.

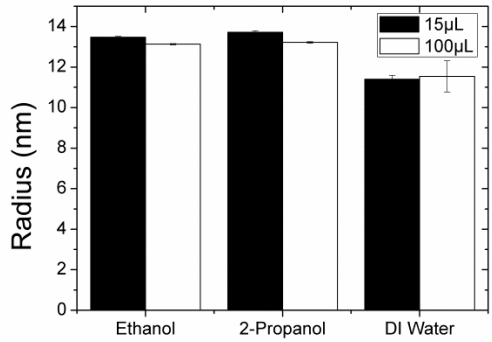

Figure 3.11: Radius estimations from time-resolved interferogram analysis of experiments performed with different amounts of liquid released onto the NAA.

The measurements using alcohol-based solvents as the infiltrating liquid produce slightly smaller radius estimations for larger drop volume, whereas the radius estimations obtained with DI water were slightly larger using a smaller drop volume. The results for the different drop volumes from the different liquids are consistent and the differences in radius estimations are negligible. Carefully controlling the drop volume for following experiments was shown not to be necessary and to

streamline future measurements a disposable plastic pipette will be used.

3.4.3 Effects of NAA Thickness on FICLI Pore Radius Estimations

In previous studies the velocity of the fluid meniscus in nanochannels was expressed as a function of the position within the pore (x) and the estimation of the pore radius was dependent on measurements of the porous medium thickness[30].

In our approach we take advantage of the fact that the volume filled by the liquid front between two consecutive time-resolved interferogram extrema is a constant to obtain a linear relationship between the index of the maximum or minimum and the time between such consecutive extrema. Such linear relationship has the advantage of permitting an estimate of the pore radius independently of the number of maxima and minima, and consequently, independently of the total length of the pore.

As shown in section 3.3.2 it became apparent that our approach to the data extraction process and conversion to radius estimates is independent from the total thickness of the NAA. Figure 3.12 below illustrates this by comparing two NAA_{Ox} with different total thicknesses of 35µm and 98µm respectively but otherwise identical anodization conditions.

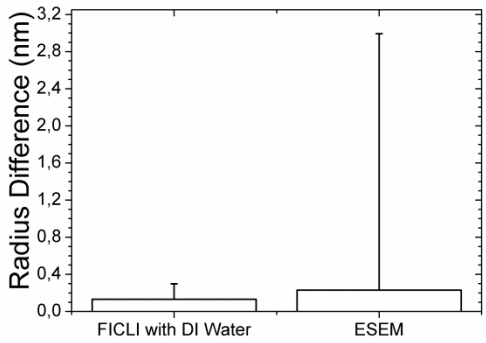

Figure 3.12: Differences in FICLI and ESEM radius estimations for two identical NAA_{Ox} with different total thicknesses of 35µm and 98µm.

The radius estimates for the two NAA_{Ox} with different thicknesses produced almost identical results with differences of 0.13 nm and 0.23 nm for FICLI and ESEM estimations respectively. FICLI estimations display a much lower variance in the radius estimations as compare to ESEM, however both results experimentally validate that radius estimations are independent from the total NAA thickness. Nevertheless, the fragility and the chance of breaking the NAA samples is enormously larger for samples with a total thickness below 50µm. For future experiments NAAs were hereafter fabricated with total thicknesses ranging from 75-100µm.

3.4.4 Effects of Barrier Layer Removal on FICLI Pore Radius Estimations

The NAA bottom side with intact barrier layer and closed pores functions as a thin film with light travelling through the barrier layer. A

barrier layer thickness of approximately 65-100 nm, for NAA_{Sul} and NAA_{Ox} respectively, is still transparent enough to not pose optical problems for optofluidic experiments. In contrast NAA fabricated with phosphoric acid and a barrier layer thickness of around 500nm did not yield sufficient laser reflection for optical measurements. Here we will be afurther ddressing the effects of the barrier layer on radius estimations using FICLI.

Figure 3.13 shows the interferograms of an NAA_{Ox} with intact barrier layer measured from the top side and the bottom side.

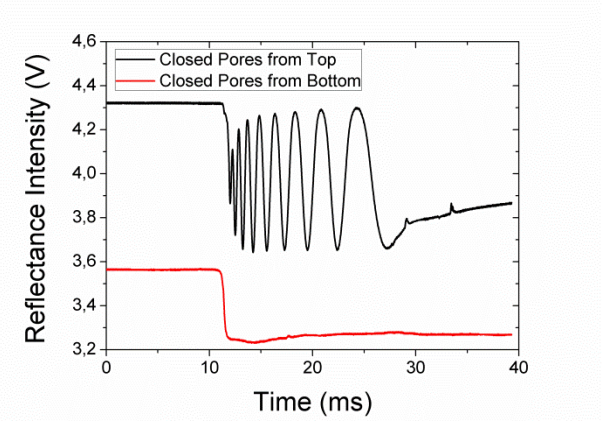

Figure 3.13: FICLI interferogram of an NAA_{Ox} with intact barrier layer measured from the top (black) and bottom (red).

To the naked eye, the black interferogram does not reveal any significant change due to the presence of the barrier layer upon fluid imbibition. As seen for the red interferogram, the sharp drop in reflectance intensity describes the moment the liquid drop impinges on the NAA surface, however, the absence of an oscillation pattern indicates that the liquid did not enter the pores, thereby not causing

light interferences. In this sense, FICLI can be used as a technique to demonstrate the presence and absence of a barrier layer or even obstructions of nanopores.

Repeating the measurements using the same NAA_{Ox} sample after removing the barrier layer and opening the pores with RIE we obtain interferograms from the top and from the bottom side of the NAA_{Ox} indicating that the pores were successfully opened, as shown in figure 3.14.

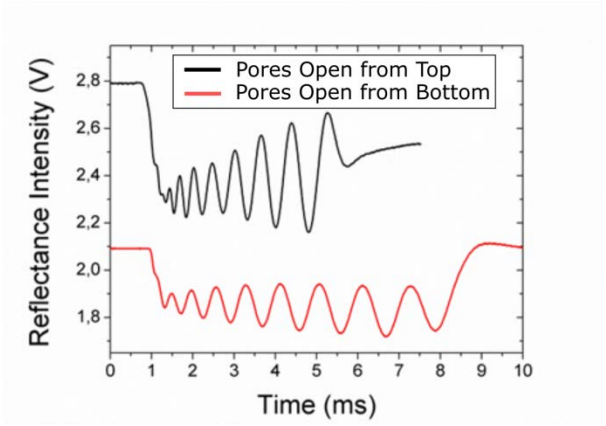

Figure 3.14: Time-resolved interferogram of a liquid passing through an NAA_{Ox} with removed barrier layer from the top (black) and bottom (red).

Even though the pores are open and the fluid imbibition was monitored successfully on either side we see that the duration of the top side imbibition is faster than the bottom one. This will be discussed in more detail in section 3.4.5.

It can be further noticed that the duration of the top imbibition after the barrier layer removal is faster (about 5 ms) than before (about 15 ms).

Since FICLI exploits the movement of a liquid front within an NAA in real-time, closed pores at the bottom skew the radius estimations due to building up gas pressure from entrapped air at the bottom which works against the capillary forces. This is visually represented by the non-linearity of the time differences versus extremum number index plots (figure 3.15) for the slope extraction during the radius estimation.

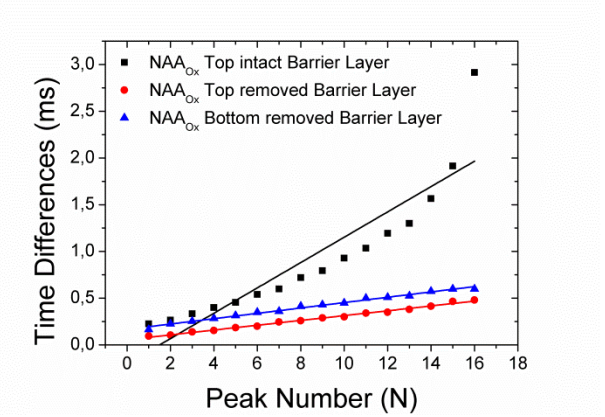

Figure 3.15: Time differences between two adjacent extrema from FICLI interferogram of an NAA_{Ox} before and after the barrier layer removal versus the extremum number index.

After removing the barrier layer, the time differences between adjacent extrema increase linearly. Due to the non-linear nature of the liquid movement when the pores are still closed extracting the slope from the linear regression is really only an approximation and leads to a radius estimation of 20.6 nm. The radius estimates after the barrier layer removal account to 25.2 nm and 24.0 nm for the top and bottom pores respectively.

The differences in radius estimations of up to 4.6 nm between closed and open pores show the necessity for open pores to obtain more reliable and accurate results.

3.4.5 Comparing FICLI Radius Estimations with Washburn Capillary Filling Radius Estimations

The driving forces behind the liquid's movement within the nanopores are largely capillary forces and other forces such as gravity can be largely neglected. Capillary filling was first described as early as 1921 by Edward W. Washburn [147] and has since been employed in many technological fields such as inkjet printing, wound dressing and food technology. It has further been adapted to nanoporous materials but its usefulness and accuracy in this field are currently still under discussion.

According to Washburn the radius of a capillary, or as in this case a nanopore, can be described by

$$R = \frac{2\mu\left(\frac{L}{t_{fill}}\right)^2}{\gamma \cos\theta}$$

,

where μ is the liquid viscosity, L is the pore length, t_{Fill} is the pore filling time, γ is the liquid surface tension and θ is the liquid contact angle with the inner pore surface.

The physico-chemical parameters of the liquids are known from the literature, the pore length as in this case the NAA thickness is directly

estimated via electron microscopy but can also be estimated via a calibration curve of total charge over time during the anodization process (Chapter 2.1.3). The pore filling time is obtained from the time-resolved interferograms (figure 3.16).

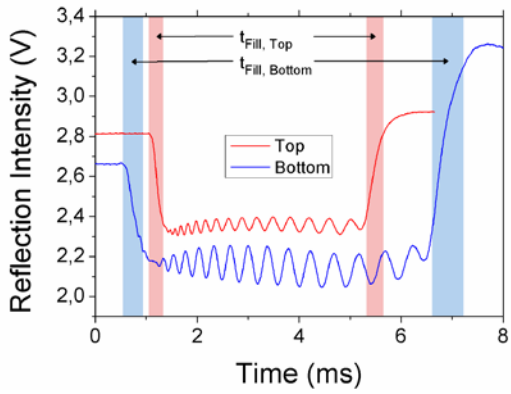

Figure 3.16: Interferogram of light intensity extrema produced by a moving liquid interface in NAA. The marked margins represent the beginning and end of the pore filling measured from the top (red) and bottom (blue).

The beginning and end of capillary filling is marked by a sudden drop and rise in reflection intensitiy. However, as highlighted by the red and blue margins in figure 3.16 determining the exact beginning and end of capillary filling is somewhat ambiguous. For instance, the initial drop in signal may relate to the impinging and dispersal of the liquid on the surface and the onset of the oscillation pattern may be the beginning of the liquid movement inside the pores. Similarly, the end of the oscillation pattern may mark the arrival of the liquid front at the pore end and the rise in signal may be dispersal of the liquid across the bottom surface of the pore. Whether the duration of this initial drop and

final rise reflects the liquid movement inside the pores is in question. For the following radius estimations we determined the first moment the signal drops and starts to rise again as the reference time points for the beginning and end of the pore filling process. The top and bottom pore radius of three NAA_{Ox} fabricated under identical conditions are estimated using the Washburn equation, FICLI and ESEM and are shown in figure 3.17.

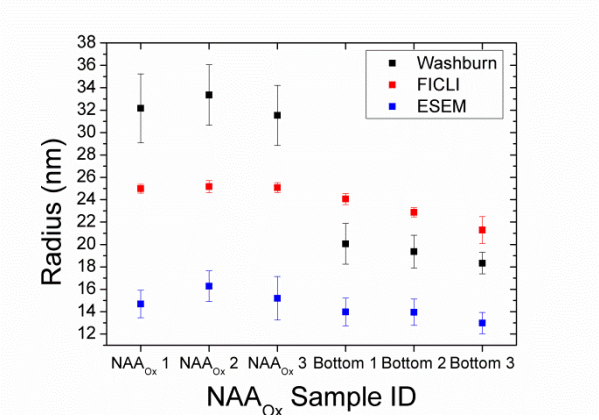

Figure 3.17: Top and bottom pore radius estimations of three NAA_{Ox} fabricated under identical conditions using the Washburn equation, FICLI estimations and ESEM estimations.

By extracting the pore filling time and using the Washburn equation the radius estimations show the largest deviation of measurement replicates and a difference of 12 nm between the top and bottom pore radius estimations. The ESEM radius estimations show slightly smaller deviations of measurement replicates compared to Washburn estimations, however, the results for top and bottom radius estimations are consistent with only a minor difference of about 3 nm. The FICLI radius estimations show the smallest deviations of measurement

replicates of the three methods and, compared to ESEM, similarly consistent results for top and bottom pore radius with a marginal difference of about 4 nm. The FICLI pore radius estimates are about 10nm larger than the ESEM estimates and this difference is attributable to the physico-chemical parameters in use, which will be discussed in Chapter 4. Similar physico-chemical parameters were used for the Washburn estimations, however, additional NAA thickness estimations from ESEM and the filling time extracted from the interferograms cause these larger discrepancies compared to the other two methods. In conclusion FICLI produced the fastest and most reproducible results of the three methods.

Additionally FICLI brings along an advantage of producing robust and reproducibly accurate results when dealing with noisy data as shown in figure 3.18.

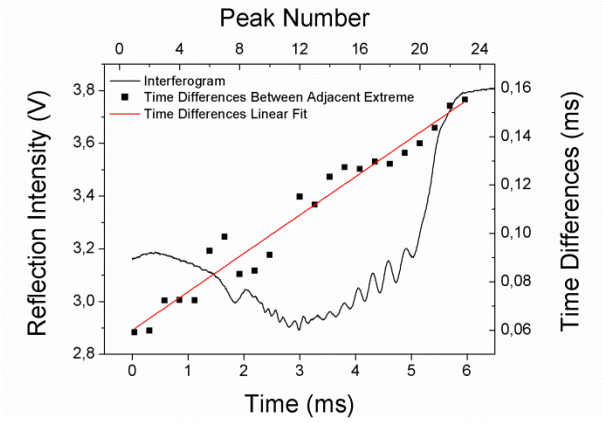

Figure 3.18: Noisy time resolved FICLI interferogram (primary axes) and extracted time differences of adjacent extrema plotted versus the extremum index (secondary axes).

The above presentation of a noisy interferogram is in part an example for the explanation of the large deviation in Washburn pore radius estimations. The beginning and end of capillary filling are more ambiguous to interpret than the FICLI time differences extracted from the light intensity oscillation extrema.

3.4.6 Pore Radius Estimations from the Top and Bottom Side

In a previous study it was shown that the top and bottom pore radius are not identical and that NAA are not perfectly cylindrical but conical with a slight angle [30]. We also find varying differences between top and bottom pore radius estimates which account to about 3 nm, illustrated in figure 3.19.

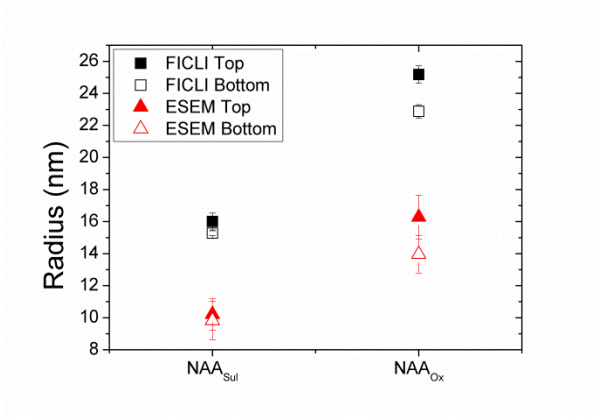

Figure 3.19: FICLI and ESEM top and bottom pore radius estimates for an NAA_{Sul} and NAA_{Ox}.

FICLI and ESEM pore radius estimates of an NAA_{Sul} and NAA_{Ox} are shown highlighting the differences between top and bottom pore radius estimates. The differences of 0.7 nm and 2.3nm between the FICLI NAA_{Sul} and NAA_{Ox} top and bottom estimates are very small and similar

to the differences estimated by ESEM of 0.4 and 2.3 nm respectively. Over an NAA thickness of 75μm this difference in pore radius produces an angle of 0.0005° - 0.0017°, which is so small that along this PhD dissertation we refer to the pores as cylindrical. We assume that the top and bottom pore radii change equally upon modification and that the initial difference will not affect the estimates of pore radius changes in later experiments.

3.4.7 Summary of the Physico-Chemical Parameters used for FICLI Pore Radius Estimations

Since FICLI is a method to estimate the pore radius which includes a 5^{th} power law, using accurate figures for the physico-chemical parameters employed during the conversion is of utmost importance. Many of these parameters are well described and accurately determined in the literature such as refractive indices, liquid viscosities and surface tensions, table 3.1.

Other parameters extracted from the literature were employed with caution, such as the liquid-surface contact angle within the nano-confinement, as they are still under debate. Where possible, we relied on the literature, but where necessary we estimated contact angles on glass slides modified similarly as the NAA with a surface tension measurement system using the sessile drop method and used the results as approximations during the radius estimations. Table 3.2 summarises contact angles obtained via a goniometer and the literature where indicated with subscripts.

Table 3.1: Values of the parameters for the different liquids used in the experiments and considered in the estimation of pore radius.

	Viscosity [Pa·s]	Surface tension [mN/m]	Refractive index
Ethanol	0.0012	22.31	1.361
2-Propanol	0.00226	21.74	1.379
Deionised water	0.001	72.75	1.333
0,15M NaCl	0.00105	73.20	1.335
Air			1
Alumina			1.77

Table 3.2: Contact angles for FICI radius estimations obtained from the literature and goniometer

		Contact Angles [°]	
Liquid	Surface modification	NAA_{Sul}	NAA_{Ox}
Ethanol	None	60.0 [148]	
2-Propanol	None	53.5 [148]	
DI Water	None	65.8 [148]	73.3 [148]
	PSS	40 [146]	40 [146]
	BSA	47	47
	Protein A	49	49
	IgG	60	60
	APTES+GTA	65	65

Since the self-ordering of NAA and the arising honeycomb-like arrangements of perpendicular nanochannels is highly reproducible and controllable by the anodization conditions there is no need to collect the

NAA geometry parameters for every fabricated sample. The used anodization conditions and the resulting NAA geometrical characteristics are given in table 3.3.

Table 3.3: Anodization conditions and resulting NAA geometrical characteristics

Anodization Voltage	Electrolyte	Interpore Distance D_{int}	Pores / m²
40 V	Oxalic Acid	100 nm	1,1547 E+14
50 V	Oxalic Acid	140 nm	5,89133 E+14
25V	Sulfuric Acid	65 nm	2,73 E+14

3.5 Summary

In this chapter we addressed the fabrication of NAA membranes and how we modified and fucntionalized the surfaces of the pore walls. The FICLI set up and basic foundation of monitoring fluid movement within nanopores in real time and the subsequent pore radius estimation procedure were presented. In an experimental approach we discussed limitations and possibilities of FICLI and its advantages over alternative methods. With the considerations made in this chapter we established a FICLI measurement protocol for the following experiments. FICLI pore radius estimates are robust and reproducible and ready to be applied in large experiments in the following chapters.

Chapter 4

Optical monitoring of capillary filling dynamics variation for the characterisation of nanoporous anodic alumina membranes

Chapter overview:

As described in Chapter 3 a pore radius estimate of NAA can be obtained via mathematical extrapolation of monitored distinct light interference patterns caused by the movement of a liquid front within the nanopores. In this chapter we employ FICILI as a pore radius characterization tool to estimate the pore radius of straight and multi-layer pores and subsequent structural modifications. We investigate the sensitivity of FICLI towards small pore radius increases to obtain a quantitative pore radius change detection limit. We do so by estimating the pore radius of NAA before and after a series of pore widening steps.

We also look at the transferability of this method to different liquid-surface interfaces by using different liquids as the moving liquid interface or using NAA fabricated with different anodization electrolytes, i.e. sulfuric or oxalic acid. When using different liquids or carrier matrices, the changes of physico-chemical parameters of the liquid-surface interface have to be incorporated into the radius extrapolation accordingly. The effects of these adaptations are further addressed in this chapter. Finally we fabricated NAA bilayers and trilayers to investigate FICLI to characterize NAA with somewhat more complex internal geometries as compared to straight cylindrical pores.

4.1 A Side by Side Comparison of ESEM and FICLI as Pore Radius Estimation Techniques

In this section we are initially distinguishing between different pore radii of NAA fabricated in sulfuric and oxalic acid before and after a

series of pore widening steps. Environmental scanning electron microscopy (ESEM) accompanied the FICLI measurements before and after each widening step for a comparison of the methods.

4.1.1 Estimating Pore Radius Changes of an NAA Produced in Sulfuric Acid Electrolyte after a Series of Pore Widening Steps

Figure 4.1 a and b show ESEM images of the top surface of NAA produced in sulphuric acid electrolyte (NAA_{sul}) before and after a pore widening step in 5% H_3PO_4 at 35°C for the pore widening time (t_{PW}) of t_{PW} = 0 min and t_{PW} = 6 min, respectively. The pictures show well-ordered pores in a hexagonal honeycomb-like distribution. Figure 4.1 c and d show the membrane cross section (membrane thickness of 56 µm) with a homogenous perpendicular growth of pores from top to bottom. ESEM image analysis revealed estimated average pore radius $r_{pore,0\ min}$ = 14.5 nm ± 1.1 nm at t_{PW} = 0 min and $r_{pore,6\ min}$ = 17.6 nm ± 1.1 nm at t_{PW} = 6 min. Average pore radii and the interpore distances, estimated to $d_{int,sulphuric}$ = 66.4 nm ± 3.9 nm, are presented in figure 4.2.

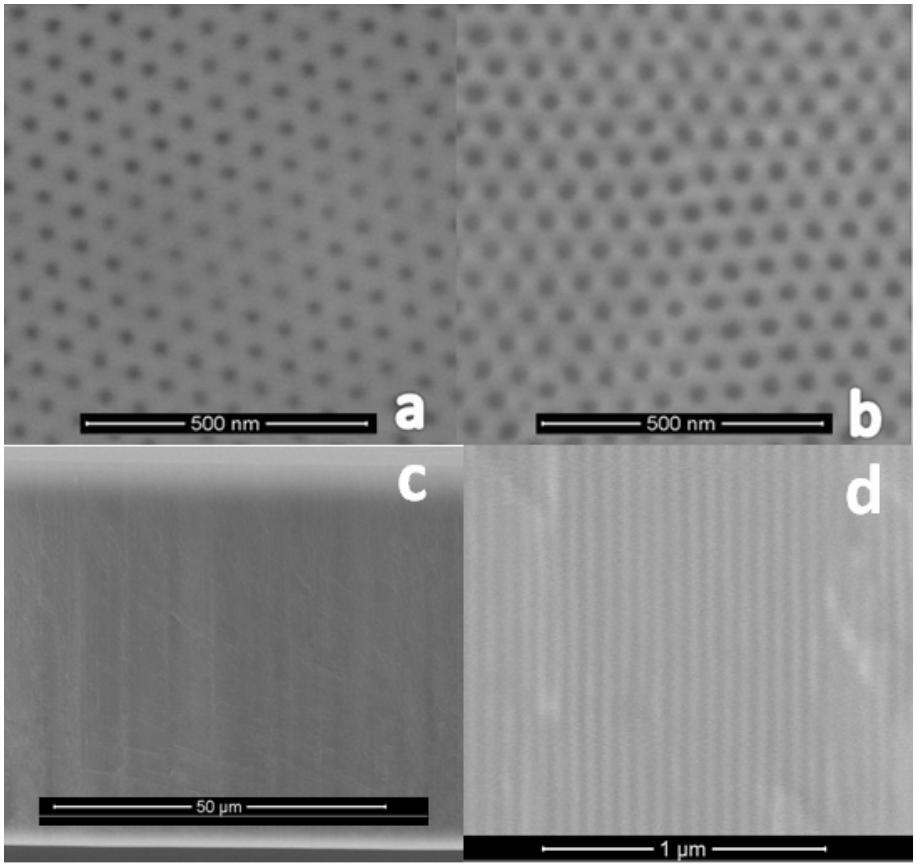

Figure 4.1. (a) ESEM images of NAA produced in sulfuric acid at pore widening time t_{PW} = 0min, **(b)** t_{PW} = 6min and membrane cross section showing the entire NAA thickness **(c)** and higher magnification showing the perpendicular pores **(d)**.

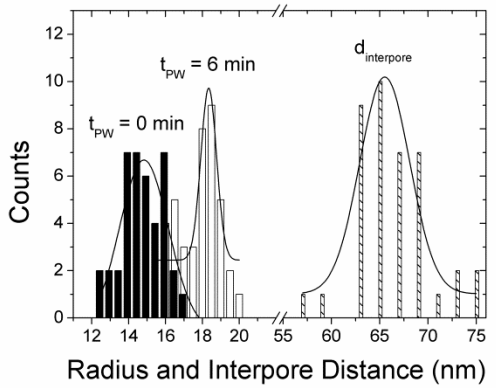

Figure 4.2: Pore radius distribution estimated by ESEM image analysis for NAA produced in sulfuric acid electrolyte at t_{PW} = 0 min. and 6 min and interpore distance.

ESEM provides a first rough estimate for pore radii, however, as it is apparent from the low image resolution and the rather wide size distribution of estimated pore radii from the respective image analysis, the selection of the grey cut off point from where to measure the radius is somewhat subjective and is heavily influenced by the images' contrasts and are therefore not a very accurate measure.

Figure 4.3 shows the estimated pore radius, as a function of pore widening time, obtained by FICLI, using deionised water (DI water) in the same NAA_{sul} membrane present in figures 4.1 and 4.2 above.

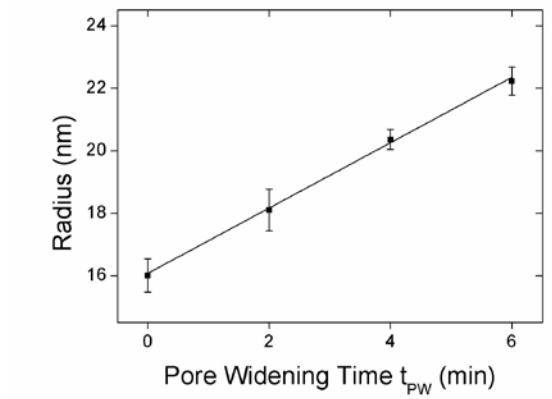

Figure 4.3. Estimated pore radius obtained with FICLI using deionized water as a function of pore widening time t_{PW}.

The values of the parameters in eq. (3.3), introduced in chapter 3, for the liquids and NAA samples employed for the estimation of pore radius are specified in table 4.1 below.

Table 4.1: Physico-chemical paramaters used for the radius estimation of NAAsul using FICLI with deionised water.

	NAA_{sul} Contact angle [°]	Viscosity [Pa·s]	Surface tension [mN/m]	Refractive index
Deionised water	65.8 [148]	0.001	72.75	1.333
Air				1
Alumina				1.77

The estimated pore radius for the as-produced sample is $r_{pore,0min}$ = 16.0 nm ± 0.5 nm at t_{PW} = 0 min. Consecutive pore widening steps (t_{PW} = 2, 4, 6 min.) lead to a linearly proportional increase in estimated average pore radius, as indicated by the trend line in figure. 4.3. The slope of this trend line reveals that the pore etching rate is $r_{etch,\ DI}$ = 1.05 nm/min. ±

0.11 nm/min. These results are validated by the values shown in the histogram in figure 4.2 of pore radius values estimated from the ESEM pictures in figure. 4.1 above. The result shows a good agreement between the two techniques.

This result is also in good agreement with previously reported etching rates investigated by ESEM and AFM image analysis[101], [149] and underlines the accuracy and sensitivity of FICLI for nanopore characterization. The error bars in figure 4.3 corresponding to the standard deviation for all the measurements of the particular pore widening steps, indicate that the uncertainty in pore radius is at most 1.7 nm, which further illustrates the accuracy of the method.

It was previously shown that the material NAA gradually gains purity from the surface material towards the material within the NAA[113]. With the consistent etching rate over the course of the power widening time of up to 6 minutes we demonstrated that these changes in NAA purity do not sufficiently affect the parameters determinining the liquid-surface interface and can be disregarded for the radius estimation using FICLI.

Figure 4.4 shows the time-resolved interferograms and the corresponding analysis of the time differences versus extremum order index, for one of the measurements of each pore widening time. The graphs show that in all cases, the filling dynamics are uniform and the linear fits have good regression coefficients. This result confirms a uniform imbibition of the pores and the absence of pore blockage.

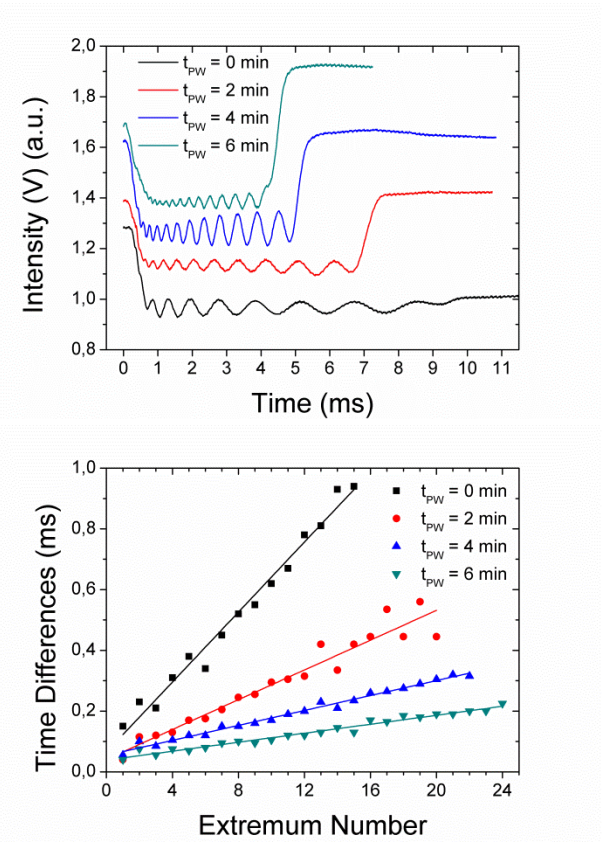

Figure 4.4: (top) Time-resolved interferograms and (bottom) corresponding plots of time difference between two consecutive extrema versus extremum number for one measurement after each pore widening step of an NAA produced in sulfuric acid.

4.1.2 Interfacing an NAA Produced in Sulfuric Acid with Different Liquids and Its effects on FICLI pore radius estimations

Addressing the consistency of the method, figure 4.5 top and bottom shows the results of pore radius estimations of a sulfuric acid NAA

(NAA_{sul}) with FICLI for the consecutive pore widening steps from section 4.1.1, using different liquids. Figure 4.5 top depicts the percentage deviation of the pore radius estimated using ethanol or 2-isopropanol with respect to the pore radius estimated with DI water shown in figure 4.4. The error bars in figure 4.5 top represent the standard deviation of the measurement replicates for ethanol and 2-propanol.

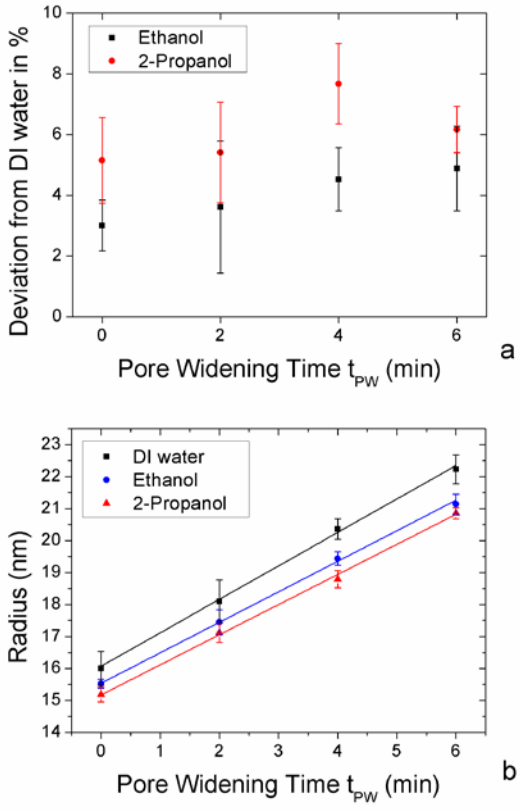

Figure 4.5: (top) Percent deviation of estimated pore radius obtained with ethanol and 2-propanol relative to the estimated pore radius obtained with DI water as a function of pore widening time t_{PW} for an NAA fabricated in sulfuric acid electrolyte. **(bottom)** Estimated pore

radius obtained with FICLI using deionized water, ethanol and 2-propanol as a function of pore widening time t_{PW}.

Table 4.2: Physico-chemical paramaters used for the radius estimation of NAA_{sul} using FICLI with ethanol and 2-propanol.

	NAA_{sul} Contact Angles [°]	Viscosity [Pa·s]	Surface Tension [mN/m]
Ethanol	60.0 [148]	0.0012	22.31 [150]
2-Propanol	53.5 [148]	0.00226 [6]	21.74 [150]

The estimated radius using a given liquid corresponding to a set of replicates were first normalized with respect to the corresponding average pore radius obtained for DI water, then, the error bar was computed as the standard average of these normalized values. Small discrepancies between the pore radius estimates for the different liquids were found. However, these discrepancies are constant for all the pore widening times and present variations in pore radii between 3 - 5 % using ethanol and between 5 - 8 % using 2-propanol. The pore etching rates obtained with ethanol of $r_{etch,Ethanol}$ = 0.95 nm/min ± 0.05 nm/min. and 2-propanol of $r_{etch,\ 2\text{-}Propanol}$ = 0.94 nm/min ± 0.05 nm/min, presented in figure 4.5 bottom, are consistent with the pore etching rates obtained with DI water.

The observed discrepancy of the estimated radius for the different liquids is probably caused by the fact that the values of the different liquid parameters (i.e. viscosity, surface tension and contact angle) considered in equation (3.3) to estimate the radius do not correspond to the actual values in the experimental conditions. Previously reported

changes in liquid properties in nano-channels, as opposed to (micro) capillaries, might in part explain the variation of the estimated pore radii between the liquids. For example, opposed to bulk material, higher viscosities of aqueous liquids have been reported due to the nanometer range of nanochannels[151] and their rectangular geometry[152]. Furthermore, direct effects of pore radius on the liquid contact angle were reported[153]. Nonetheless, our presented results have proven reproducible and pore etching rates acquired using different liquids are in good agreement with previously reported etching rates obtained by different methods [36], [101], [114], [149], [154].

4.1.3 Interfacing an NAA Produced in Oxalic Acid with Different Liquids and Its effects on FICLI pore radius estimations

Substituting the composition of the carrier matrix is another means of exploring the effects of changing the liquid-surface interface during imbibition experiments. Similar to the NAA_{sul} characterized above we addressed the incorporation of different physico-chemical parameters of an NAA fabricated with oxalic acid (NAA_{ox}) and the respective liquids in use.

Figure 4.6 top and bottom show the results of pore radius estimations of NAA_{ox} samples with FICLI for a wider range of consecutive pore widening steps. Figure 4.6 top depicts the percent deviation of ethanol and 2-propanol with respect to the values obtained with DI water. The error bars in figure 4.6 top represent the standard deviation of the measurement replicates for ethanol and 2-propanol.

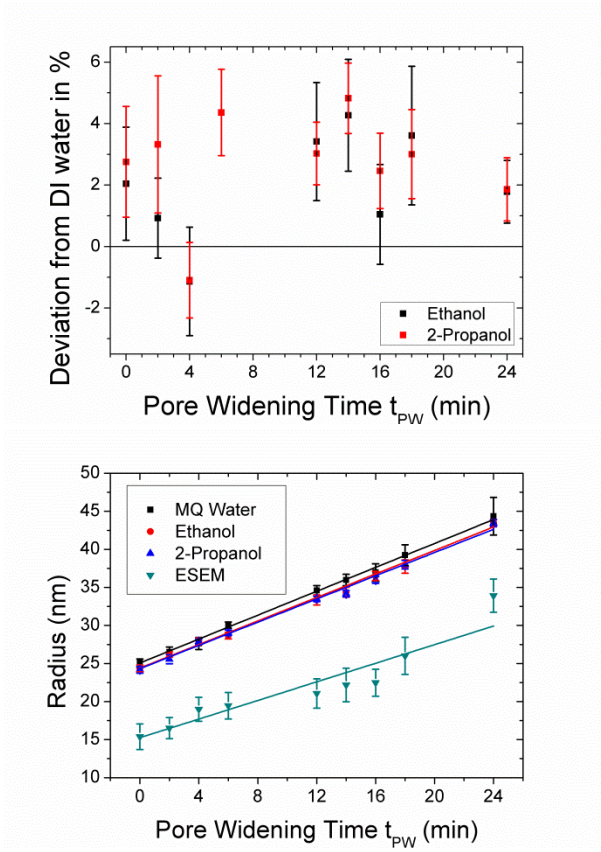

Figure 4.6: (top) Percent deviation of estimated pore radius obtained with ethanol and 2-propanol relative to the estimated pore radius obtained with DI water as a function of pore widening time t_{PW} for an NAA fabricated in oxalic acid electrolyte. **(bottom)** Estimated pore radius obtained with FICLI using deionized water, ethanol and 2-propanol as a function of pore widening time t_{PW}.

The contact angles of 69.2° necessary for the NAA_{ox} - ethanol and NAA_{ox} - 2-propanol interface were adapted from the literature [148].

The estimated pore increase rates (IR) of $IR_{ox,\ Ethanol} = 0.77 \pm 0.02$ nm/min ($R^2 = 0.99$), $IR_{ox,\ 2\ Propanol} = 0.76 \pm 0.02$ nm/min ($R^2 = 0.99$) and $IR_{ox,\ DI} = 0.78 \pm 0.04$ nm/min ($R^2 = 0.99$) are similar to the ones estimated for the NAA_{sul} and to literature values. The pore radius estimates over a long pore widening time range with a maximum of $t_{PW} = 24$min resulted in good linear correlation coefficients for the three liquids. This shows even more drastically that the change in NAA purity throughout the wet chemical etching process, from acid electrolyte anion-contaminated outside walls to pure AlO_2 deeper within the sample material, does not sufficiently alter the liquid-surface interface to skew the radius estimations.

The deviations of the pore radius estimates obtained with different liquids are more congruent for the NAA_{ox} samples than for NAA_{sul} with a marginal variation of up to only 6%. This indicates more accurate literature values of the NAA_{ox} physico-chemical parameters of the liquids-solid interface in use during the estimation of pore radius from the analysis of the time-resolved interferograms.

ESEM images were taken after every pore widening step for a more coherent comparison of pre radius increase rate estimates obtained with FICLI. The consecutive ESEM images are shown in figure 4.7 below and the resulting pore radius estimate from image analysis are presented in figure 4.6 (bottom) above. The radius estimates show a larger standard deviation than the estimates obtained by FICLI which can be explained by the difficulty to adjust exact objective cut off values for the radius estimations from the images, as can be noted by the poor image resolution in figure 4.7. This in turn is also the probable cause of the

slightly lower pore radius increase rate estimated via ESEM image analysis shown in figure 4.6 (bottom).

Similarly, the discrepancies between ESEM and FCILI estimates are somewhat large (up to 10nm) and the aforementioned arbitrary nature of choosing ESEM grey values contributes to this, however, an overestimation of the radius via FICLI is also a possibility explained by inaccurate physico-chemical properties from the literature or changing properties within the nano-confinement. Nevertheless, the estimations of radius changes via FICLI is very accurate and reproducible.

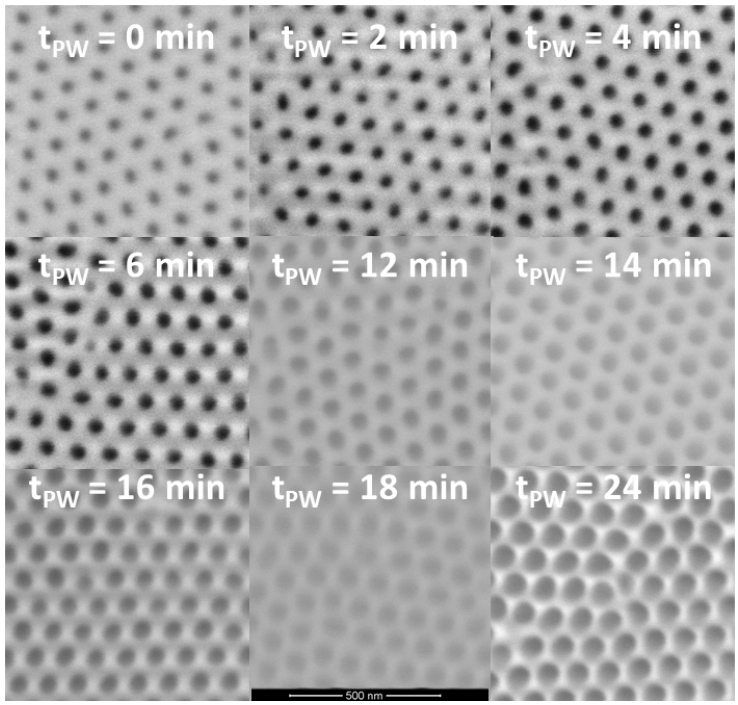

Figure 4.7: Top-view ESEM Images of NAA produced in oxalic acid electrolytes after a series of pore widening steps with pore widening times t_{PW}.

4.1.4 Contrasting Radius Estimations Obtained by ESEM Image Analysis and FICLI Time-Resolved Interferogram Analysis of NAA Produced in Oxalic and Sulfuric Acid

Since we found minor discrepancies between NAA_{ox} and NAA_{sul} radius estimates and their complementary ESEM image analysis the following sub-section focuses on more detail towards contrasting the two.

To verify the fabrication process of NAA, traditional characterization methods (ESEM) served to confirm and highlight the efficacy and working range of FICLI on NAA with non-modified inner pore surfaces. Figure 4.8 shows, from left to right, top-view ESEM images of NAA fabricated in oxalic (top) (NAA_{ox}) and sulfuric (bottom) (NAA_{sul}) acid electrolytes followed by wet chemical etching for the durations of t_{PW} = 12, 18, 24 min. for NAA_{ox} and t_{PW} = 0, 5, 10 min. for NAA_{sul}.

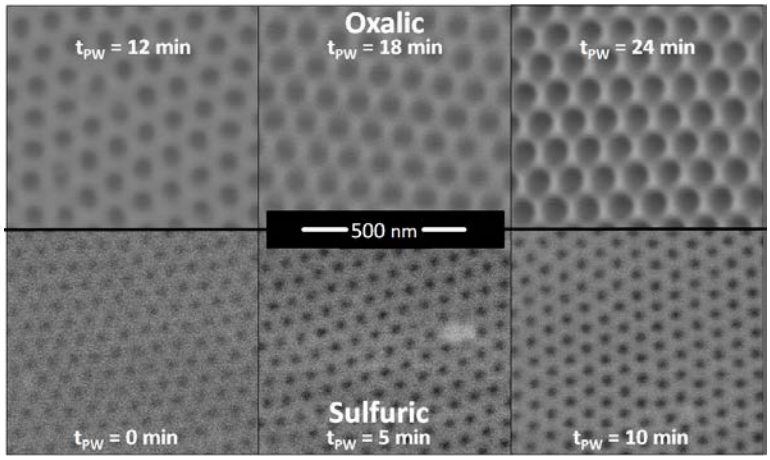

Figure 4.8: Top-view ESEM Images of 6 NAA produced in oxalic and sulfuric acid electrolytes and after the indicated pore widening times, t_{PW}.

Their respective average pore size distributions were obtained by image analysis and are presented in the form of histograms with Gaussian fits in figure 4.9, top. The average pore radius estimated by ESEM image analysis were plotted as a function of pore widening time and compared with FICLI estimates in figure 4.9, bottom.

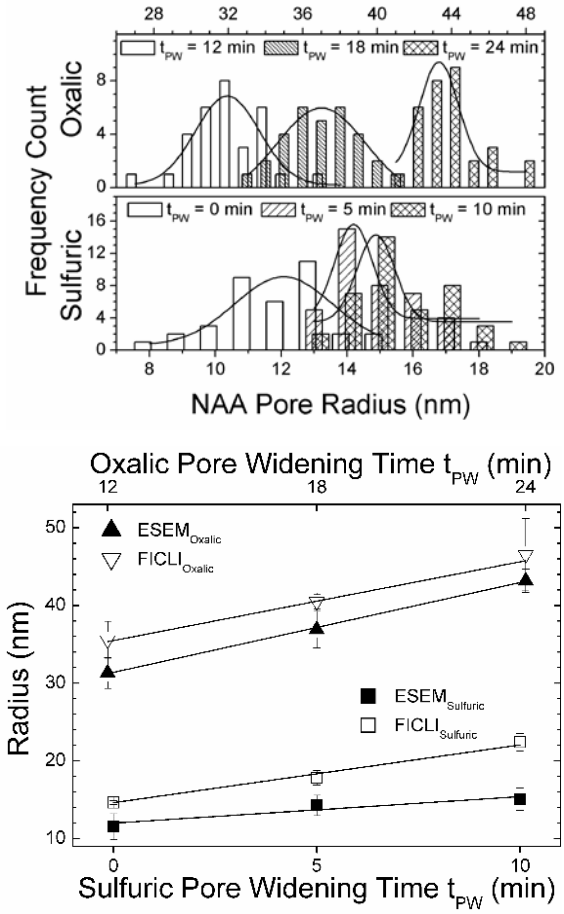

Figure 4.9: (top) Average size distribution of radius estimates obtained by ESEM image analysis for NAA obtained in oxalic and sulfuric acid electrolytes and with the indicated pore widening time. **(bottom)** Average pore radii and standard deviation obtained by FICLI and ESEM image analysis.

The pore radius increase rates (IR) estimated by ESEM image analysis differ by a factor of 3 for NAA_{ox} and NAA_{sul} with $IR_{ox,ESEM}$ = 1.0 ± 0.2 nm/min. and $IR_{sul,ESEM}$ = 0.3 ± 0.2 nm/min. On the other hand, the pore radius increase rate estimations obtained by FICLI were both found identical and accounted to $IR_{ox,FICLI}$ = 0.8 ± 0.2 nm/min. and $IR_{sul,FICLI}$ = 0.8 ± 0.1 nm/min.

The ESEM images show highly ordered pores with a honeycomb-like arrangement and uniform interpore distances for both NAA_{ox} and NAA_{sul}. The image analysis revealed average pore estimates with a wider size distribution of pores compared to FICLI estimations, especially for smaller pore radii. However, the average pore radii and pore radius increase rates obtained by both methods are rather coherent. Minor differences are observed in the radius estimation, which can be attributed to parameter adjustments regarding the liquid-surface interface (contact angle, surface tension, viscosity) during FICLI data treatment. In respect thereof, different contact angles were reported in the literature for pores with increasing radii, which was not accounted for in the data treatment of this study[153]. The large uncertainty stemming from the subjective ESEM image analyses due to arbitrarily selected grey cut off values further added to the presented minor etch rate discrepancies. Nonetheless, the etch rates obtained by ESEM and FICLI are in good agreement with previously published etch rates for NAA produced in oxalic[155] and sulfuric acid[156] electrolytes. In comparison with previous studies, this work provides an estimate of the pore widening rate for a wide range of pore radius and for samples produced with two different electrolytes. These results confirm that uncertainty of pore radius estimation with FICLI is less than 3 nm.

4.2 Characterizing Double and Triple Layer Pore Profiles of NAA Produced in Sulfuric Acid via FICLI Time-Resolved Interferogram Analysis

Thus far the FICLI radius estimations focused on cylindrical pores with straight pore walls. But a large variety of NAA structures can be fabricated not only changing the pore radius and interpore distance but also their internal geometries. Figure 4.10 below illustrates a few possible NAA geometries such cones, funnels, inverted funnels or double and triple layers with changing pore radii.

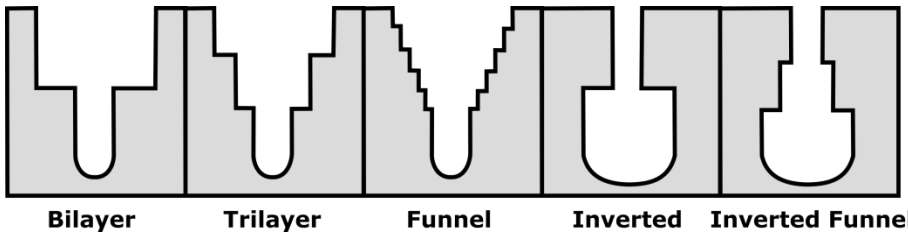

Figure 4.10: Illustration of varying internal pore geometries of NAA

We first used the common two step anodization process to fabricate NAA_{sul} under the conditions described in chapter 3. After the second anodization step the pores were widened for an indicated amount of time (t_{PW}) followed by a third anodization step identical to the second step, resulting in NAA_{sul} with two distinct pore sizes with an upper and lower layer. An ESEM cross section of the NAA_{sul} bilayer in figure 4.11 below shows a clear line separating the two layers, with the upper layer being the widened layer and the lower as-produced layer grown during the 3rd anodization step.

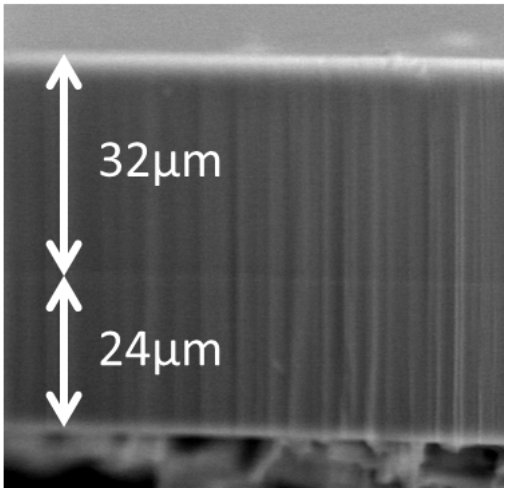

Figure 4.11: ESEM cross section of an NAA_{sul} double layer with a widened upper layer and an as produced lower layer.

Upon moving through the NAA_{sul} the liquid front eventually encounters the transition from top to bottom layer. This transition between two different pore sizes causes a change in the rate at which the liquid front moves past this point. This in turn results in a change in the light interference pattern which in turn expresses itself as a change in the linearity of the time difference between adjacent extrema plotted against the extremum index. Two distinct linear regressions are obtained as illustrated in figure 4.12.

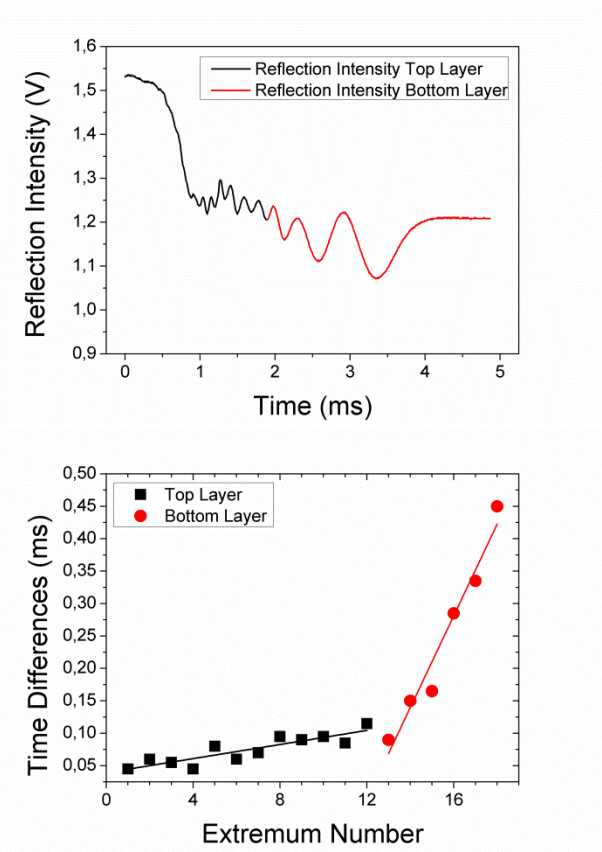

Figure 4.12: (top) light interference reflection intensity over time of an NAA_{sul} double layer, **(bottom)** linear correlation of elapsed time between adjacent extrema versus their indexed extremum number.

The black and red part of the spectrogram and dots belong to the top and bottom layer of the NAA_{sul} respectively. Transforming the two obtained slopes from the light intensity interferograms one obtains two radius estimates per measurement. The obtained pore radius estimates of the upper layer are presented in black and the pore radius estimates of the lower layer are presented in red in figure 4.13 below.

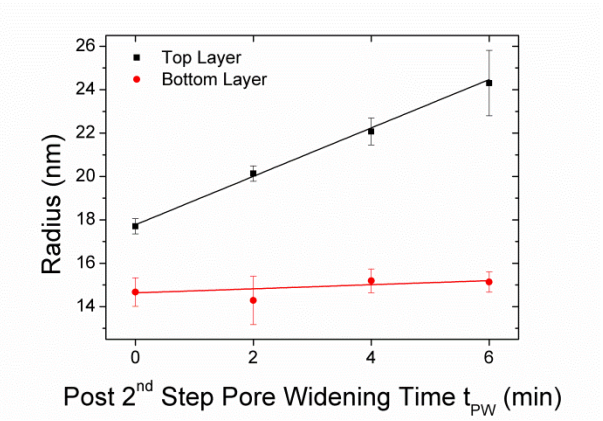

Figure 4.13: FICLI pore radius estimates for top and bottom layers of NAA_{sul} double layers with varying pore widening times after the second anodization step.

The pore widening steps after the second anodization step (post 2nd Step Pore Widening Time t_{PW}) resulted in a similar linear correlation between t_{PW} and estimated pore radius with an etch rate of 1.12 ± 0.15 nm/min (R^2 = 0.99) as compared to the reported for NAA_{sul} and NAA_{ox} monolayers in sections 4.1.1 and 4.1.3 above.

In contrast, the pore radius estimates of the bottom layer remained constant. Expectedly, the 3rd anodization step produced identical pores with similar pore radii for all samples which were not affected by the prior pore etching step.

Similar to the radius estimation and partial internal geometrical characterisation of double layers we fabricated an NAA_{sul} triple layer via a 4 step anodization with intermittent pore widening steps of t_{PW} = 2min. The extraction of time differences between extrema from the

time-resolved interferogram in figure 4.14 shows three zones with distinct linear correlations with varying slopes, with the slopes from left to right representing the top (black), middle (red) and bottom (blue) layer of the triple layer respectively.

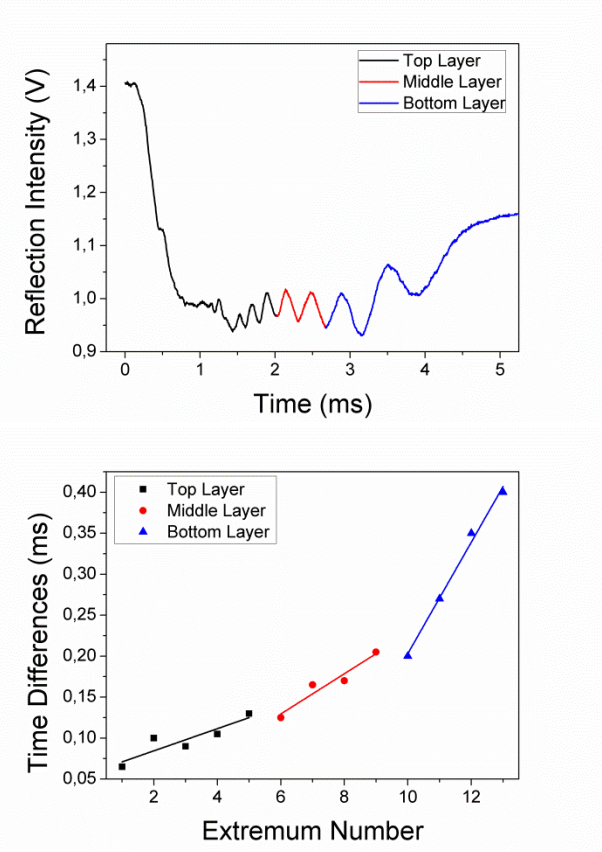

Figure 4.14: (top) light interference reflection intensity over time of an NAA_{sul} triple layer, **(bottom)** linear correlation of elapsed time between adjacent extrema versus their indexed extremum number.

Estimating the pore radius via time-resolved interferogram analysis yields three distinct pore radii for the top, middle and bottom layer of the triple layer (figure 4.15).

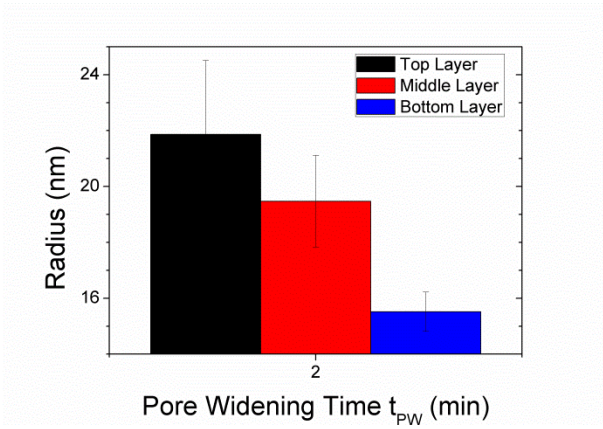

Figure 4.15: FICLI pore radius estimates for top, middle and bottom layers of NAA_{sul} triple layers.

The difference of pore radius of the top layer to the middle layer of 2.39 ± 3.11 nm falls in line with the pore etch rates present in the sections above for a pore widening time of t_{PW} = 2min. However, the difference of 4.00 ± 1.79 nm between the middle layer and bottom layer is somewhat large and does not follow this trend. This might in part be explained by the margin of error during the extraction of the slopes from the spectrograms. The three different zones for the linear regressions are not as clearly separated as seen with the double layers and accurately aligning the slopes becomes slightly arbitrary as the time differences in part appear to flow into one another. This might also stem from the sample as continued etching reduces sharp edges of the transition from one layer to another during the pore etching which may explain the less defined transition from one slope to another. The good linear fit of the distinct local regressions for the top (R^2 = 0.76), middle (R^2 = 0.90) and bottom (R^2 = 0.99) layer obtained from the time-resolved interferogram indicates that the pore radius estimations are good approximations.

Even though to a lesser extent, an influence of the previous pore layer on the movement of the liquid front entering the next layer is to be expected influencing the pore radius estimations. This effect would probably be more evident in longer pore lengths of each layer. However, the pore radius estimates of the triple layer give a good approximation of the respective layers.

We previously demonstrated that FICLI is capable of accurately estimating minor pore radius changes of cylindrical pores in NAA. Here, addressing distinct ranges of the linearity of the evolution of time differences between extrema we further demonstrated that FICLI is capable of detecting and quantifying pore radius changes within an NAA and that FICLI can be used as a topological tool and to characterize the internal geometries of nanopores.

4.3 Summary

In this chapter we addressed the reproducibility and accuracy of fluid imbibition coupled laser interferometry (FICLI) as a pore radius estimation technique under a set of changes to the physico-chemical parameters of the liquid-surface interface. We validated the technique by comparing it to results obtained by environmental scanning electron microscopy (ESEM).

The results showed good reproducibility and accuracy of FICLI when carefully adjusting the physico-chemical parameters of the liquids and carrier matrix in use and we obtained a linear relationship between pore

widening times and increasing pore radius estimates in accordance to the literature for these materials.

However, FICLI and ESEM both present limiting bottlenecks towards the estimation of a pore radius with sub-nanometer accuracy. FICLI pore radius estimations are dependent on the use of accurate physico-chemical parameters of the liquid-surface interface during the analysis of the time-resolved interferograms. Herein lies the challenge, as certain parameters are still under ongoing discussion in the scientific community such as the dynamic contact angle within the nanopores and the changes of fluid parameters (i.e. viscosity, surface tension) due to the nano-confinement. In contrast, insufficient resolution of the ESEM images are the main limiting factor during radius estimations via image analysis as obscure boarders between pore and pore wall with low resolution lead to a highly subjective selection of measurement alignments.

Finally, we demonstrated that, in contrast to the purely topological nature of ESEM, FICLI is capable to characterize NAA beyond the surface and allows getting an insight into the internal geometry by giving pore radius estimates of NAA double and triple layer structures.

UNIVERSITAT ROVIRA I VIRGILI
CAPILLARY FILLING DYNAMICS AS A METROLOGICAL CHARACTERISATION TECHNIQUE FOR THE DETECTION OF RADIUS CHANGES AND SURFACE MODIFICATIONS IN NANOPOROUS ANODIC ALUMINA
Chris Eckstein

Chapter 5

Nanoporous Anodic Alumina Surface Modification by Electrostatic, Covalent and Immune Complexation Binding Investigated by Capillary Filling

Chapter Overview

In the previous chapter various pore widening steps led to an increase in pore radius which was successfully estimated by FILCI. In this chapter we aim to estimate pore radius changes due to the deposition of a variety of chemical and biological materials onto the pore walls. We address the sensitivity, accuracy and reproducibility of FICLI detecting such pore radius reductions and evaluate its potential as a biosensor based on pore radius reduction.

We first electrostatically bind the widely used model protein and blocking agent bovine serum albumin (BSA)[157] onto the pore walls as a proof of concept for the detection of a radius reduction upon immobilizing biomolecules. Thereafter, layer-by-layer deposition of polyelectrolytes onto the walls is monitored in consecutive deposition and radius estimation steps to show that FICLI is capable of detecting the build-up of multi-layered systems. This in turn allows interpreting the radius reduction obtained by the functionalization with (3-aminopropyl)triethoxysilane (APTES) used as chelating agent for a following covalent immobilization of Streptavidin. A final experiment addresses FICLI estimations of pore radius reduction upon a series of immune complexation binding events between Protein A (PA) and immunoglobulins (IgG).

5.1 Optical Characterization of Electrostatic Immobilization of BSA in NAA

BSA is a standard protein in molecular biology and is often used to block unconjugated surfaces during immuno assays to avoid non-specific binding of target analytes. It is well characterized and like most proteins BSA folds into globular domains with a minimal surface area due to hydrophobic effects. It is approximately 65kDa with the dimensions of about 2.5 x 5 x 6 nm. At pH 7 it possesses sufficient positively charged moieties for electrostatic immobilization on negatively charged NAA surfaces[158].

Initially hydroxylating NAA in 35% H_2O_2 at 70°C for 30min increases the number of negative binding sites on the NAA pore walls for an enhanced electrostatic binding and a homogenous distribution of BSA during the following protein incubation. BSA suspensions were prepared in DI water rather than commonly done in PBS to avoid protein charge neutralization via ions in the buffer. [158]

As demonstrated in chapter 4 FICLI is capable of characterising the internal pore geometries of NAA. Here we use BSA to assess if it is also possible to characterize electrostatic protein immobilization and whether FICLI is able to detect the protein within the NAA.

5.1.1 Optical Characterization of NAA Radius Changes and BSA Immobilization – Photoluminescence Spectroscopy, Fourier Transform Infrared Spectroscopy, Confocal Microscopy

Photoluminescence Spectroscopy

Photoluminescence is among the most suitable techniques for protein characterization in enzymology due to its accuracy and reproducibility[159][160].

Nanoporous anodic alumina shows photoluminescence upon excitation and distinct oscillation patterns of photoluminescence intensity are obtained depending on the morphology of the nanoporous structure[112], [123] . For instance the interpore distance, pore radius and NAA thickness play a role in the formation of these oscillations which arise due to a Fabry-Perot effect, as exemplified in figure 5.1.

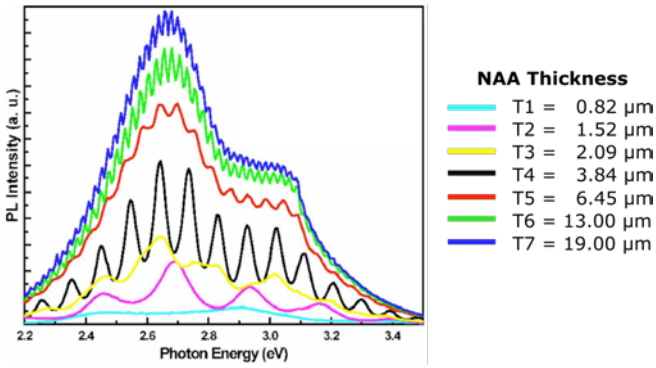

Figure 5.1: Formation of an oscillation pattern of photoluminescence intensity in NAA with increasing thickness. Adapted from Huang et al. 2006[112].

The position of the intensity extrema can be related to the effective optical thickness (EOT) infiltrated with different substances. The changing effective optical thickness (ΔEOT) was previously demonstrated to be exploitable as an optical sensing system [127], where a ΔEOT was found upon the surface functionalization and covalent immobilization of trypsin. However, the presence of photoluminescence intensity oscillations depends on the thickness and anodization electrolyte the NAA is fabricated with and with increasing thickness the oscillation pattern vanishes.[112]

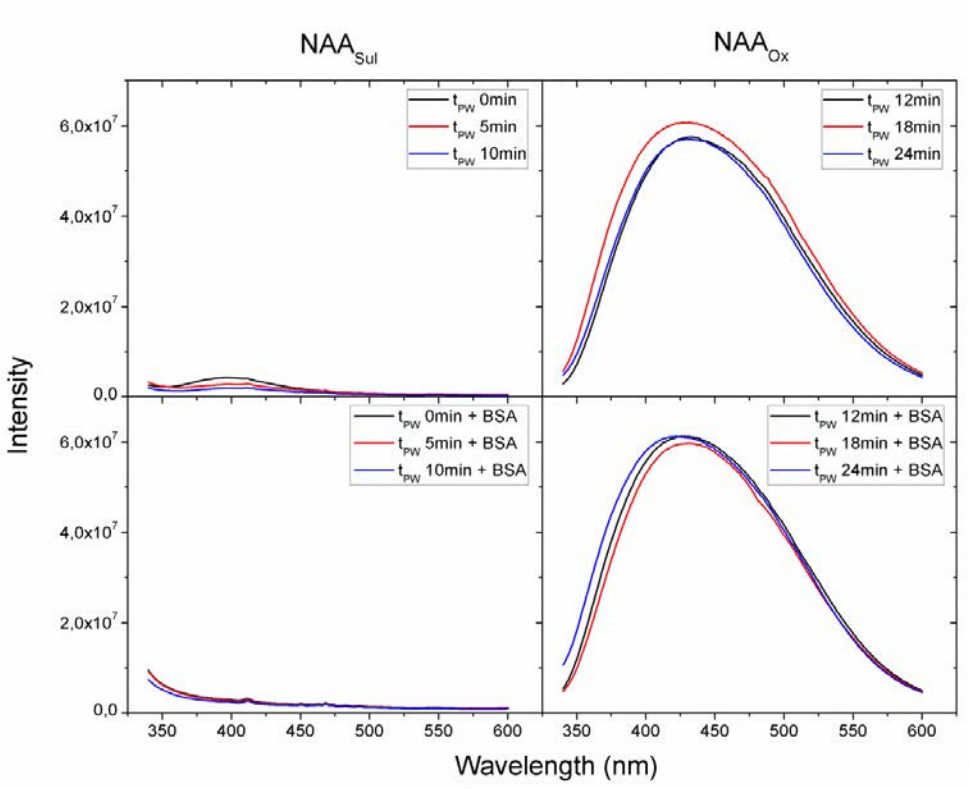

Figure 5.2: Photoluminescence intensities of NAA_{Ox} and NAA_{Sul} after a series of widening steps before and after electrostatically binding BSA.

Figure 5.2 shows photoluminescence intensities of NAA fabricated with sulfuric acid (NAA_{Sul}) and oxalic acid (NAA_{Ox}) electrolyte, a total thickness of 75µm, varying pore widen times (t_{PW}) and after the electrostatic immobilization of BSA.

Photoluminescence of NAA_{Sul} and NAA_{Ox} upon UV irradiation is well documented and was shown to depend on the NAA thickness, with NAA_{Ox} exhibiting stronger photoluminescence intensities than NAA_{Sul}. This is confirmed by the difference in photoluminescence intensities between the two types of NAA shown in figure 5.2. However, there was no detectable effect of the pore radius change as can be seen from the increasing pore widening times t_{PW} with constant photoluminescence intensities. The immobilization of BSA did not result in a noticeable effect on the photoluminescence intensities either. The lack of Fabry-Pérot oscillations and the lack of changes in photoluminescence due to morphological changes of the NAA and BSA immobilization can be explained by the large sample thickness leading to a signal over-exposure and a loss of sensitivity. Only minor changes in EOT of less than 2% upon surface modifications, as shown in other studies[127], are probably masked by the very high photoluminescence intensities due the very large sample thickness in this case which renders this alternative path to co-validate of detecting the annealing of BSA unsuccessful.

Fourier Transform Infrared Spectroscopy

Another rather traditional technique to characterize the surface chemistry of NAA is Fourier Transform Infrared Spectroscopy. In brief, this technique allows measuring the absorption of infrared light by

chemical bonds. Chemical bonds absorb distinct amounts of energy and a fingerprint like pattern expressed in wavenumbers is used to identify chemical compositions.

FTIR spectra of three NAA_{Sul} and NAA_{Ox} with different pore widening times t_{PW} before and after the electrostatic immobilization of BSA are show in figure 5.3.

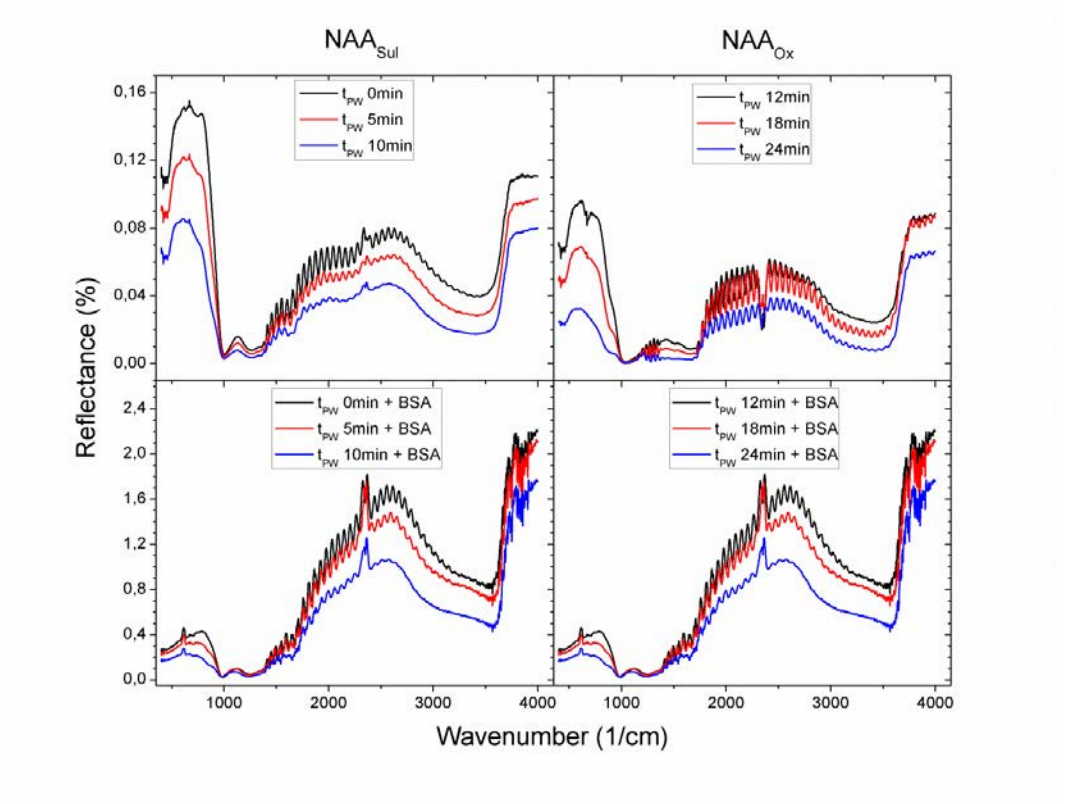

Figure 5.3: FTIR of NAA_{Ox} and NAA_{Sul} after three widening steps before (top) and after (bottom) electrostatically immobilizing BSA.

In figure 5.3 top, the FTIR spectra of NAA_{Sul} and NAA_{Ox} are similar with regard to their reflectance bands and intensities. Reflectance intensities

decrease for both NAA_{Sul} and NAA_{Ox} with increasing t_{PW} due to the decrease in reflecting surface area over pore widening time.

In figure 5.3 bottom, electrostatic immobilization of BSA increases the overall reflectance intensities but no distinct bands indicating the presence of the protein are observed. Reflectance intensities also decrease for both NAA_{Sul} and NAA_{Ox} with BSA with increasing t_{PW}. Decreasing reflectance intensities over increasing pore widening time t_{PW} for NAA_{Sul} and NAA_{Ox} with and without BSA can be explained by the decrease in reflecting surface area over pore widening time. Not detecting distinct reflectance band for BSA is somewhat surprising since it was shown to produce distinct FTIR reflectance bands at 1600 cm^{-1}.[161] However, the increasing reflectance intensities after BSA immobilization may be related to the increasing water content within the molecule.

Even though a higher reflectance in the FTIR patterns was observed upon the immobilization of BSA it was, however, not possible to detect expected distinct bands to chemically identifying the protein. Furthermore, FTIR is not able to discern between topologically immobilized protein and protein attached to the inside walls of the NAA pores.

Confocal Microscopy

Photoluminescence spectroscopy and FTIR are topological methods that are mainly dependent on the surface characteristics of NAA. With the previous results it is therefore not possible to reliably tell whether BSA

immobilizes on the pore walls within the NAA pores or simply on the top surface. Confocal microscopy allows reconstructing three dimensional images of a sample by means of optical sectioning, i.e. taking several two dimensional images at different depths in the sample.

Thus, confocal microscopy permits to vertically scan the NAA. However, the resolution of the confocal microscope is not sufficient to detect single proteins within the pores. But coupling it with a fluorescence excitation and detection system allows detecting fluorescence labels. Here we used a fluorescence labelled BSA which resulted in images with easily distinguishable fluorescence carpets in each depth where the protein was present.

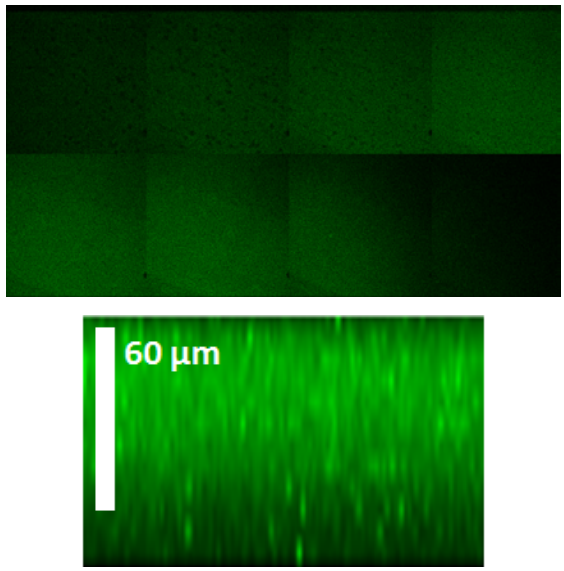

Figure 5.4: (top) top view confocal microscopy images at 7.5µm depth intervals from top left to bottom right, **(bottom)** superimposition of top view images and resulting cross sectional view of NAA produced in oxalic acid after immobilization of labeled BSA.

Figure 5.4 (bottom) shows a vertically reconstructed image after superimposing 12 images at depths with 7.5 µm distances in between (top). A bright fluorescence is visible throughout the NAA sample marking a total distance of 60µm with darker margins at the top and bottom. The fluorescing area corresponds to the NAA thickness whereas the dark areas correspond to images taken outside the matrix of the NAA. Even though the image provides sufficient qualitative proof for the immobilization of BSA within the pores we henceforth try to present data of a more quantitative nature on the size of the immobilized proteins using FICLI in the following sections.

5.1.2 FICLI Estimations of Radius Reduction due to BSA Immobilization

In order to demonstrate the ability of FICLI to sense biological binding events on the inner pore surface of NAA produced in oxalic acid (NAA_{ox}), the pore radius was estimated before and after the immobilization of BSA inside the pores. An NAA_{Ox} was first hydroxylated as described above to provide sufficient hydroxyl groups. Subsequently the NAA_{Ox} was incubated with 100 µg/mL BSA in DI water at 4 °C overnight.

As shown in Chapter 4 FICLI is capable of giving indications about the consistency of the internal pore geometry. Here, after BSA immobilization we obtain a similar pattern of the fluid movement compared to the as-produced NAA_{Ox} before the BSA immobilization.

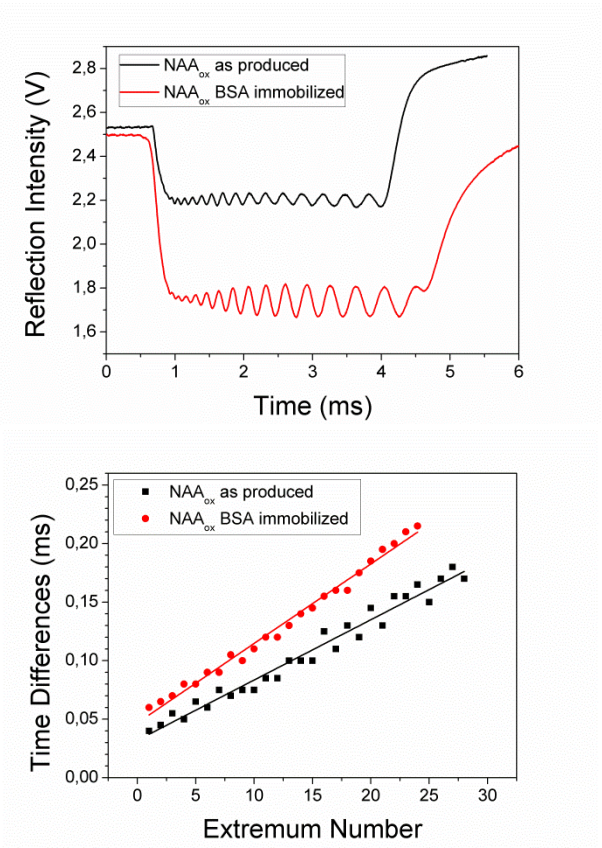

Figure 5.5 (top) Time-resolved interferogram of an NAA produced in oxalic acid. **(bottom)** Time differences between adjacent extrema vs number of extrema used for the estimation of the pore radius before and after electrostatic immobilization of BSA.

Figure 5.5 illustrates the movement of the fluid. The differences in the linear regressions are due to a different radius of the pore before and after BSA immobilization, however, the mostly linear progression of both scatters (NAA_{ox} as-produced $R^2 = 0.97$, NAA_{ox} with immobilized BSA $R^2 = 0.99$) indicates similar internal pore geometry. Hence we can safely

assume the BSA is homogenously distributed along the pore walls inside the NAA, backing up the confocal microscopy images.

The conversion to radius showed an estimated radius reduction (ΔR) from 35.6 ± 0.8 nm to 30.7 nm ± 0.4 nm which led to an estimate of BSA diameter of d_{BSA} = 4.9 nm ± 1.1 nm. The dimensions of BSA were previously reported to 2.7 x 6.3 x 8.2 nm [162] and the estimated pore radius reduction upon BSA immobilization found in this study are in good agreement.

In order to more comprehensively evaluate the influence of electrostatic immobilization of biomolecules to the NAA pores on the accuracy of FICLI, we studied the electrostatic immobilization of BSA in NAA produced in sulfuric (NAA_{sul}) and oxalic (NAA_{ox}) acid for a range of pore radii. Figure 5.6 top shows six pairs of FICLI radius estimates corresponding to NAA before (back bars) and after (front bars) the electrostatic immobilization of BSA. Bars with horizontal or vertical patterns correspond to NAA_{sul} or NAA_{ox}, respectively. The x-axis corresponds to the pore radius FICLI estimate of the as-produced sample after pore widenings of t_{PW} = 0, 5 and 10 min for NAA_{sul} and t_{PW} = 12, 18 and 24 min for NAA_{ox}, and before the BSA immobilization. In Figure 5.6 bottom the estimated radius reductions after BSA immobilization are shown. This radius reduction estimate can be related to the BSA molecule diameter. The estimated reductions (ΔR) for NAA_{sul} are slightly larger than those for NAA_{ox} with $\Delta R_{,sul}$ = 8.0 ± 0.8 nm and $\Delta R_{,ox,\ ox}$ = 6.9 ± 1.9 nm, respectively.

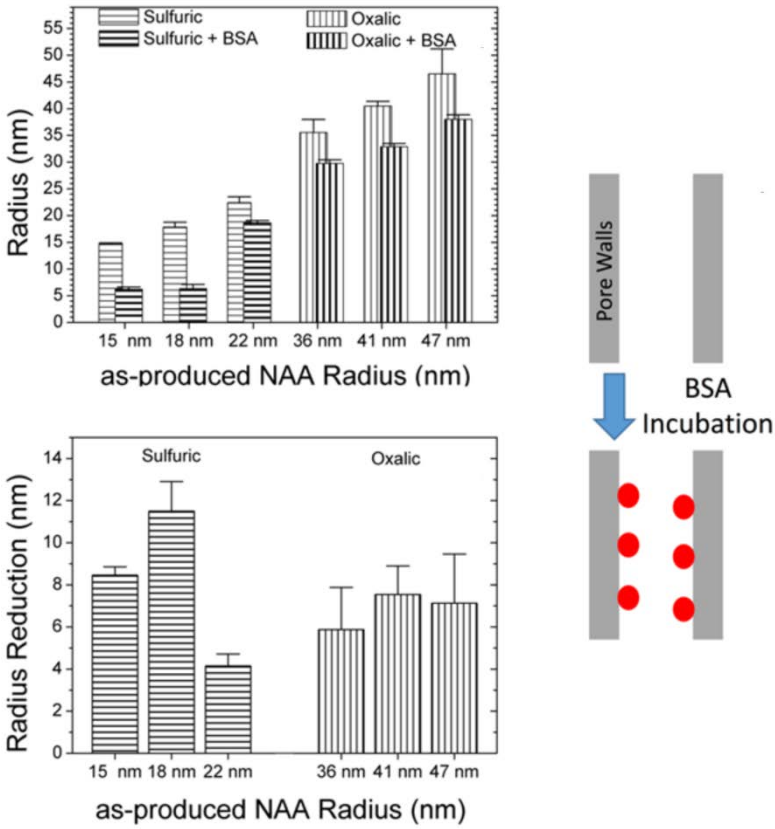

Figure 5.6: (top) Average pore radius estimated by FICLI for samples produced in sulfuric acid electrolyte and oxalic acid electrolyte with different pore widening times (characterized in figures 4.8 and 4.9) before and after electrostatically immobilizing bovine serum albumin (BSA) to the pore walls. **(bottom)** Radius reduction estimated by FICLI for the same sets of samples. **(right)** Schematic illustration of the surface modification monitored in this experiment.

The detection of BSA was very reproducible with a marginal standard deviation of 3.2 nm across a large range of as-produced radii (15 – 43 nm) and two types of NAA materials (i.e. NAA_{sul}, NAA_{ox}). The radius reduction due the immobilization of BSA depends neither on the initial

as-produced pore radius of NAA_{sul} and Past studies providing the dimensions of BSA (2.7 x 6.3 x 8.2 nm)[162] show that the radius reduction due to the immobilization of BSA in NAA_{sul} and NAA_{ox} in the present study both fall into a slightly overestimated size range of the protein.

These minor overestimations can in part be explained by the wetting properties of the BSA molecule which retains an additional water layer in aqueous solution (Debye sphere) due to its electrostatic potential. The formation of more than one layer and disordered alignment on the surface are also possible explanations for these BSA size over-estimations. However, more important is the selection of the liquid-surface interface parameters (i.e. contact angle) used during the data treatment for the radius estimation. It was previously shown that the contact angle depends on the electrolyte the NAA is fabricated with. It further depends on the changes upon wet chemical etching of NAA, probably due to a changing surface composition with fewer impurities towards the center[113], [163]. These etching-related changes were not accounted for in this study and the accuracy of the absolute values of the contact angles may be in question, explaining the differences in radius reduction due to BSA immobilization in NAA_{sul} and NAA_{ox}. The selection of precise parameters for the FICLI interferogram analysis plays therefore a crucial role in the accurate estimation of NAA radii. Nonetheless, both estimations of the size of BSA fall into realistic dimensions and present reasonable estimates.

5.2 Radius Reduction Estimations of Multi-Layer Systems via Layer-by-Layer Deposition of Polyelectrolytes

In order to evaluate the sensitivity of FICLI towards the step wise reduction of the pore radius via a multi-layer system, polyelectrolyte double layers were deposited inside the pores with intermittent pore radius estimations.

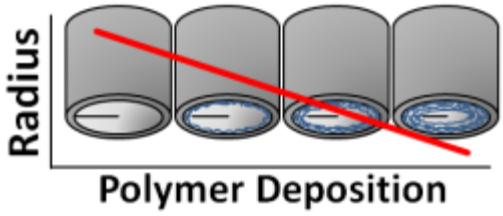

Figure 5.7: Graphic illustration of polymer deposition leading to pore radius reduction

An NAA_{SuI}, fabricated as described in Chapter 3, was initially widened for t_{PW} = 6min and the pores were further modified with polyelectrolyte double layers as follows: The pores were hydroxylated in > 30% hydrogen peroxide (H_2O_2) at 70 °C for 30 min and thereafter handled in nitrogen environment. The NAA_{SuI} was placed in 20 mL anhydrous toluene and 0.2 mL of (3-aminopropyl)triethoxysilane (APTES) was added drop wise and stirred for one hour. 10 min washing steps in anhydrous toluene in nitrogen environment and in toluene and deionized water at ambient environment followed. Incubation overnight at 120 °C facilitated silane crosslinking. Polymer deposition was performed by dipping the NAA_{SuI}, in poly(allylamine hydrochloride) (PAH) and poly(sodium 4-styrenesulfonate) (PSS) solutions (0.5 mg/mL

in 0.15 M NaCl) for 30 min, for a number of polyelectrolyte double layers given as N_{PDL}, following a protocol reported elsewhere [146].

Figure 5.8 shows FICLI pore radius estimates (r) as a function of the number of double layers of PAH/PSS polyelectrolytes (N_{DPL}) deposited inside the pores.

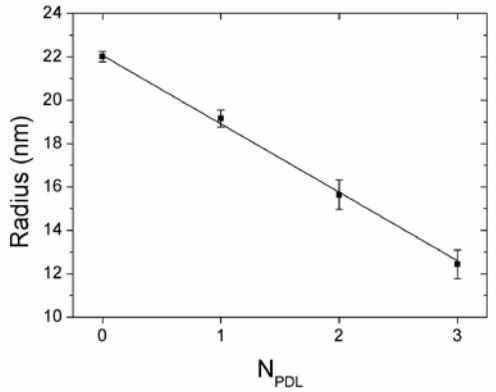

Figure 5.8: Estimated pore radius obtained by FICLI using 0.15M NaCl as a function of the number of PAH/PSS double layers N_{PDL}.

The radius reduction rate during the LbL deposition of PAH/PSS was found to be constant at $r_{PAH/PSS}$ = 3.2 nm ± 0.2 nm per N_{PDL}, as illustrated by the trend line in figure 5.8. The thickness of every added double layer is slightly larger than the thickness reported in other works[20], where elipsometry was used to obtain an estimated PAH/PSS double layer thickness on flat surfaces of about 2 nm. The slightly larger thickness presented in this study might be explained by spatial restrictions during the LbL deposition, where the geometry of the nanochannels is confined as opposed to a flat surface.

The error bars in figure 5.8, which correspond to the standard deviation for the replicates on the same sample, are smaller than the radius difference between two consecutive double layers. This demonstrates that FICLI is able to resolve each deposited double layer. The consistency of radius estimations when using different liquids (chapter 4.1.2) and when changing from non-modified to PAH/PSS coated NAA illustrates the robustness of the method towards estimating NAA pore radii across different liquid-surface interfaces.

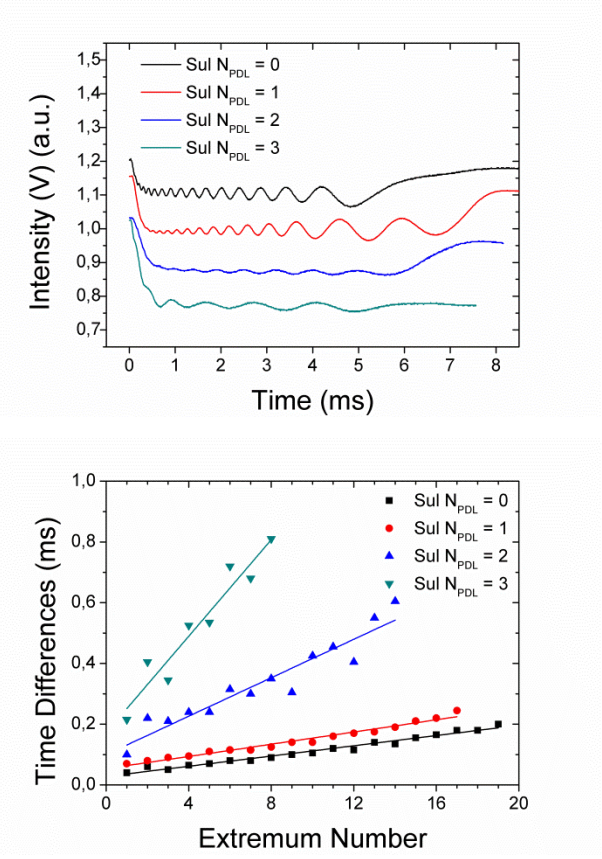

Figure 5.9: (top) and **(bottom):** data corresponding to one measurement among all replicates for the different polyelectrolyte double layer deposition steps.

Figure 5.9 top and bottom show the time-resolved interferograms and the corresponding data analysis to confirm the absence of artefacts in the experiments and that the pores remained open after the deposition of the 3rd polyelectrolyte double layer.

In conclusion it was not only possible to detect and estimate the thickness of a deposited polyelectrolyte double layer but it was furthermore possible to differentiate between intermittent deposition steps and reproduce consistent size changes corresponding to the deposited double layers.

5.3 Estimating the Thickness of the Time Dependent Deposition of a Silane Functionalization via FICLI

As presented in the section above it was possible to demonstrate that FICLI is capable of detecting and estimating the stepwise deposition of a polymer to the pore walls, thereby reducing the pore radius. In continuation of this experiment we present a practical application to demonstrate and estimate the time-dependent multi-layer formation of the commonly used silane functionalization (3-aminopropyl)triethoxysilane (APTES).

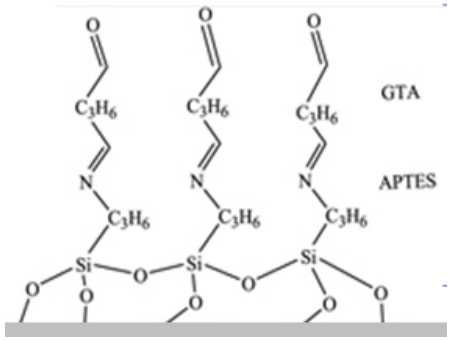

Figure 5.10: Scheme of APTES+GTA with a theoretical thickness of less than 2nm, according to the sum of the individual bond lengths.

APTES is a coupling agent and is frequently used to covalently immobilize organic molecules to hydroxylated surfaces, such as NAA. Ideally, under perfectly controlled reaction conditions an APTES monolayer of only 1-2nm is formed during the chemical deposition. However, forming silanol groups in the presence of water may react with each other resulting in polymerization. APTES molecules have also been shown to physio-sorb to each other forming vertical multi-layers. Reaction temperature, water content, APTES concentration and reaction time have been shown to influence such a multi-layer formation. [164]

Depending on the scientific scope of an experiment such multi-layer formation may be undesirable. In this section we aim to detect and estimate the dependence of multi-layer formation of APTES within NAA pores on the chemical deposition-time during the functionalization process.

NAA samples were fabricated following the well-established two-step anodization method as described in chapter 3, with an 0.3M oxalic acid

electrolyte at an anodization potential of 55V at 5°C. The anodization time at the second step was adjusted to obtain 80 µm length pores, with an average interpore distance of 138 nm and a pore radius estimated from SEM pictures (figure 5.11 top and bottomt) of 30 nm.

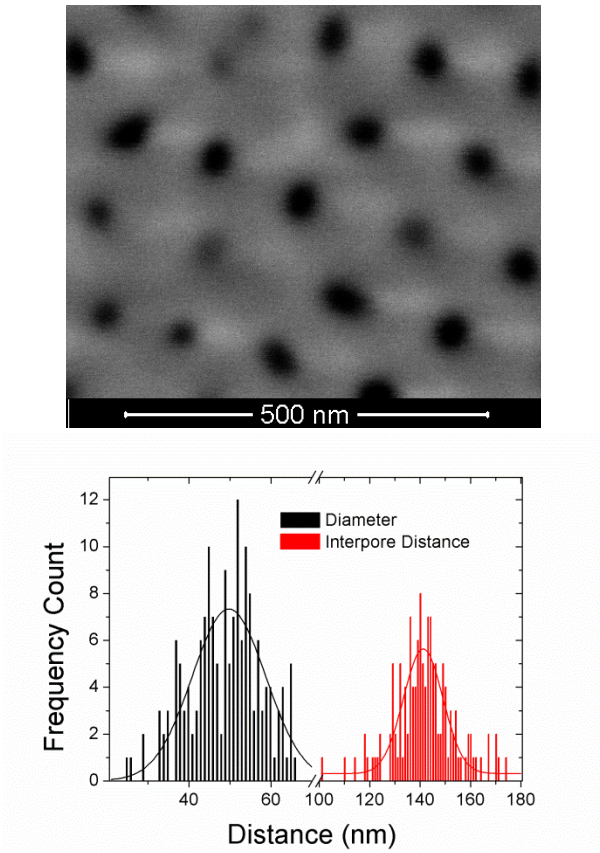

Figure 5.11: (top) ESEM images of NAA fabricated in oxalic acid electrolyte with **(bottom)** pore radius estimations via ESEM image analysis.

The remaining aluminum was etched away and the pores were opened at the bottom end by reactive ion etching to obtain a membrane. NAA samples were then modified following different steps: first, they were hydroxylated in hydrogen peroxide at 70 ºC for 0.5 h. Then, four groups of samples were formed and each group was incubated in a 2% (v/v) APTES solution for different amounts of time (0.5, 1, 2 and 4 hours) at room temperature.

All the samples were measured with FICLI, using MQ water as the infiltrating liquid. Triplicate measurements at three different sample spots were conducted and an estimate of the pore radius was obtained using the adequate values of liquid viscosity and surface tension and of the liquid-surface contact angle

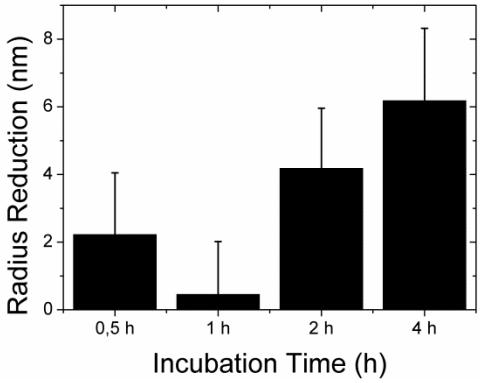

Figure 5.11: FICLI pore radius reduction estimates for different APTES incubation times.

Figure 5.11 illustrates increasing radius reductions after each APTES incubation step with increasing incubation time. This is a clear indication of the multi-layer deposition of APTES, in agreement with the

literature [164], [165]. We have demonstrated the multi-layer attachment of the APTES silane linker to the inner pore walls of nanoporous anodic alumina by FICLI. This multi-layer attachment is directly correlated to the incubation time of the APTES molecule. This finding obtained by FICLI is of special interest for future applications of APTES-functionalized NAA.

5.4 Covalent immobilization of Streptavidin

Since in some cases it is not possible to immobilize biomolecules to surfaces electrostatically, covalent attachment via silane coupling has become common practice. In this study FICLI served to detect and characterize the silane coupling agent APTES+GTA and the covalent immobilization of streptavidin in NAA produced in oxalic acid (NAA_{ox}) widened by t_{PW} = 18 min.

Figure 5.12 a shows the consecutive radius estimations of NAA_{ox} after the following modification steps: i) pore widening for t_{PW} = 18 min, ii) silanization with APTES-GTA and iii) covalent immobilization of streptavidin. On the other hand, figure 5.12 b shows the normalized slopes, S, obtained from the raw oscillation patterns used for the radius estimation for the same modification steps, in a logarithmic scale.

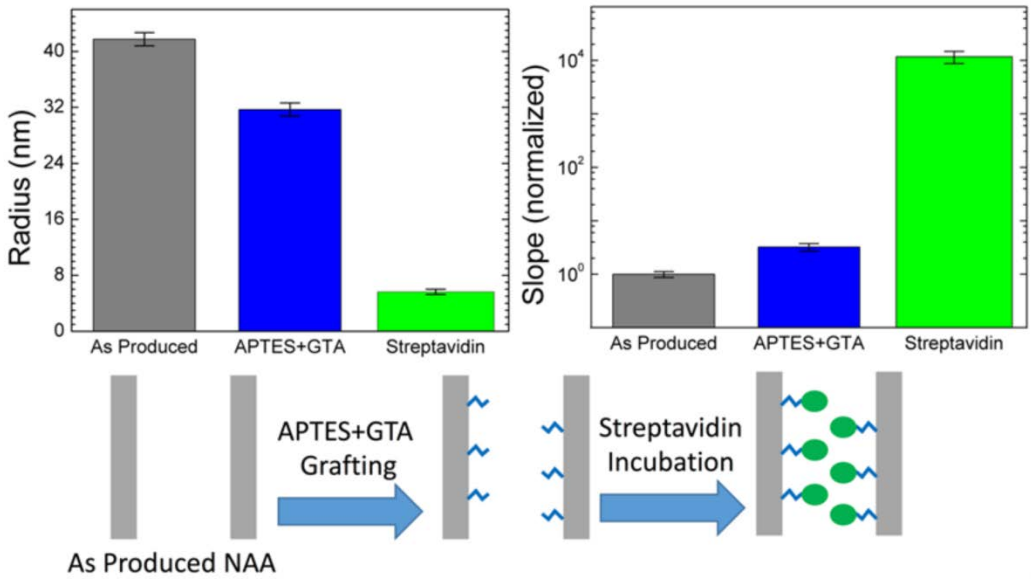

Figure 5.12: (top, left) FICLI radius estimations of an NAA produced in oxalic acid electrolyte with an initial pore widening step (t_{PW} = 18 min), a subsequent functionalization step with APTES+GTA and a final covalent immobilization step of streptavidin. **(top, right)** corresponding FICLI slopes. **(bottom)** Schematic drawing of the surface modifications monitored in this experiment.

The radius estimates account for $R_{18\ min}$ = 41.8 ± 1.0 nm, $R_{APTES\text{-}GTA}$ = 31.7 ± 1.0 nm and $R_{streptavidin}$ = 5.6 ± 1.0 nm. The respective radius reductions amount to $\Delta R_{APTES\text{-}GTA}$ = 10.1 ± 1.0 nm and $\Delta R_{streptavidin}$ = 26.0 ± 0.4 nm which both represent an over-estimation of a monolayer of the silane coupling agent and the protein respectively. Concerning the slope S, it can be seen that it increases significantly (3 fold) upon the functionalization with APTES+GTA and then it increases sharply (3612 fold) after the covalent immobilization of streptavidin.

The 10 nm radius reduction observed after APTES-GTA immobilization is not in agreement with the size of the molecules: considering an APTES monolayer as the sum of the individual bond lengths one obtains a theoretical thickness of less than 1nm as discussed in chapter 5.3. However, multilayer deposition of APTES is common and is strongly dependent on the reaction conditions.[164], [165] Vandenberg et al. addressed some of the reaction conditions and obtained layers with thickness from 1.8 and up to 33 nm with incubation periods of from 1 and up to 24 h and an APTES concentration of 0.4 %. Therefore, the observed slope and radius reduction are reasonably justified by the experimental conditions, concisely 2 h. incubation period with an APTES concentration of 1 % and an additional GTA layer.

The sharp increase in slope S (up to four orders of magnitude) after the streptavidin immobilization is a consequence of the dependence of the slope with the inverse fifth power of the radius: as the pores become smaller, the slope S approaches infinity. This means that such a magnitude is especially sensitive for small radius values.

In the case of Figure 5.12 above, the results demonstrate that after streptavidin immobilization the pores are nearly blocked. The homogenous deposition of streptavidin across the NAA thickness was confirmed by the linear dependence of the fluid imbibition dynamics, figure 5.13 (top) and by the confocal microscopy image shown in figure 5.13 (bottom).

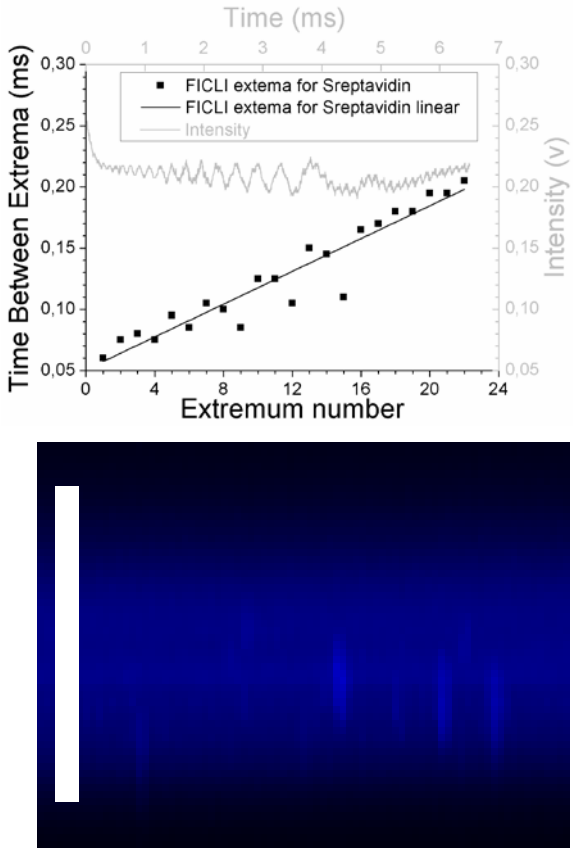

Figure 5.13: (top) Fluorescence confocal microscopy image of the NAA cross-section visualizing the immobilized streptavidin via its fluorescence marker throughout the NAA thickness**. (bottom)** Fluorescence confocal microscopy image of the NAA cross-section visualizing the immobilized streptavidin via its fluorescence marker throughout the NAA thickness of 85µm (white scale bar).

The radius reduction upon streptavidin immobilization is about 2.5-fold larger than the expected maximal dimension of the protein (2.0 x 6.8 x 10 nm) [96]. Similarly to the discussion about the size overestimation of BSA in section 5.1.2 the formation of a protein multilayer within the

NAA is the most probable cause of the Streptavidin overestimation. Nevertheless, we hereby successfully demonstrated FICLI's capability to detect the covalent immobilization of a protein via silane coupling.

5.5 Immobilization via immune complexation

In the previous sections we addressed FICLI's capability and accuracy in detecting and characterizing protein immobilized within NAA via different immobilization strategies. In the following section we look at another immobilization strategy of proteins crucial for the functionality of immuno-sensors where specific proteins are immobilized via immune complexation reactions occurring between proteins.

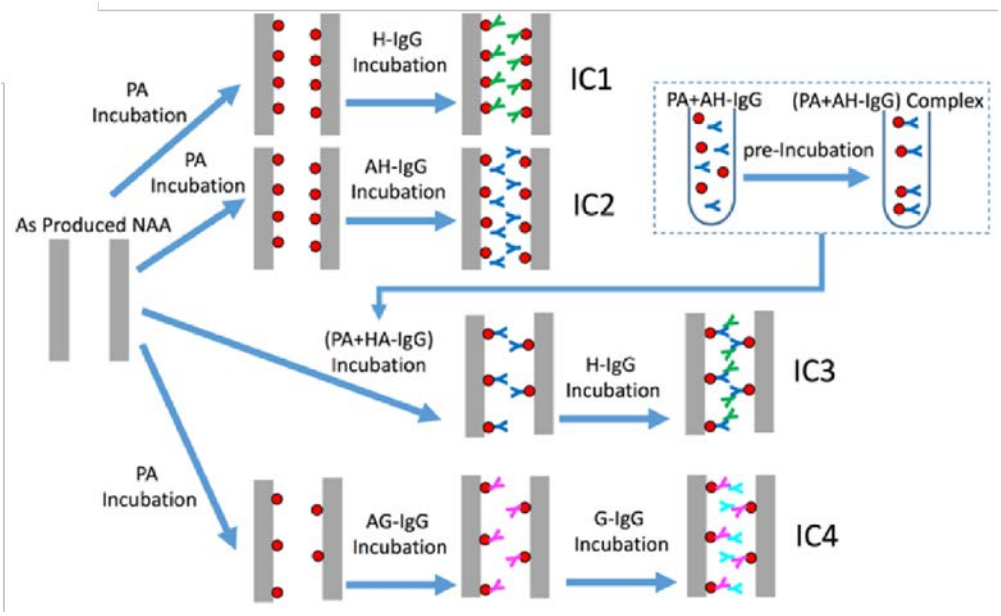

Figure 5.14: Schematic drawing of the different surface modification steps monitored in experiments IC1 to IC4.

Immune complexation reactions of protein A and immunoglobulins (IgG) were conducted at the NAA pore surfaces and its influence on FICLI radius estimations was evaluated. The following experiments were conducted as illustrated in figure 5.14 which schematically depicts four immune complexation experiments with the labels IC1 to IC4.

The NAA used for the following experiments were fabricated in oxalic acid at 55 V at 5 °C for an anodization period to reach a total NAA thickness of 75 µm. Immobilization of immunoglobulins (IgG) via immune complexation in the IC experiments was accomplished by initially hydroxylating 4 NAA_{ox} in > 30% hydrogen peroxide (H_2O_2) at 70 °C for 30 min.

In experiment IC1, the hydroxylation was followed by the electrostatic immobilization of 100µL of 100 µg/mL protein A (PA) at 4°C overnight. Subsequently 100µL of 1 mg/mL of human-IgG (H-IgG) from human serum were incubated at 4°C overnight to form immune complexes with PA via the human Fc portion of the H-IgG.

Similarly, in experiment IC2, the hydroxylation was followed by electrostatic immobilization of 100µL of 100 µg/mL PA at 4°C overnight with a final incubation of 100µL of 1 mg/mL of anti-human-IgG (AH-IgG) produced in goat, to form immune complexes with PA via the goat Fc portion of the AH-IgG.

In experiment IC3, the immune complexation between 100µg/mL PA and 1mg/mL AH-IgG was allowed to take place in a test tube at 4° C

overnight, to provide an increased reaction volume for the complexation reaction. After this test tube pre-incubation period, the NAA_{ox} was incubated with 100µL of this PA/AH-IgG complex at 4°C overnight. Finally 100µL of 1mg/ml of H-IgG was incubated at 4° C overnight, to form secondary immune complexes between the two IgG.

Finally, in experiment IC4, hydroxylation of NAA_{ox} and the electrostatic immobilization of PA (100µL of 100µg/mL at 4° C overnight) were followed by the incubation of 100µL of 1mg/mL of anti-Goat IgG (AG-IgG, produced in rabbit) to form PA-IgG immune complexes via the rabbit Fc portion of the AG-IgG. A final incubation of 100µL of 1mg/mL of goat IgG from goat serum was applied to form secondary immune complexes between the two AG-IgG and G-IgG. All NAA_{ox} were rinsed with DI water and characterized with FICLI after each incubation step.

Each experiment consists of consecutive protein immobilization events, as indicated by the categorical x-axis in figure 5.15. Their respective FICLI radius estimations after each step are shown in figure 5.15 (top), while the slopes S from each FICLI measurement are presented in figure 5.15 (bottom). The slope values were normalized by the value corresponding to the as-produced NAA in each IC experiment taking as unity.

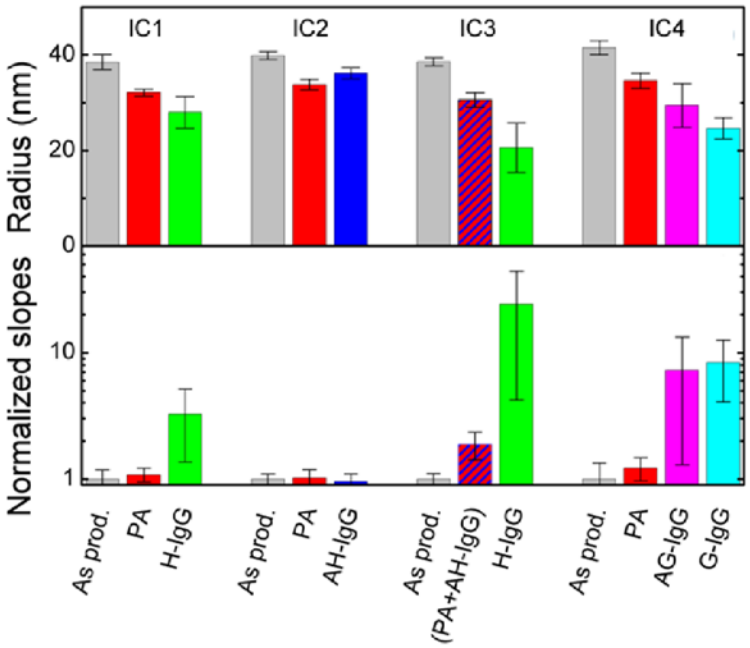

Figure 5.15: (top) Consecutive FICLI radius estimation and **(bottom)** slopes obtained for NAA as-produced in oxalic acid before and after electrostatic protein A immobilization and successive immune complexation steps with antibodies and antigens.

In IC1 the two incubation steps of protein A (PA) and human-IgG (H-IgG) result in two clear slope increases and respective radius reductions. The slope increase after the incubation of human-IgG is much more significant as compared to protein A. In contrast, the corresponding radius reductions are similar for both steps, with values $\Delta R_{IC1,PA} = 6.4 \pm 0.7$ nm and $\Delta R_{IC1,H\text{-}IgG} = 5.5 \pm 2.3$ nm. This is in agreement with the fact that human-IgG complexes with PA with high affinity.

In IC2 the incubation of protein A with the NAA_{ox} resulted in a similar slope increase and radius reduction as in IC1, with $\Delta R_{IC2,PA} = 6.1 \pm 1.1$

nm, confirming the reproducibility of this first step. However, the slope variation upon anti-human-IgG (AH-IgG) incubation is small, with a consequent small variation in the corresponding radius. This is not a surprising result, as it is widely known that this AH-IgG, obtained from goat serum, has a low affinity to PA.

For this reason, in experiment IC3 protein A and AH-IgG were pre-incubated in PBS in a reaction tube overnight prior to incubation on NAA_{ox}. After this incubation, a clear slope and radius reduction of this immune complex with $\Delta R_{IC3,PA+AH\text{-}IgG} = 8.0 \pm 1.5$ nm is obtained. The slope variation and radius reduction are similar to the corresponding values seen for the combined PA and H-IgG in IC1. The comparison between the results of the IC2 and IC3 experiment indicates that the immune complexation dynamics are critically impaired by the limited reaction space provided by the NAA. In IC3, the subsequent incubation of H-IgG resulted in a further slope S variation and a corresponding radius reduction of $\Delta R_{IC3,H\text{-}IgG} = 10.0 \pm 1.3$ nm. Finally, in IC4 three distinct slope increases after the incubation with PA, goat-IgG (G-IgG) and anti-goat-IgG (AG-IgG) can be observed and the respective radius reductions amount to $\Delta R_{IC4,PA} = 6.9 \pm 1.6$ nm, $\Delta R_{IC4,AG\text{-}IgG} = 6.6 \pm 2.9$ nm and $\Delta R_{IC4,G\text{-}IgG} = 4.8 \pm 2.2$ nm.

It is common practice to electrostatically immobilize PA[166], [167]and the consistency in radius reduction in the present study underlines the robustness of this immobilization strategy. The size of PA (60 kDa) is very similar to BSA (65 kDa) and thus the observed radius reductions for both proteins are congruent. The obtained results for the

complexation of the immunoglobulins with the PA can be explained on the basis of the affinities of the different IgG`s Fc portions to PA: IgGs from human serum (H-IgG) possess a high binding affinity which facilitated the complexation with PA within the NAA pores, resulting in the observed radius reduction in IC1. In contrast, the affinity of IgG produced in Goat (AH-IgG) is rather low. Therefore, in IC2, the provided incubation time for AH-IgG was not sufficient to facilitate enough complexation with PA inside the confined space of the NAA pores. This results in the small change in slope and estimated radius. However, providing the reaction time and space for PA and AH-IgG in PBS solution in a test tube prior to the immobilization in NAA in IC3 compensated for the low affinity and enhanced the complexation as seen by the much larger radius reduction. The PA and IgG affinities and their respective radius reductions in experiments IC1 to IC3 are further co-validated by DLS measurements of protein and complex size in solution after 2h (figure 5.16).

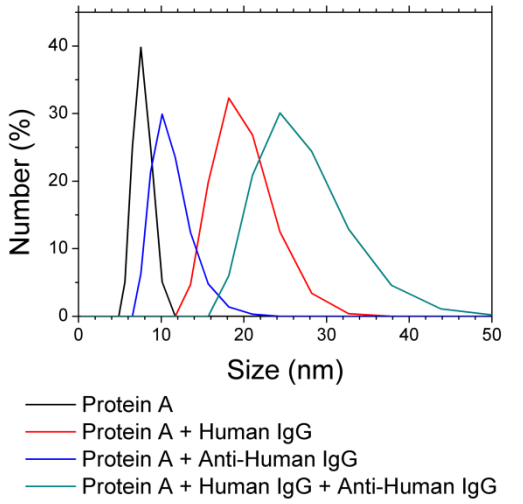

Figure 5.16: DLS measurements supporting low affinity of Protein A and Anti-Human IgG, and high affinity of Protein A and Human IgG, after 2 hours of incubation in solution.

The AG-IgG were produced in rabbit and are known to have a high affinity for PA which was demonstrated by significant slope increases and the respective radius reductions of IC4. The further immune complexation of the G-IgG resulted in significantly different slopes. Even though the sizes of the IgGs are on the smaller end of the expected results, the significant signal changes underline the detection of the immune complexation. With these results we demonstrate that FICLI is well capable as an immunosensing system, although it is very dependent on the biomolecular affinities what means the experimental procedures have to be accurately designed.

5.6 Summary

In this chapter, it was demonstrated that FICLI is a highly sensitive method to detect and quantify changes in the pore surface properties and dimensions of NAA after the attachment of different biological and chemical analytes. The accuracy of FICLI for the characterization of pore size changes of NAA produced in oxalic and sulfuric acids has been shown. The radius increase due to wet chemical pore widening was detected irrespective of the electrolyte used to prepare the NAA, and the results are in good agreement with traditional NAA characterization methods such as ESEM and the literature. The electrostatic immobilization of biomolecules to the pore walls is a common and fast NAA modification technique. In this study, it was shown that the pore radius reduction of the NAA due to the immobilization of BSA is accurately estimated by FICLI. The radius reduction estimates fall into the expected size dimensions of the protein, and the radius reductions are reproducible irrespective of the NAA material and initial pore radius. Only slight differences are observed for NAA obtained with different electrolytes, which is an indication that the surface contact angle for such structures depends slightly of the electrolyte. The pore radius reduction due to the functionalization of NAA pore walls with APTES–GTA was characterized. The observed radius reduction value suggests the deposition of an APTES multilayer due to reaction conditions. The subsequent covalent immobilization of streptavidin via imine bonds was further detected by a radius reduction. The dimensions of the protein were slightly overestimated and also suggest a multilayer deposition of the protein. The immobilization of IgGs via immune complexation with PA and secondary IgGs was detected by the

characterization of NAA pore radius reductions and changing capillary filling dynamics. It was shown that a chain of immobilization events starting with the electrostatic immobilization of PA, followed by specific immune complexations of IgG and secondary IgG can be demonstrated by the size reduction of NAA pores. These findings provide great potential for the future development of target-specific biosensing systems based on the radius reduction of NAA and the changes in nanopore filling dynamics. Further research on real-time monitoring of filling dynamics variations can open the way to new sensing devices with a view to miniaturization.

Chapter 6

Summary & Conclusion

As presented in chapter 2 there is a wealth of applications of nanoporous anodic alumina (NAA) due to its optical and structural characteristics and in this PhD work we decided to focus on advancing its application in the fields of optofluidic sensing and nanometrology. The theoretical background, experimental setup and data treatment of the technique used in this PhD work were presented in great detail in chapter 3 but will be briefly summarized here.

A liquid-solid interfacing system was used in the form of an NAA membrane with removed barrier layer and both pore ends exposed to the environment as the solid carrier matrix. The liquid interface is introduced in the form of a liquid drop released onto the top surface which is then readily passing through the nanopores via capillary forces. The fluid movement is monitored in real-time via a monochromatic laser beam directed at the NAA from the bottom side, which gets reflected off of the top and bottom interface of the NAA membrane.Since the NAA pores are smaller than the laser wavelength the NAA containing air, the liquid or a combination of both can be regarded as an effective medium. As the liquid travels through the NAA and the pore space is more and more filled with liquid it gradually changes the effective refractive index of the effective medium. This gradual effective refractive index change changes the optical path difference between a laser beam reflected off of the top surface of the NAA. The interference of the top and bottom reflected beams causes distinct light intensity patterns with extrema in the form of oscillations which can be represented in time-resolved interferograms of light intensity units over time. From the elapsed time between two adjacent light intensity extrema of such an interferogram and their respective order magnitude, given in integers, the pore radius

can be estimated. The term fluid imbibition coupled laser interferometry (FICLI) was coined.

It was further experimentally shown that even though the working principle of FICLI holds up for NAA with intact barrier layer, the build-up of gas pressure significantly alters the fluid movement and introduces a bias during the interferogram analysis for the radius estimation. In this sense it was also demonstrated that FICLI can be applied as a monitoring device for the pore opening process. Additionally, the volume of the liquid drop released onto the NAA surface, the total NAA thickness and the point of laser beam incident were shown not to alter the radius estimations.

Chapter 4 addressed the sensitivity, accuracy and reproducibility of FICLI of radius estimations for NAA produced in sulfuric acid (NAA_{sul}) and oxalic acid (NAA_{ox}) and consecutive pore widening steps. A Comparison of the results to scanning electron microscopy (SEM) image analysis showed that FICLI measurement replicates produce pore radius estimates with a lower variance and only minor differences in mean pore radius values. The latter differences were mainly attributed to the factor of subjectivity of choosing grey cut off values during ESEM image analysis with poor resolution and an uncertainty about the absolute value of the liquids contact angle within nanopores. However, the results of both methods are in good agreement with the literature and pore widening steps as short as 2 minutes with pore radius differences as small as 2 nm were possible to be resolved by FICLI, which underlines its sensitivity.

More complex pore structures in the form of bilayers and trilayers were fabricated and the pore radii of each new layer were estimated showing that FICLI is not only a topological technique but is able to characterise the internal structure of a nanopore. FICLI pore radius estimations were shown to be reproducible across a variety of different liquid-solid interfaces by means of using DI water, ethanol and 2-propanol passing through either NAA_{sul} or NAA_{ox}.

Chapter 5 introduced pore radius modifications by means of more complex surface chemistry changes in NAA_{sul} and NAA_{ox} and it was shown that FICLI is a highly sensitive method capable of detecting and resolving such changes in pore surface properties and dimensions. Pore radius reductions of NAA due to electrostatic immobilization of BSA were accurately estimated by FICLI yielding expected size dimensions of the protein. The pore radius reductions were reproducible across different NAA materials (sulfuric and oxalic acid) and initial pore radius with only minor differences indicating a dependency of the surface contact angle on the electrolyte the NAA is fabricated with.

Using layer-by-layer deposition of polyelectrolytes showed that FICLI is capable of resolving each deposition step of the polymer with results congruent to the literature based on elipsometry on flat surfaces. Increasing estimates of pore radius reductions due to the organosilane-crosslinker system APTES–GTA over increasing incubation times during the functionalization process, suggests the deposition of multilayers. Covalently immobilizing streptavidin via imine bonds was detected with slightly overestimated dimensions of the protein also suggesting a multilayer deposition of the protein. Successfully

estimating the pore radius reductions of a chain of immobilization events of biomolecules via electrostatic immobilization of Protein A, followed by specific immune complexations of IgG and secondary IgG showed that changing capillary filling dynamics has great potential as a biosensor based on radius reduction.

In summary, the results presented in this PhD dissertation demonstrated the applicability of time-resolved interferometric monitoring of fluid dynamics as a powerful tool for the characterisation of nanopores. The accurate estimation of pore radii across a variety of different liquid surface interfaces showed the capability of this system to resolve changes in the nanopore pore dimension of below 2nm. Monitoring binding events of polymers and biomolecules on the pore walls immobilised via different strategies showed the potential for target-specific biosensing based on radius reduction in NAA and may well have opened the door for the development of novel lab-on-chip and point-of-care sensing devices.

In conclusion FICLI is a beneficial addition to nanometrology and relevant for applications where the characterisation of pores with a resolution on the nanometer level is important.

Other nano-characterisation and sensing applications might benefit from FICLI's ease of use and sensitivity. For example the fabrication of carbon- or polymer-based nanotubes via NAA scaffolds might be a useful future application for FICLI to characterise the growth rate or total thickness of fabricated tubes before etching off the alumina matrix. Polyelectrolytes can be stimulated to swell or shrink by changing the

local environment. Estimating the degree of swelling of such a functionalisation might give relevant insight for the development and characterisation of drug loading and releasing of drug delivery systems. Determining the liquid contact angle within nanopores is currently still openly discussed and monitoring the pore filling dynamics in combination with high resolution electron microscopy producing more accurate pore radius estimates via image analysis, FICLI might contribute producing more accurate data on the dynamic contact angle within the nano-confinement.

References

[1] "British Patent 223994 (1923)."

[2] "Italian Patent 741753 (1936)."

[3] F. KELLER, M. S. HUNTER, and D. L. ROBINSON, "Structural Features of Oxide Coatings on Aluminum," *J. Electrochem. Soc.*, vol. 100, pp. 411–419, 1953.

[4] J. W. Diggle, T. C. Downie, and C. W. Goulding, "Anodic oxide films on aluminum," *Chem. Rev.*, vol. 69, no. 3, pp. 365–405, 1969.

[5] J. P. O'Sullivan and G. C. Wood, "The morphology and mechanism of formation of porous anodic films on aluminium," *Proc. R. Soc. London Ser. A – Math. Phys. Sci.*, vol. 317, no. 1531, pp. 511–543, 1970.

[6] Thompson and Wood, "Porous anodic film formation on aluminium," *Nature*, vol. 290. pp. 230–232, 1981.

[7] G. C. Wood, P. Skeldon, G. E. Thompson, and K. Shimizu, "A Model for the Incorporation of Electrolyte Species into," *J. Electrochem. Soc.*, vol. 143, no. 1, pp. 74–83, 1996.

[8] H. Masuda and K. Fukuda, "Ordered metal nanohole arrays made by a two-step replication of honeycomb structures of anodic alumina.," *Science*, vol. 268, pp. 1466–1468, 1995.

[9] K. Nielsch, J. Choi, K. Schwirn, R. B. Wehrspohn, and U. Gösele, "Self-ordering Regimes of Porous Alumina: The 10 Porosity Rule," *Nano Lett.*, vol. 2, pp. 677–680, 2002.

[10] W. Lee and J. Kim, "Highly ordered porous alumina with tailor-made pore structures fabricated by pulse anodization," *Nanotechnology*, vol. 485304, no. 21, 2010.

[11] M. M. Rahman, L. F. Marsal, J. Pallarès, and J. Ferré-Borrull, "Tuning the Photonic Stop Bands of Nanoporous Anodic Alumina-Based Distributed Bragg Reflectors by Pore Widening," *ACS Appl. Mater. Interfaces*, vol. 5, pp. 13375–13381, 2013.

[12] P. Yan, G. T. Fei, G. L. Shang, B. Wu, and L. De Zhang, "Fabrication of one-dimensional alumina photonic crystals with a narrow band gap and their application to high-sensitivity sensors," *J. Mater. Chem. C*, vol. 1, pp. 1659–1664, 2013.

[13] A. Mutalib, D. Losic, and N. H. Voelcker, "Nanoporous anodic aluminium oxide : Advances in surface engineering and emerging applications," *Prog. Mater. Sci.*, vol. 58, no. 5, pp. 636–704, 2013.

[14] T. Kumeria, A. Santos, and D. Losic, "Nanoporous anodic alumina platforms: engineered surface chemistry and structure for optical sensing applications.," *Sensors (Basel).*, vol. 14, no. 7, pp. 11878–918, Jan. 2014.

[15] I. Vlassiouk, A. Krasnoslobodtsev, S. Smirnov, and M. Germann, "' Direct ' Detection and Separation of DNA Using Nanoporous Alumina Filters," *Langmuir*, vol. 20, no. 23, pp. 9913–9915, 2004.

[16] E. J. Sin *et al.*, "SURFACE MODIFICATION OF ALUMINUM OXIDE FOR BIOSENSING APPLICATION," *Biomed. Eng. Appl. Basis Commun.*, vol. 24, no. 2, pp. 111–116, 2012.

[17] M. Porta-i-Batalla, C. Eckstein, E. Xifré-Pérez, P. Formentín, J. Ferré-Borrull, and L. F. Marsal, "Sustained, Controlled and Stimuli-Responsive Drug Release Systems Based on Nanoporous Anodic Alumina with Layer-by-Layer Polyelectrolyte," *Nanoscale Res. Lett.*, vol. 11, no. 1, p. 372, 2016.

[18] F. Li, "Nanostructure of anodic porous alumina films of interest in magnetic recording," *PhD Thesis, Univ. Alabama*, 1998.

[19] A. Santos, "Structural Engineering of Nanoporous Anodic Alumina and Applications," *PhD Thesis, Lambert Acad. Publ.*, 2011.

[20] H. Masuda, F. Hasegwa, and S. Ono, "Self − Ordering of Cell Arrangement of Anodic Porous Alumina Formed in Sulfuric Acid Solution," *J. Electrochem. Soc.*, vol. 144, no. 5, pp. L127–L130, 1997.

[21] A. O. H. Masuda, K. Yada, "Self-Ordering of Cell Configuration of Anodic Porous Alumina with Large-Size Pores in Phosphoric Acid Solution," *Jpn. J. Appl. Phys.*, vol. 1340, no. 37, pp. L1340–L1342, 1998.

[22] W. Lee, K. Nielsch, and U. Gösele, "Self-ordering behavior of nanoporous anodic aluminum oxide (AAO) in malonic acid anodization," *Nanotechnology*, vol. 475713, no. 18, 2007.

[23] S. Ono, M. Saito, M. Ishiguro, and H. Asoh, "Controlling Factor of Self-Ordering of Anodic Porous Alumina," *J. Electrochem. Soc.*, vol. 151, no. January 2004, pp. B473–B478, 2004.

[24] W. Lee, R. Ji, U. G. Osele, and K. Nielsch, "Fast fabrication of long-range ordered porous alumina membranes by hard anodization," *Nat. Mater.*, vol. 5, no. September, pp. 741–747, 2006.

[25] T. Aerts, T. Dimogerontakis, I. De Graeve, J. Fransaer, and H. Terryn, "Influence of the anodizing temperature on the porosity and the mechanical properties of the porous anodic oxide film," *Surf. Coatings Technol.*, vol. 201, pp. 7310–7317, 2007.

[26] W. Chen, J. Wu, and X. Xia, "Porous Anodic Alumina with Continuously Manipulated Pore / Cell Size," *ACS Nano*, vol. 2, no. 5, pp. 959–965, 2008.

[27] C. V. Manzano, J. Martín, and M. S. Martín-González, "Ultra-narrow 12 nm pore diameter self-ordered anodic alumina templates," *Microporous Mesoporous Mater.*, vol. 184, pp. 177–183, 2014.

[28] H. Takahashi and M. Nagayama, "The determination of the porosity of anodic oxidfe films on aluminium by the pore-filling method," *Corros. Sci.*, vol. 18, no. November 1977, pp. 911–925, 1978.

[29] O. Jessensky, F. Müller, and U. Gösele, "Self-organized formation of hexagonal pore arrays in anodic alumina," *Appl. Phys. Lett.*, vol. 72, p. 1173, 1998.

[30] R. Urteaga *et al.*, "Optofluidic Characterization of Nanoporous Membranes," *Langmuir*, vol. 29, no. 8, pp. 2784–2789, Feb. 2013.

[31] L. N. Acquaroli, R. Urteaga, C. L. A. Berli, and R. R. Koropecki, "Capillary filling in nanostructured porous silicon.," *Langmuir*, vol. 27, no. 5, pp. 2067–72, Mar. 2011.

[32] E. Elizalde, R. Urteaga, R. R. Koropecki, and C. L. A. Berli, "Inverse Problem of Capillary Filling," *Phys. Rev. Lett.*, vol. 112, no. 13, p. 134502, 2014.

[33] M. Lillo and D. Losic, "Pore opening detection for controlled dissolution of barrier oxide layer and fabrication of nanoporous alumina with through-hole morphology," *J. Memb. Sci.*, vol. 327, no. 1–2, pp. 11–17, Feb. 2009.

[34] M. Lillo and D. Losic, "Ion-beam pore opening of porous anodic alumina: The formation of single nanopore and nanopore arrays," *Mater. Lett.*, vol. 63, pp. 457–460, 2009.

[35] a. Santos, L. Vojkuvka, J. Pallarés, J. Ferré-Borrull, and L. F. Marsal, "In situ electrochemical dissolution of the oxide barrier layer of porous anodic alumina fabricated by hard anodization," *J. Electroanal. Chem.*, vol. 632, no. 1–2, pp. 139–142, Jul. 2009.

[36] H. Han *et al.*, "In situ determination of the pore opening point during wet-chemical etching of the barrier layer of porous anodic aluminum oxide: Nonuniform Impurity Distribution in Anodic Oxide," *ACS Appl. Mater. Interfaces*, vol. 5, no. 8, pp. 3441–3448, 2013.

[37] M. Jung *et al.*, "Characteristics and fabrication of nanohole array on InP semiconductor substrate using nanoporous alumina," *Microelectronics J.*, vol. 39, pp. 526–528, 2008.

[38] A. P. Li, F. Müller, A. Birner, K. Nielsch, and U. Gösele, "Hexagonal pore arrays with a 50 – 420 nm interpore distance formed by self-organization in anodic alumina," *J. Appl. Phys.*, vol. 6023, no. 84, 1998.

[39] Y. Fu, N. Kok, A. Bryan, and L. T. Fatt, "Fabrication and Characterization of Nanopore Array," *J. Nanosci. Nanotechnol.*, vol. 6, no. 6, pp. 1954–1960, 2006.

[40] H. Chang *et al.*, "Fabrication and characterization of solid-state nanopores using a field emission scanning electron microscope," *Appl. Phys. Lett.*, vol. 103109, no. 2006, pp. 2004–2007, 2014.

[41] M. Wu *et al.*, "Formation of nanopores in a Si N/Si O 2 membrane with an electron beam," *Appl. Phys. Lett.*, vol. 113106, no. 2005, pp. 1–4, 2009.

[42] J. Li, D. Stein, C. Mcmullan, and D. Branton, "Ion-beam sculpting at nanometre length scales," *Nature*, vol. 412, no. July, pp. 166–169, 2001.

[43] P. Y. Apel, "Etching of nanopores in polycarbonate irradiated with swift heavy ions at 15 K," *Nucl. Instruments Methods Phys. Res. B*, vol. 245, pp. 284–287, 2006.

[44] F. Buyukserin and C. R. Martin, "The use of Reactive Ion Etching for obtaining ' free ' silica nano test tubes," *Appl. Surf. Sci.*, vol. 256, no. 24, pp. 7700–7705, 2010.

[45] S. SAITO, K. SUGITA, and J. TONOTANI, "Effect of CHF3 Addition on Reactive Ion Etching of Aluminum Using Inductively

Coupled Plasma," *Jpn. J. Appl. Phys.*, vol. 44, no. 5A, pp. 2971–2975, 2005.

[46] J. Kim, Y. Kim, and W. Lee, "Reactive ion etching deposited aluminum mechanism of plasma enhanced oxide film in CF4 / 02 plasma chemically vapor," *J. Appl. Phys.*, vol. 78, no. 3, pp. 2045–2049, 1995.

[47] L. Vojkuvka, L. F. Marsal, and J. Pallares, "Study of Porous Alumina Porosity after Pore Widening Process," *2007 Spanish Conf. Electron Devices, Proc.*, pp. 41–43, 2007.

[48] W. L. Xu, H. Chen, M. J. Zheng, G. Q. Ding, and W. Z. Shen, "Optical transmission spectra of ordered porous alumina membranes with different thicknesses and porosities," *Opt. Mater. (Amst).*, vol. 28, pp. 1160–1165, 2006.

[49] F. Le Coz, L. Arurault, S. Fontorbes, V. Vilar, L. Datas, and P. Winterton, "Chemical composition and structural changes of porous templates obtained by anodising aluminium in phosphoric acid electrolyte," *Surf. Interface Ananlysis*, vol. 42, no. December 2009, pp. 227–233, 2010.

[50] K. E. La Flamme *et al.*, "Biocompatibility of nanoporous alumina membranes for immunoisolation," *Biomaterials*, vol. 28, pp. 2638–2645, 2007.

[51] J. Salonen and V. Lehto, "Fabrication and chemical surface modification of mesoporous silicon for biomedical applications," *Chem. Eng. J.*, vol. 137, pp. 162–172, 2008.

[52] M. Baranowska *et al.*, "Protein attachment to nanoporous anodic alumina for biotechnological applications: influence of pore size, protein size and functionalization path.," *Colloids Surf. B. Biointerfaces*, vol. 122, pp. 375–83, Oct. 2014.

[53] K. C. Popat, G. Mor, C. A. Grimes, and T. A. Desai, "Surface Modification of Nanoporous Alumina Surfaces with Poly (ethylene glycol)," *Langmuir*, vol. 19, no. 10, pp. 8035–8041, 2004.

[54] G. Demirel and F. Buyukserin, "Surface-Induced Self-Assembly of Dipeptides onto Nanotextured Surfaces," *Langmuir*, vol. 27, no. 20, pp. 12533–12538, 2011.

[55] V. Biju, "Chemical modifications and bioconjugate reactions of nanomaterials for sensing, imaging, drug delivery and therapy.," *Chem. Soc. Rev.*, vol. 43, no. 3, pp. 744–764, 2014.

[56] J. J. Gooding, S. Ciampi, and J. J. Gooding, "The molecular level modification of surfaces : from self-assembled monolayers to complex molecular assemblies," *Chem. Soc. Rev.*, vol. 40, no. 5, pp. 2704–2718, 2011.

[57] H. S. Mansur, R. L. Oréfice, W. L. Vasconcelos, Z. P. Lobato, and L. J. C. Machado, "Biomaterial with chemically engineered surface for protein immobilization," *J. Mater. Sci. Mater. Med.*, vol. 6, pp. 333–340, 2005.

[58] V. Smuleac, D. A. Butterfield, S. K. Sikdar, R. S. Varma, and D. Bhattacharyya, "Polythiol-functionalized alumina membranes for mercury capture," *J. Memb. Sci.*, vol. 251, pp. 169–178, 2005.

[59] G. Rajeev, E. Xifre-perez, B. Prieto, A. J. Cowin, L. F. Marsal, and N. H. Voelcker, "A label-free optical biosensor based on nanoporous anodic alumina for tumour necrosis factor-alpha detection in chronic wounds," *Sensors Actuators B. Chem.*, vol. 257, pp. 116–123, 2018.

[60] C. M. Halliwell and A. E. G. Cass, "A Factorial Analysis of Silanization Conditions for the Immobilization of Oligonucleotides on Glass Surfaces," *Anal. Chem.*, vol. 73, no. 11, pp. 2476–2483, 2001.

[61] S. R. Ghaemi, F. Harding, B. Delalat, R. Vasani, and N. H. Voelcker, "Surface Engineering for Long-Term Culturing of Mesenchymal Stem Cell Microarrays," *Biomacromolecules*, vol. 14, no. 8, pp. 2675–2683, 2013.

[62] S. G. Thakurta and A. Subramanian, "Fabrication of dense , uniform aminosilane monolayers : A platform for protein or ligand immobilization," *Colloids Surfaces A Physicochem. Eng. Asp.*, vol. 414, no. 0, pp. 384–392, 2012.

[63] L. Velleman, G. Triani, P. J. Evans, J. G. Shapter, and D. Losic, "Structural and chemical modification of porous alumina membranes," *Microporous Mesoporous Mater.*, vol. 126, no. 1–2, pp. 87–94, 2009.

[64] T. Kumeria, A. Santos, and D. Losic, "Ultrasensitive Nanoporous Interferometric Sensors for Label-free Detection of Gold (III) Ions.," *ACS Appl. Mater. Interfaces*, vol. 5, no. Iii, p. 11783−11790, 2013.

[65] E. Metwalli, D. Haines, O. Becker, S. Conzone, and C. G. Pantano, "Surface characterizations of mono- , di- , and tri-aminosilane treated glass substrates," *J. Colloid Interface Sci.*, vol. 298, pp. 825–831, 2006.

[66] J. Largueze, K. El, and S. Morandat, "Colloids and Surfaces B : Biointerfaces Preparation of an electrochemical biosensor based on lipid membranes in nanoporous alumina," *Colloids Surfaces B Biointerfaces*, vol. 79, no. 1, pp. 33–40, 2010.

[67] P. Takmakov, I. Vlassiouk, and S. Smirnov, "Hydrothermally shrunk alumina nanopores and their application to DNA sensing," *Analyst*, vol. 131, no. 11, pp. 1248–1253, 2006.

[68] P. Takmakov, I. Vlassiouk, and S. Smirnov, "Application of anodized aluminum in fluorescence detection of biological species," *Anal Bioanal Chem*, vol. 385, no. 5, pp. 954–958, 2006.

[69] V. Szczepanski, I. Vlassiouk, and S. Smirnov, "Stability of silane modifiers on alumina nanoporous membranes," *J. Memb. Sci.*, vol. 281, no. April, pp. 587–591, 2006.

[70] M. Yamaura *et al.*, "Preparation and characterization of (3-aminopropyl) triethoxysilane-coated magnetite nanoparticles," *J. Magn. Magn. Mater.*, vol. 279, pp. 210–217, 2004.

[71] J. A. Howarter, J. P. Youngblood, R. V May, I. Final, and F. September, "Optimization of Silica Silanization by 3-Aminopropyltriethoxysilane," *Langmuir*, vol. 47907, no. 30, pp. 11142–11147, 2006.

[72] E. E. Leary Swan, K. C. Popat, and T. a. Desai, "Peptide-immobilized nanoporous alumina membranes for enhanced osteoblast adhesion," *Biomaterials*, vol. 26, pp. 1969–1976, 2005.

[73] B. Bhushan, K. J. Kwak, and S. Gupta, "Nanoscale adhesion , friction and wear studies of biomolecules on silane polymer-coated silica and alumina-based surfaces," *J. R. Soc. Interface*, vol. 6, no. November 2008, pp. 719–733, 2009.

[74] R. E. Ducker, M. T. Montague, and G. J. Leggett, "A comparative investigation of methods for protein immobilization on self-assembled monolayers using glutaraldehyde , carbodiimide , and anhydride reagents," *Biointerphase*, vol. 3, no. 3, pp. 59–65, 2008.

[75] D. Kim and A. E. Herr, "Protein immobilization techniques for microfluidic assays," *Biomicrofluidics*, vol. 7, no. 4, pp. 1–47, 2013.

[76] K. Fukuzaki, S.; Urano, H.; Nagata, "Adsorption of Bovine Serum Albumin onto Metal Oxide Surfaces," *J. Ferment. Bioeng.*, vol. 81, no. 2, pp. 163–167, 1996.

[77] A. Dhathathreyan, "Real-time monitoring of invertase activity immobilized in nanoporous aluminum oxide.," *J. Phys. Chem. B*, vol. 115, no. 20, pp. 6678–82, May 2011.

[78] C. Chang and S. Suen, "Modification of porous alumina membranes with n -alkanoic acids and their application in protein adsorption," *J. Memb. Sci.*, vol. 275, no. (1-2), pp. 70–81, 2006.

[79] M. L. Bruening, D. M. Dotzauer, P. Jain, L. Ouyang, and G. L. Baker, "Creation of Functional Membranes Using Polyelectrolyte

Multilayers and Polymer Brushes," *Langmuir*, vol. 24, no. 18, pp. 7663–7673, 2008.

[80] M. L. Bruening and M. Adusumilli, "Polyelectrolyte Multilayer Films and Membrane Functionalization Film Formation Functionalized Membranes," *Aldrich. Mater. Sci.*, pp. 76–81.

[81] L. Ouyang, R. Malaisamy, and M. L. Bruening, "Multilayer polyelectrolyte films as nanofiltration membranes for separating monovalent and divalent cations," *J. Memb. Sci.*, vol. 310, no. 1–2, pp. 76–84, 2008.

[82] X. Liu and M. L. Bruening, "Size-Selective Transport of Uncharged Solutes through Multilayer Polyelectrolyte Membranes," *Chem Mater*, no. 17, pp. 351–357, 2004.

[83] U. S. Hong and M. L. Bruening, "Separation of amino acid mixtures using multilayer polyelectrolyte nanofiltration membranes," *J. Memb. Sci.*, vol. 280, pp. 1–5, 2006.

[84] C. S. Peyratout and L. Dähne, "Tailor-Made Polyelectrolyte Microcapsules : From Multilayers to Smart Containers Angewandte," *Angew. Chemie*, vol. 43, no. 29, pp. 3762–3783, 2004.

[85] J. Dai, G. L. Baker, and M. L. Bruening, "Use of Porous Membranes Modified with Polyelectrolyte Multilayers as Substrates for Protein Arrays with Low Nonspecific Adsorption," *Anal Chem*, vol. 78, no. 1, pp. 135–140, 2006.

[86] D. M. Dotzauer, J. Dai, L. Sun, and M. L. Bruening, "Catalytic

Membranes Prepared Using Layer-by-Layer Adsorption of Polyelectrolyte / Metal Nanoparticle Films in Porous Supports," *Nano Lett.*, vol. 6, no. 10, 2006.

[87] Y. Yang, Q. He, L. Duan, Y. Cui, and J. Li, "Assembled alginate / chitosan nanotubes for biological application," *Biomaterials*, vol. 28, pp. 3083–3090, 2007.

[88] P. M. Biesheuvel, T. Mauser, and G. B. Sukhorukov, "Micromechanical Theory for pH-Dependent Polyelectrolyte Multilayer Capsule Swelling," *Macromolecules*, vol. 39, pp. 8480–8486, 2006.

[89] J. Krenkova and F. Foret, "Immobilized microfluidic enzymatic reactors," *Electrophoresis*, vol. 25, pp. 3550–3563, 2004.

[90] F. Rusmini, Z. Zhong, and J. Feijen, "Protein Immobilization Strategies for Protein Biochips," *Biomacromolecules*, vol. 8, pp. 1775–1789, 2007.

[91] K. Nakanishi, T. Sakiyama, Y. Kumada, K. Imamura, and H. Imanaka, "Recent Advances in Controlled Immobilization of Proteins onto the Surface of the Solid Substrate and Its Possible Application to Proteomics," *Curr. Proteomics*, vol. 5, pp. 161–175, 2008.

[92] J. Yakovleva, R. Davidsson, M. Bengtsson, T. Laurell, and J. Emneus, "Microfluidic enzyme immunosensors with immobilised protein A and G using chemiluminescence detection," *Biosens. Bioelectron.*, vol. 19, pp. 21–34, 2003.

[93] S. Laib and B. D. Maccraith, "Immobilization of Biomolecules on Cycloolefin Polymer Supports," *Anal Chem*, vol. 79, no. 16, pp. 6264–6270, 2007.

[94] L. N. Amankwa and W. G. Kuhr, "Trypsin-Modified Fused-Silica Capillary Microreactor for Peptide Mapping by Capillary Zone Electrophoresis," *Anal Chem*, vol. 64, no. 10, pp. 1610–1613, 1992.

[95] C. L. Smith and S. M. Giang, "Immobilization of Nucleic Acids Using Biotin-Strept (avidin) Systems," *Top Curr Chem*, vol. 261, no. November 2005, pp. 63–90, 2006.

[96] A. Kuzuya, K. Numajiri, M. Kimura, and M. Komiyama, "Single-molecule accommodation of streptavidin in nanometer-scale wells formed in DNA nanostructures.," *Nucleic Acids Symp. Ser. (Oxf).*, no. 52, pp. 681–682, 2008.

[97] S. Pan and L. J. Rothberg, "Interferometric sensing of biomolecular binding using nanoporous aluminum oxide templates," *Nano Lett.*, vol. 3, pp. 811–814, 2003.

[98] I. Sjöholm, "Protein A from Staphylococcus aureus. Spectropolarimetric and Spectrophotometric Studies.," *Eur. J. Biochem*, vol. 51, pp. 55–61, 1975.

[99] Uptima@interchim.com, "Protein A , IgG-Fc binding protein, FT-40290A," *Uptima Prod. Descr.*, vol. 1, pp. 1–3.

[100] S. D. Alvarez, C. P. Li, C. E. Chiang, I. K. Schuller, and M. J. Sailor, "A label-free porous alumina interferometric immunosensor," *ACS Nano*, vol. 3, no. 10, pp. 3301–3307, 2009.

[101] G. Macias, J. Ferré-Borrull, J. Pallarès, and L. F. Marsal, "Effect of pore diameter in nanoporous anodic alumina optical biosensors.," *Analyst*, Dec. 2014.

[102] C. Eckstein *et al.*, "Nanoporous Anodic Alumina Surface Modification by Electrostatic, Covalent, and Immune Complexation Binding Investigated by Capillary Filling," *ACS Appl. Mater. Interfaces*, vol. 10, no. 12, pp. 10571–10579, 2018.

[103] D. Losic and A. Santos, *Nanoporous Alumina.* .

[104] K. A. Willets and R. P. Van Duyne, "Localized Surface Plasmon Resonance Spectroscopy and Sensing," *Annu. Rev. Phys. Chem.*, vol. 58, pp. 267–97, 2007.

[105] M. Saito, M. Shibasaki, S. Nakamura, and M. Miyagi, "Optical waveguides fabricated in anodic alumina films," *Opt. Lett.*, vol. 19, no. 10, pp. 710–712, 1994.

[106] K. H. A. Lau, L. Tan, K. Tamada, M. S. Sander, and W. Knoll, "Highly Sensitive Detection of Processes Occurring Inside Nanoporous Anodic Alumina Templates : A Waveguide Optical Study," *J. Phys. Chem. B*, vol. 108, pp. 10812–10818, 2004.

[107] K. S. Dancil, D. P. Greiner, and M. J. Sailor, "A Porous Silicon Optical Biosensor : Detection of Reversible Binding of IgG to a Protein A-Modified Surface," *J. Am. Chem. Soc.*, vol. 121, no. 14, pp. 7925–7930, 1999.

[108] T. Kumeria and D. Losic, "Controlling interferometric properties of nanoporous anodic aluminium oxide," *Nanoscale Res. Lett.*, vol.

7, p. 88, 2012.

[109] D. Guo, L. Fan, F. Wang, S. Huang, and X. Zou, "Porous Anodic Aluminum Oxide Bragg Stacks as Chemical Sensors," *J. Phys. Chem. C*, vol. 112, pp. 17952–17956, 2008.

[110] L. Pang, H. M. Chen, L. M. Freeman, and Y. Fainman, "Optofluidic devices and applications in photonics, sensing and imaging," *Lab Chip*, vol. 12, p. 3543, 2012.

[111] D. Psaltis, S. R. Quake, and C. Yang, "Developing optofluidic technology through the fusion of microfluidics and optics," *Nature*, vol. 442, no. 7101, pp. 381–386, 2006.

[112] K. Huang, L. Pu, Y. Shi, P. Han, R. Zhang, and Y. D. Zheng, "Photoluminescence oscillations in porous alumina films," *Appl. Phys. Lett.*, vol. 89, no. 20, pp. 1–4, 2006.

[113] A. Santos *et al.*, "Structural tuning of photoluminescence in nanoporous anodic alumina by hard anodization in oxalic and malonic acids.," *Nanoscale Res. Lett.*, vol. 7, no. 1, p. 228, Jan. 2012.

[114] Y. Yamamoto, N. Baba, and S. Tajima, "Coloured materials and photoluminescence centers in anodic film on aluminium," *Nature*, vol. 289, pp. 572–574, 1981.

[115] Y. Liu, Y. Tu, S. Huang, J. Sang, and X. Zou, "Effect of etch-treatment upon the intensity and peak position of photoluminescence spectra for anodic alumina films with ordered nanopore array," *J. Mater. Sci.*, vol. 44, pp. 3370–3375, 2009.

[116] N. I. Mukhurov *et al.*, "INFLUENCE OF ELECTROLYTE COMPOSITION ON PHOTOLUMINESCENT PROPERTIES OF ANODIC ALUMINUM OXIDE," *J. Appl. Spectrosc.*, vol. 75, no. 2, pp. 208–212, 2008.

[117] T. Gao, G. Meng, and L. Zhang, "Blue luminescence in porous anodic alumina films : the role of the oxalic impurities," *J. Phys. Condens. Matter*, vol. 15, pp. 2071–2079, 2003.

[118] Y. Du *et al.*, "Preparation and photoluminescence of alumina membranes with ordered pore arrays," *Appl. Phys. Lett.*, vol. 74, p. 2951, 1999.

[119] Y. Li, G. W. Meng, L. D. Zhang, and F. Phillipp, "Photoluminescence and optical absorption caused by the F + centres in anodic alumina membranes," *J. Phys. Condens. Matter*, vol. 13, pp. 2691–2699, 2001.

[120] J. Choi, Y. Luo, R. B. Wehrspohn, R. Hillebrand, and J. Schilling, "Perfect two-dimensional porous alumina photonic crystals with duplex oxide layers," *J. Appl. Phys.*, vol. 94, p. 4757, 2003.

[121] W. L. Xu, M. J. Zheng, S. Wu, and W. Z. Shen, "Effects of high-temperature annealing on structural and optical properties of highly ordered porous alumina membranes," *Appl. Phys. Lett.*, vol. 85, p. 4364, 2004.

[122] G. Shi, C. M. Mo, W. L. Cai, and L. D. Zhang, "Photoluminescence of ZnO nanoparticles in alumina membrane with ordered pore arrays," *Solid State Commun.*, vol. 115, pp. 253–256, 2000.

[123] A. Santos *et al.*, "Nanoporous anodic alumina barcodes: Toward smart optical biosensors," *Adv. Mater.*, vol. 24, no. 8, pp. 1050–1054, 2012.

[124] A. Santos, T. Kumeria, and D. Losic, "Optically Optimized Photoluminescent and Interferometric Biosensors Based on Nanoporous Anodic Alumina: A Comparison," *Anal Chem*, vol. 85, pp. 7904–7911, 2013.

[125] A. Yamaguchi, K. Hotta, and N. Teramae, "Optical Waveguide Sensor Based on a Porous Anodic Alumina / Aluminum Multilayer Film," *Anal Chem*, vol. 81, no. 1, pp. 10812–10818, 2009.

[126] J. Pepper *et al.*, "Detection of proteins and intact microorganisms using microfabricated flexural plate silicon resonator arrays," *Sensors Actuators B*, vol. 96, pp. 565–575, 2003.

[127] A. Santos, G. MacÍas, J. Ferré-Borrull, J. Pallarès, and L. F. Marsal, "Photoluminescent enzymatic sensor based on nanoporous anodic alumina," *ACS Appl. Mater. Interfaces*, vol. 4, no. 7, pp. 3584–3588, 2012.

[128] T. Kumeria and D. Losic, "Reflective interferometric gas sensing using nanoporous anodic aluminium oxide (AAO)," *Phys. Status Solidi RRL*, vol. 5, no. 10–11, pp. 406–408, 2011.

[129] T. Kumeria, M. D. Kurkuri, K. R. Diener, L. Parkinson, and D. Losic, "Label-free reflectometric interference microchip biosensor based on nanoporous alumina for detection of circulating tumour cells," *Biosens. Bioelectron.*, vol. 35, no. 1, pp. 167–173, 2012.

[130] L. K. Acosta, F. Berto-rosello, E. Xifré-, A. Santos, J. Ferré-borrull, and L. F. Marsal, "Stacked Nanoporous Anodic Alumina Gradient-Index Filters with Tunable Multi-Spectral Photonic Stopbands as Sensing Platforms," *ACS Appl. Mater. Interfaces*, 2018.

[131] G. Gauglitz and J. Ingenhoff, "Design of new integrated optical substrates for immuno-analytical applications," *Anal. Chem.*, vol. 349, pp. 355–359, 1994.

[132] X. Fan and I. M. White, "Optofluidic microsystems for chemical and biological analysis," *Nat. Photonics*, vol. 5, no. 10, pp. 591–597, 2011.

[133] D. B. Wolfe *et al.*, "Dynamic control of liquid-core/liquid-cladding optical waveguides.," *Proc. Natl. Acad. Sci. U. S. A.*, vol. 101, no. 34, pp. 12434–12438, 2004.

[134] P. Domachuk, M. Cronin-Golomb, B. J. Eggleton, S. Mutzenich, G. Rosengarten, and A. Mitchell, "Application of optical trapping to beam manipulation in optofluidics," *Opt. Express*, vol. 13, no. 19, pp. 7265–7275, 2005.

[135] A. Mitra, B. Deutsch, F. Ignatovich, C. Dykes, and L. Novotny, "NIH Public AccessNano-optofluidic detection of single viruses and nanoparticles," *ACS Nano*, vol. 23, no. 1, pp. 1–7, 2010.

[136] W. W. Ye, J. Y. Shi, C. Y. Chan, L. D. Xiao, and M. Yang, "Nanoporous Alumina Membrane and Nanoparticle Based Microfluidic Sensing Platform for Direct DNA Detection," no. June, pp. 1255–1258, 2013.

[137] K. M. van Delft *et al.*, "Micromachined Fabry − Pérot Interferometer with Embedded Nanochannels for Nanoscale Fluid Dynamics," *Nano Lett.*, vol. 7, no. 2, pp. 345–350, 2007.

[138] A. Han, G. Mondin, N. G. Hegelbach, N. F. De Rooij, and U. Staufer, "Filling kinetics of liquids in nanochannels as narrow as 27 nm by capillary force," *J. Colloid Interface Sci.*, vol. 293, no. 2006, pp. 151–157, 2006.

[139] D. I. Dimitrov, A. Milchev, and K. Binder, "Capillary Rise in Nanopores : Molecular Dynamics Evidence for the Lucas-Washburn Equation," *Phys. Rev. Lett. week*, vol. 99, p. 054501, 2007.

[140] C. Wu, H. S. Leese, D. Mattia, R. R. Dagastine, D. Y. C. Chan, and R. F. Tabor, "A study of fluid and transport properties of porous anodic aluminium membranes by dynamic atomic force microscopy," *Langmuir*, vol. 29, no. 8969, 2013.

[141] P. Tabeling, *Introduction to Microfluidics*. New York: Oxford University Press, 2005.

[142] D. Erickson, D. Li, and C. B. Park, "Numerical Simulations of Capillary-Driven Flows in Nonuniform Cross-Sectional Capillaries," *J. Colloid Interface Sci.*, vol. 250, pp. 422–430, 2002.

[143] T. L. Staples and D. G. Shaffer, "Wicking flow in irregular capillaries," *Colloids Surfaces A Physicochem. Eng. Asp.*, vol. 204, pp. 239–250, 2002.

[144] M. REYSSAT, L. COURBIN, E. REYSSAT, and H. A. STONE,

"Imbibition in geometries with axial variations," *J. Fluid Mech.*, vol. 615, pp. 335–344, 2008.

[145] W. W. Liou, Y. Peng, and P. E. Parker, "Analytical modeling of capillary flow in tubes of nonuniform cross section," *J. Colloid Interface Sci.*, vol. 333, no. 1, pp. 389–399, 2009.

[146] M. Elzbieciak, M. Kolasinska, and P. Warszynski, "Characteristics of polyelectrolyte multilayers: The effect of polyion charge on thickness and wetting properties," *Colloids Surfaces A Physicochem. Eng. Asp.*, vol. 321, no. 1–3, pp. 258–261, 2008.

[147] E. W. Washburn, "The dynamics of capillary flow," *Phys. Rev.*, vol. 17, no. 3, pp. 273–283, 1921.

[148] R. Redón, A. Vázquez-Olmos, M. E. Mata-Zamora, A. Ordóñez-Medrano, F. Rivera-Torres, and J. M. Saniger, "Contact angle studies on anodic porous alumina," *J. Colloid Interface Sci.*, vol. 287, no. 2, pp. 664–670, 2005.

[149] C. Y. Han, G. A. Willing, Z. Xiao, and H. H. Wang, "Control of the anodic aluminum oxide barrier layer opening process by wet chemical etching," *Langmuir*, vol. 23, no. 19, pp. 1564–1568, 2007.

[150] G. Vazquez, E. Alvarez, and J. M. Navaza, "Tension of Alcohol + Water from 20 to 50 °C," *J. Chem. Eng. Data*, vol. 40, pp. 611–614, 1995.

[151] A. Hibara *et al.*, "Nanochannels on a fused-silica microchip and liquid properties investigation by time-resolved fluorescence measurements," *Anal. Chem.*, vol. 74, no. 24, pp. 6170–6176, 2002.

[152] N. R. Tas, J. Haneveld, H. V. Jansen, M. Elwenspoek, and A. van den Berg, "Capillary filling speed of water in nanochannels," *Appl. Phys. Lett.*, vol. 85, no. 15, p. 3274, 2004.

[153] V. Raspal, K. O. Awitor, C. Massard, E. Feschet-Chassot, R. S. P. Bokalawela, and M. B. Johnson, "Nanoporous surface wetting behavior: The line tension influence," *Langmuir*, vol. 28, no. 30, pp. 11064–11071, 2012.

[154] A. Santos, T. Kumeria, Y. Wang, and D. Losic, "Insitu monitored engineering of inverted nanoporous anodic alumina funnels: on the precise generation of 3D optical nanostructures.," *Nanoscale*, vol. 6, no. 1, pp. 9991–9999, 2014.

[155] M. Rahman, E. Garcia-Caurel, A. Santos, L. F. Marsal, J. Pallarès, and J. Ferré-Borrull, "Effect of the anodization voltage on the pore-widening rate of nanoporous anodic alumina," *Nanoscale Res. Lett.*, vol. 7, no. 1, p. 474, 2012.

[156] C. Eckstein, E. Xifré-Pérez, M. Porta-I-Batalla, J. Ferré-Borrull, and L. F. Marsal, "Optical Monitoring of the Capillary Filling Dynamics Variation in Nanoporous Anodic Alumina toward Sensing Applications," *Langmuir*, vol. 32, no. 41, pp. 10467–10472, 2016.

[157] J. Anderegg and W. Beeman, "An Investigation of the Size, Shape and Hydration of Serum Albumin by Small-angle X-Ray Scattering," *J. Am. Chem. Soc.*, vol. 77, no. 11, pp. 2927–2937, 1955.

[158] Q. Shi, Y. Zhou, and Y. Sun, "Influence of pH and Ionic Strength

on the Steric Mass Action Model Parameters around the Isoelectric Point of Protein," *Biotechnol. Prog.*, vol. 21, no. 2, pp. 516–523, 2005.

[159] K. W. Pearson, R. E. Smith, A. R. Mitchell, and E. R. Bissel, "AutomatedEnzymeAssaysby Use of a CentrifugalAnalyzerwith FluorescenceDetection," vol. 27, no. 2, pp. 256–262, 1981.

[160] R. E. Smith, "Identification Isoelectric Impregnated of Protease Focusing Using into Cellulose Isozymes after Analytical Fluorogenic Substrates Membranes ' the," *J. Histochem. Cytochem.*, vol. 32, no. 12, pp. 1265–1274, 1984.

[161] J. Grdadolnik and Y. Mar�chal, "Bovine serum albumin observed by infrared spectrometry. I. Methodology, structural investigation, and water uptake," *Biopolymers*, vol. 62, no. 1, pp. 40–53, 2001.

[162] J. W. Anderegg, W. W. Beeman, S. Shulman, and P. Kaesberg, "An Investigation of the Size, Shape and Hydration of Serum Albumin by Small-angle X-Ray Scattering," *J. Am. Chem. Soc.*, vol. 77, no. 11, pp. 2927–2937, Jun. 1955.

[163] W. J. Stępniowski *et al.*, "Fabrication of anodic aluminum oxide with incorporated chromate ions," *Appl. Surf. Sci.*, vol. 259, pp. 324–330, Oct. 2012.

[164] R. G. Acres *et al.*, "Molecular structure of 3-aminopropyltriethoxysilane layers formed on silanol-terminated silicon surfaces," *J. Phys. Chem. C*, vol. 116, no. 10, pp. 6289–6297, 2012.

[165] E. T. Vandenberg *et al.*, "Structure of 3-aminopropyl triethoxy silane on silicon oxide," *J. Colloid Interface Sci.*, vol. 147, no. 1, pp. 103–118, 1991.

[166] D. Hyndman, T. G. Flynn, G. Lever, and R. Burrell, "Protein immobilization to alumina supports: I. Characterization of alumina-organophosphate ligand interactions and use in the attachment of papain," *Biotechnol. Bioeng.*, vol. 40, no. 11, pp. 1319–1327, Dec. 1992.

[167] Y. H. Tan, M. Liu, B. Nolting, J. G. Go, J. Gervay-Hague, and G. Y. Liu, "A nanoengineering approach for investigation and regulation of protein immobilization," *ACS Nano*, vol. 2, no. 11, pp. 2374–2384, 2008.

UNIVERSITAT ROVIRA I VIRGILI
CAPILLARY FILLING DYNAMICS AS A METROLOGICAL CHARACTERISATION TECHNIQUE FOR THE DETECTION OF RADIUS CHANGES AND SURFACE MODIFICATIONS IN NANOPOROUS ANODIC ALUMINA
Chris Eckstein